MANUFACTURING ANALYSIS AND DESIGN OPTIMIZATION OF IRRIGATION PUMPS FOR BANGLADESH

A Thesis

Presented to

The Academic Faculty

by

Su Yu

In Partial Fulfillment

of the Requirements for the Degree

Master of Science in Mechanical Engineering in the

School of Mechanical Engineering

Georgia Institute of Technology

May 2017

MANUFACTURING ANALYSIS AND DESIGN OPTIMIZATION OF IRRIGATION PUMPS FOR BANGLADESH

Approved by:

Dr. Jonathan S. Colton, Advisor
School of Mechanical Engineering
Georgia Institute of Technology

Dr. Minami Yoda
School of Mechanical Engineering
Georgia Institute of Technology

Dr. Alexander Alexeev
School of Mechanical Engineering
Georgia Institute of Technology

Date Approved: January 13, 2017

ACKNOWLEDGMENTS

I wish to thank Dr. Timothy J Krupnik, Dr. Md. Abdul Matin, and Dr. Md. Ayub Hossain of the International Maize and Wheat Improvement Center (CIMMYT) – Bangladesh and the Bangladesh Agricultural Research Institute for performing full-scale experiments in local region. All theories of this thesis would not have been validated without their efforts.

I would like to gratefully acknowledge my committee members, Professor Minami Yoda and Professor Alexander Alexeev, for their background and endless support on fluid mechanics theories and computational fluid dynamics simulation techniques.

Above all, I would like to express my deepest appreciation to Dr. Jonathan S. Colton, my advisor for providing the opportunity for me to conduct this research, without whose recognition and guidance I would not be here.

TABLE OF CONTENTS

LIST OF TABLES

LIST OF FIGURES

LIST OF SYMBOLS AND ABBREVIATIONS

AFP	Axial Flow Pump
BBS	Bangladesh Bureau of Statistics
CAD	Computer Aided Design
CFD	Computational Fluid Dynamics
CP	Centrifugal Pump
GDP	Gross Domestic Product
GI	Galvanized Iron
GPM/gpm	Gallons per Minute
IRRI	International Rice Research Institute
MFP	Mixed Flow Pump
R&D	Research and Development
RPM	Revolutions per Minute
STD	Standard Deviation
TmIP	Thai-made Irrigation Pump
U.S.	United States
USD	US Dollars

SUMMARY

Irrigation pumps are indispensable to the production of major crops in Southeast Asia, especially in Bangladesh where agriculture plays a dominant role in the economy. This thesis first analyzes the manufacturing and performance of prototype irrigation pumps, which are manufactured in Bangladesh using a Thai mixed-flow pump model. Then this thesis optimizes the design of the current model in a cost-effective and energy-efficient manner.

This study is based upon several fundamental tenets of fluid mechanics. It begins with the definition of specific speed, which is critical to the pump selection among axial-flow, mixed flow, and centrifugal pumps. The study also discusses friction losses and the Affinity Law concepts, which are incorporated in the analysis of major and minor losses and of scaling at different RPMs.

This study proceeds through multiple stages, including design of experiments, full-scale sample testing, prototype testing, computational fluid dynamics (CFD) simulation in SolidWorks Flow Simulation and ANSYS CFX, and results analysis. The research also involves several advanced techniques such as rapid prototyping, reverse engineering, computer-aided design (CAD), CFD, and analysis of variance (ANOVA) during these stages.

During this study, the results of prototype and CFD simulation demonstrate good agreement with full-scale testing. From this study, several significant outcomes are generated and presented. The six manufactured samples exhibit geometric differences

with an average standard deviation (STD) of 3.6%. These differences have only a small effect on pump performance, with STDs in shut-off head at all RPMs of less than 3.0% in prototype testing, 4.4% in SolidWorks simulation, and 5.6% in CFX simulation. The study implements the friction loss model to the pump system. For full-scale testing rigs, the loss coefficient is found to be 21.75 with a STD of 1.74. For prototype testing rigs, the loss coefficient is found to be 14.2 with a STD of 3.19. The thesis also implements Affinity Law scaling at different RPMs. This is supported by curve fits of the data with R-squared values of greater than 0.9 for flow rate and 0.99 for shut-off head. After that, a method of pump selection is presented for customers to find the most energy efficient pump and its operating condition. Finally, a design optimization of the four major design parameters, along with the significance level of each, is suggested for the current design of Thai mixed flow pump.

CHAPTER 1

INTRODUCTION

Due to different applications and manufacturing conditions, irrigation pumps are constantly optimized to achieve the best performance. This thesis focuses on designing irrigation pumps in a cost effective and energy efficient manner. It can play a critical role in reducing equipment costs and operating expenses, thus improving farmers' overall standard of living in developing regions such as Bangladesh. Such an approach is accomplished through manufacturing in local Bangladesh' factories, as well as by design optimization with CFD simulation. This thesis analyzes the effect of local manufacturing capability on the quality of pump impellers and suggests potential improvements to current design parameters. The sections below introduce the significance of the study and provide an overview of the thesis.

1.1 Irrigation and Rice Production in Southeastern Asia

Irrigation pumps are indispensable to the production of some major crops in Southeastern Asia. By supplying sufficient water for cultivation in the dry season, irrigation pumps benefit rice production. For example, rice harvests can be increased from two per year, which are Aus (planted in March/April and harvested in June/July) and Aman (planted in July/August and harvested in November/December), to three per year by growing rice in the dry season, adding Boro (planted in December/January and harvested in April/May). This requires a pumped irrigation between 12,800 $m^3 ha^{-1}$ and 11,700 $m^3 ha^{-1}$ per season, and emphasizes the necessity of irrigation pumps in Southeastern Asia (Sarker & Ali, 2010).

1.2 Benefit of Efficient and Affordable Irrigation Pumps in Bangladesh

Bangladesh is a densely populated South Asian country bounded by India, Myanmar, and the Bay of Bengal, with a total population of 144 million (*Minor Irrigation Survey Report 2012-13*, June 2013). In this country, agriculture plays a dominant role in its economy. From its Irrigation Survey Report in 2013, for example, Bangladesh has 15.18 million farming households, or 52.9% of the total, cultivating 8.52 million ha, or 57.7% of its total area (*Minor Irrigation Survey Report 2012-13*, June 2013). Among all agricultural products, rice is the major crop and food source in Bangladesh. In fact, with a total area of 1/22 and a total population of 1/9 of India, Bangladesh produces as much as 1/3 of rice production (34.5 million tons) in India. This places it in front of Vietnam and Thailand as the fourth largest rice producing country on the globe (Map of World, February 2016) (Schwartzberg, February 2016).

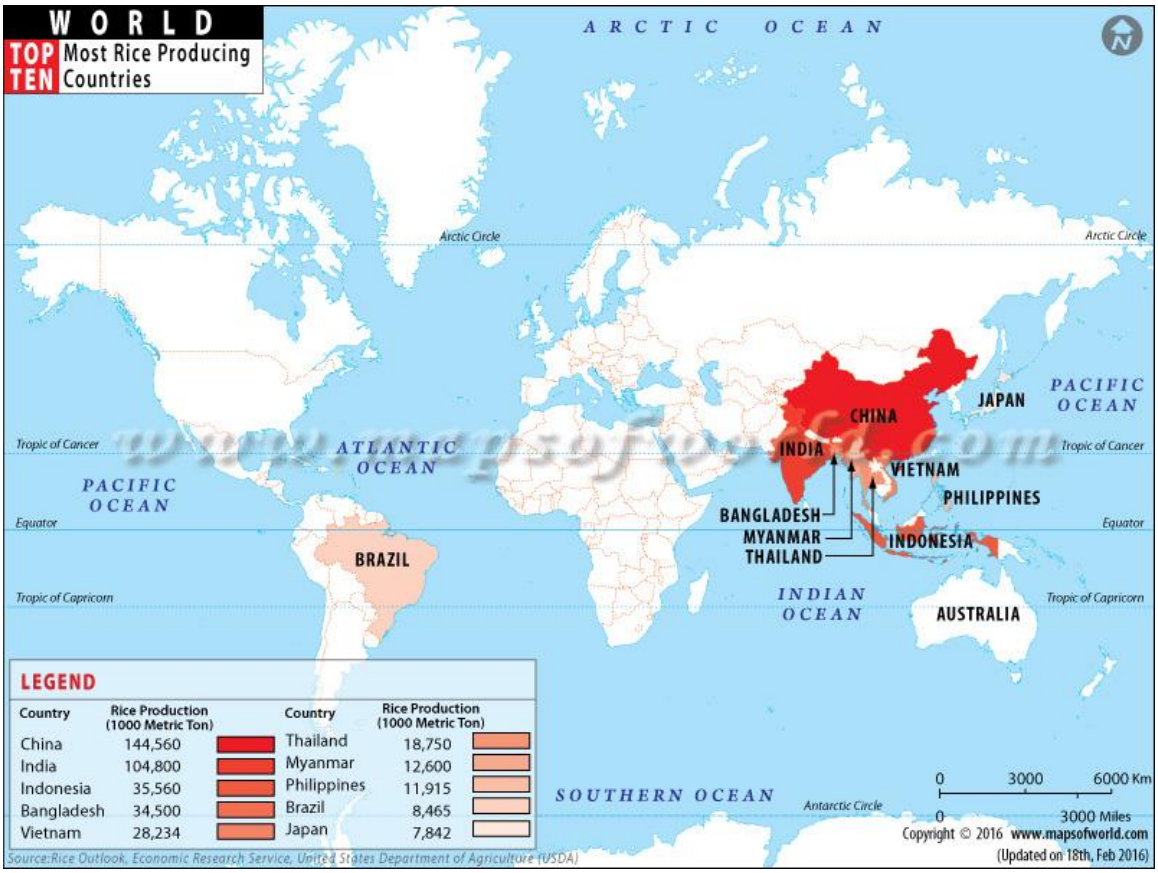

Figure 1.1. Most Rice Producing Countries in the World

However, this large rice production, shown in Figure 1.1, is affected by a major limit on agricultural technology, which constrains its cultivated area per household, cropping intensity, and, finally, the production per capita. For instance, in 2013, the annual GDP per capita in Bangladesh was $1,044, less than 1/10 of the world average and half of the average monthly income in the United States (World Bank Group, 2016). Moreover, this tremendous demand for rice will only increase in the near future. Two research studies in 2010 and 2011 project that population growth and increases in per capita income will require an expansion of global food requirements for at least the next four decades before they plateau, which implies that a doubling of the current staple crop production will be required by 2050 (Godfray, et al., 2010, Tilman, et al., 2011). This trend line provides an even greater challenge to the farmers of Bangladesh, who are not

only seeking to increase their own living standard, but also to feed a growing population of which 43% are living below the poverty line at $1.90 per day (World Bank Group, 2016).

The issues and challenges mentioned above drives Bangladesh towards agricultural mechanization, which frees people from basic labor and augments the rice production per unit farmland. For example, by utilizing low lift pumps, such as AFP or MFP, to carry surface water to fields, a study, shown in Figure 1.2, indicates that over 20,000 ha of fallow land and 100,000 ha of low-intensity cropland can be brought into intensified production. This results in an increase of annual cultivation cycles from 0 - 1 to 2 – 3 (Schulthess et al., 2015). Therefore, the Bangladesh government has been giving special emphasis to mechanization and related issues, such as a 25% subsidy to the farmers to purchase machinery (Bangladesh Agricultural Development Corporation, June 2013). Because of the current economic conditions in Bangladesh, most pumps are manufactured in-country to reduce costs, rather than imported from countries with mature technology, such as Thailand and Indonesia. Due to its limited R&D and manufacturing capabilities, assistance from developed countries, such as the United States, on the design and manufacture of an easy-to-use and energy-efficient irrigation pump offers a desirable solution to Bangladeshis living below poverty line.

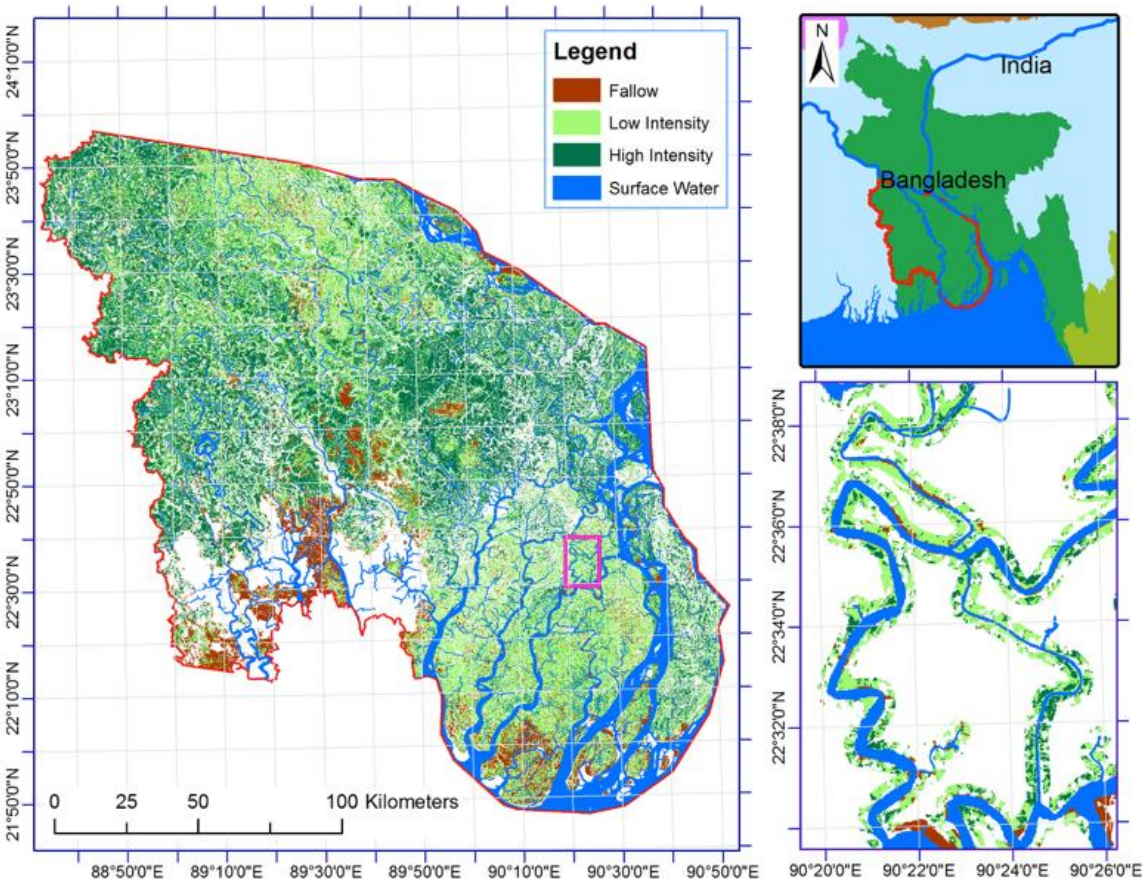

Figure 1.2. Land Use Intensity of Cropland during the 2014 Rabi Season in Southern Bangladesh. (Schulthess et al., 2015)

1.3 Thesis Overview

This thesis is organized in the following manner. Chapter 1 covers the purpose and scope of the study, as well as a project overview. Chapter 2 covers the history and background information of the development of irrigation pumps in the south Asia. It also introduces the AFP model used in this study. Chapter 3 provides the important principles associated with pumps, such as pump selection, scaling, Bernoulli's Equation, and losses, which are essential to understand the experiments and their analyses. Chapter 4 describes the test apparatus and procedures. Chapter 5 describes the approach and problem setup of

the CFD simulation using ANSYS Fluent. Chapter 6 then discusses and analyzes the results from the previous two sections. The results from the experiments at different scales and the simulations are compared using the models developed in Chapter 3. Finally, Chapter 7 concludes the thesis with a summary and plans for future work.

CHAPTER 2

DEVELOPMENT OF IRRIGATION PUMPS

2.1 Application of Irrigation Pumps among Developing Asian Countries

The introduction of irrigation pumps is a milestone for the Asian agricultural industry. Beginning in the early 1960s, small-scale irrigation pumps were introduced to developing Asian countries during the Vietnam War (Biggs, 2011). These pumps first appeared as engines taken from small tractors and mounted on a water pump and enabled farmers to irrigate crops and doubled their yields. Higher yields then permitted purchase of other engines, such as from Honda motorbikes, generators, and sewing machines. Soon, almost every household managed to acquire one. The popularity of these small-scale irrigation pumps grew exponentially. Rarely a moment existed in the rivers or fields when one did not hear the percussive rattling of a motor. Since then, the practice of adopting water pumps to multiply harvests gradually became the norm today. Irrigation pumps played a vital role in what is called the Silent Revolution (Molle, Shah and Barker, 2003).

To understand the sizes and types of Asian irrigation pumps, one must consider social background and geography. Their size is mostly determined by the social structure of Asian countries. Influenced by the Communist party, irrigation was traditionally managed by “big engines,” or state-owned large water pumping stations and canals (Biggs, 2011). As Southeast Asian countries shifted their economic structure to individual control, small-scale irrigation pumps swiftly gained popularity among

individual farmers. For this reason, pipe diameters are often limited to 4 - 6 inches (10 – 15 cm).

Geography helps determine the type of irrigation pumps used by farmers. Pumps can generally be categorized into three types – axial flow pumps (AFP), mixed flow pumps (MFP), and centrifugal pumps (CP). Generally, AFPs are designed to pump at low lift with high capacity, of which the head limit for AFPs is approximately 10 feet (SCS National Engineering Handbook). MFPs are also designed for high capacity, but at moderate lifts. They operate efficiently at heads of 6 – 25 feet (1.8 – 7.6 m). Compared to CPs, AFPs and MFPs exhibit the advantage of low initial cost, high capacity of delivery, nearly constant flow, and substantially higher powering efficiency within their operating range. Hence, AFPs and MFPs are very appropriate for lowland farming countries, such as Vietnam, Thailand, Philippines, and Bangladesh (Stickney and Salazar, 1989). Figure 2.1 shows a schematic of an exemplar axial flow irrigation pump. A detailed definition and a technical description of the three types of pumps are provided in Section 3.1.

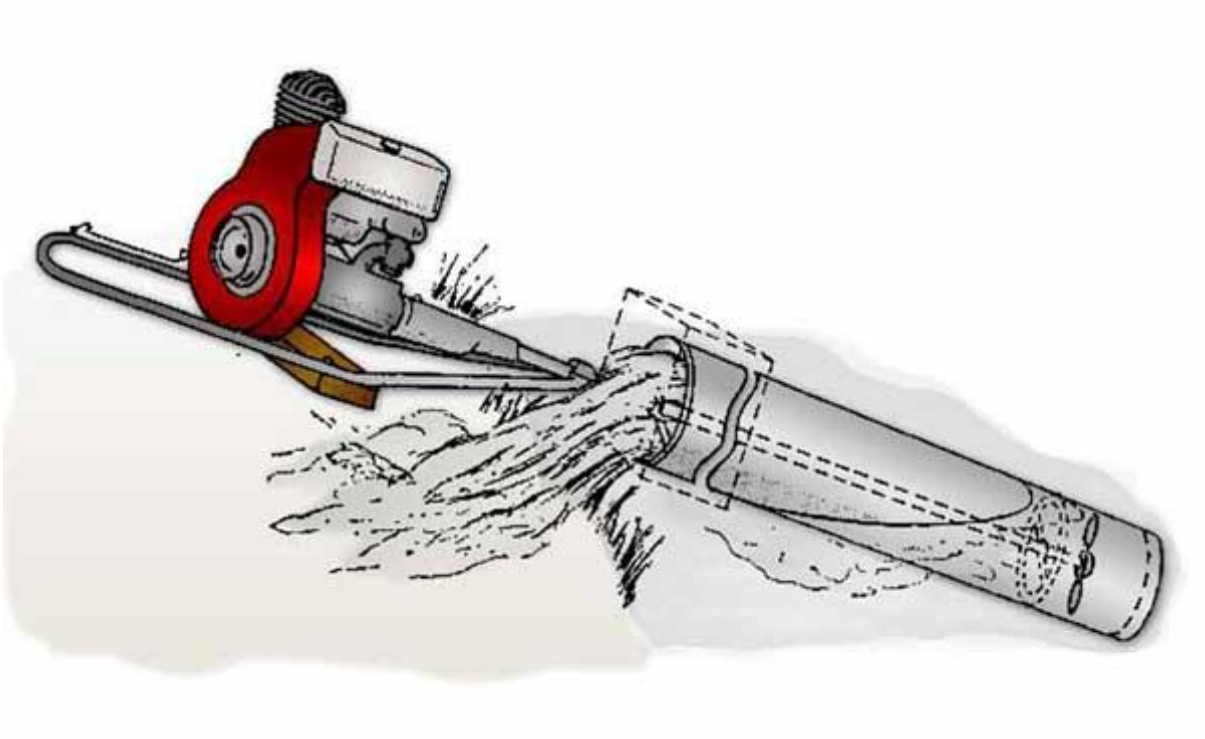

Figure 2.1. Small Engine Irrigation Pump (Biggs, 2011)

Based on the above discussion, this thesis focuses on the study of propeller pumps (AFPs and MFPs). The rest of the chapter reviews previous designs of propeller pumps, and analyzes a popular current product.

2.2 Previous Irrigation Pump Studies

Before irrigation pumps were introduced in Southeast Asia, the wooden trough water lift had been the primary irrigation device. The initial AFP in Thailand was designed and demonstrated to the public in 1941 as a simple, low price, and efficient low lift pump that small manufacturers and farmers could fabricate themselves (Chinsuwan, 1985). In this initial design, most components were made from wood. It used square pipe and nine impellers to complete the lifting. The pump outperformed the traditional wooden trough water lift in capacity.

The initial design was not commercially available until 1957, when several modifications were made. For example, the material of pipes was replaced by sheet steel, and only one impeller, attached to the suction end, was used. A small 4-wheel tractor was introduced as a power source. The pump performed at 2347 L/min at a head of 0.80 m and an impeller speed of 1500 RPM. This is much higher than that of the wooden trough water lift (1700 L/min) when operated at the same conditions (Sidnarane and Limptrakul, 1973). Since its first dissemination, an estimated total of 80,000 units were fabricated in a 10-year period (Tavakul, 1967). During this process, further modifications were adopted, such as the change of impeller to a three-blade impeller as shown in Figure 2.2. Variations of the product were also developed for wider application, including as boat propellers.

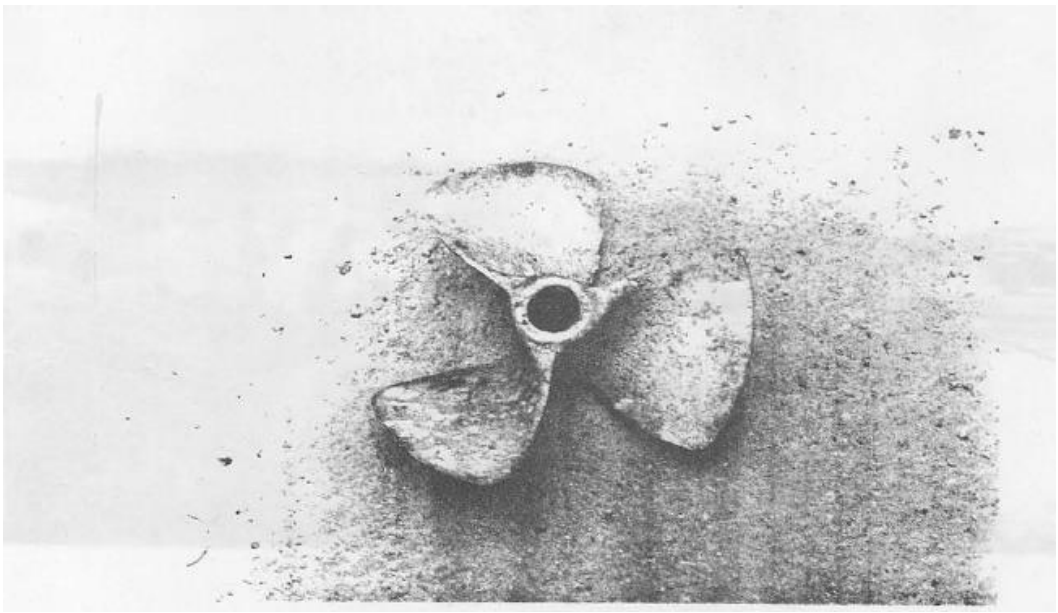

Figure 2.2. Three-Blade Impeller (Chinsuwan,1985)

AFPs make single cropping possible in some areas and double cropping in others. Besides that, continuous cropping of paddy in the central plain of Thailand is also a result

of AFPs. In 1985, the number of AFPs in use in Thailand rapidly increased to 600,000, approximately 70% of all pumps in the country, and irrigated over 9 Mha of rice (Chinsuwan, 1985). As discussed in Section 2.1, a major factor for the wide adoption was the low cost of purchase. Due to the simple design, high volume of sales, and competition among manufacturers, the price of a 13 cm diameter and 3 m long pump was USD 22.22 in 1971 and USD 33.33 in 1985. The maintenance cost was modest as well. Indicated by a farmer in Pathumthani province in Thailand, the total annual cost was as low as USD 2.5 per ton of rice yielded. Pumps of similar designs are still being produced today. In 2014, the cost of a 15-cm inner diameter by 6-m long MFP, rated by the manufacturer to deliver 50 l/s at 5 meters of head and 900 RPM, was USD 250 (PattanaKarnkol).

A similar study was performed by the Engineering Department of the International Rice Research Institute (IRRI) in the Philippines (The International Rice Research Institute, 1983). As shown in Figure 2.3, this simple design reduced the cost and labor required for rural fabricators. The pump had an inner diameter of 15 cm and was built with rolled 1.6 mm sheet metal for use with a 5 HP petrol engine. At 2200 RPM, the pump was rated for 50 L/s at 1.5 m lift. When compared to a similar CP, the tests showed that fuel efficiency was tripled at 1 m lift and doubled at 2.8 m lift. In addition, the cost of switching from a 14.3 L/s, 10-cm CP to a 40 L/s, 15-cm AFP could be covered by the fuel savings in only one year, considering pumping 100 ha-cm on a 5-ha field. Nevertheless, it is worth noting that the AFP lifespan is 5 years due to its low cost and light weight, as compared to that of 15 years in the case of CP. By 1988, over 500 AFPs were produced for rice and prawn farmers, of which the 15-cm AFP was priced at USD 50 (Stickney & Salazar, 1989).

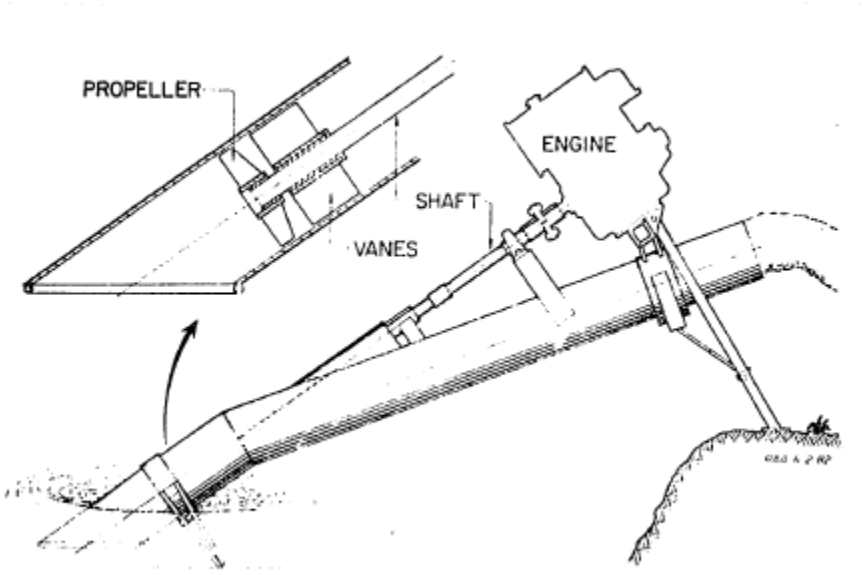

Figure 2.3. Schematic of IRRI AFP (IRRI, 1983)

Two years later, further research was conducted by IRRI to study specifically the design parameters affecting the performance of the IRRI-designed AFP discussed in the previous paragraph (Aban and International Rice Research Institute, 1985). Testing was conducted on the water irrigation system shown in Figure 2.4. It involved a pipe of 4.2 m long and 12 cm in diameter, a steel impeller coupled to a 1.9 cm (0.75 in) line-shaft, and a 5 hp (3.73 kW) gasoline engine. The experiment reported a highest efficiency of 40% at a flow rate of 1900 L/min, an impeller speed of 2330 RPM, and a total head of 1.8 m. This research also demonstrated the influence of various design parameters. Results showed that pump efficiency depended greatly on the shape of the inlet, the impeller vane discharge angle was related directly to the head-capacity characteristics, the loss in capacity due to leakage increased with the clearance between the impeller and the inner wall of the pipe, and finally, the diffusion vane angle was not a critical design parameter.

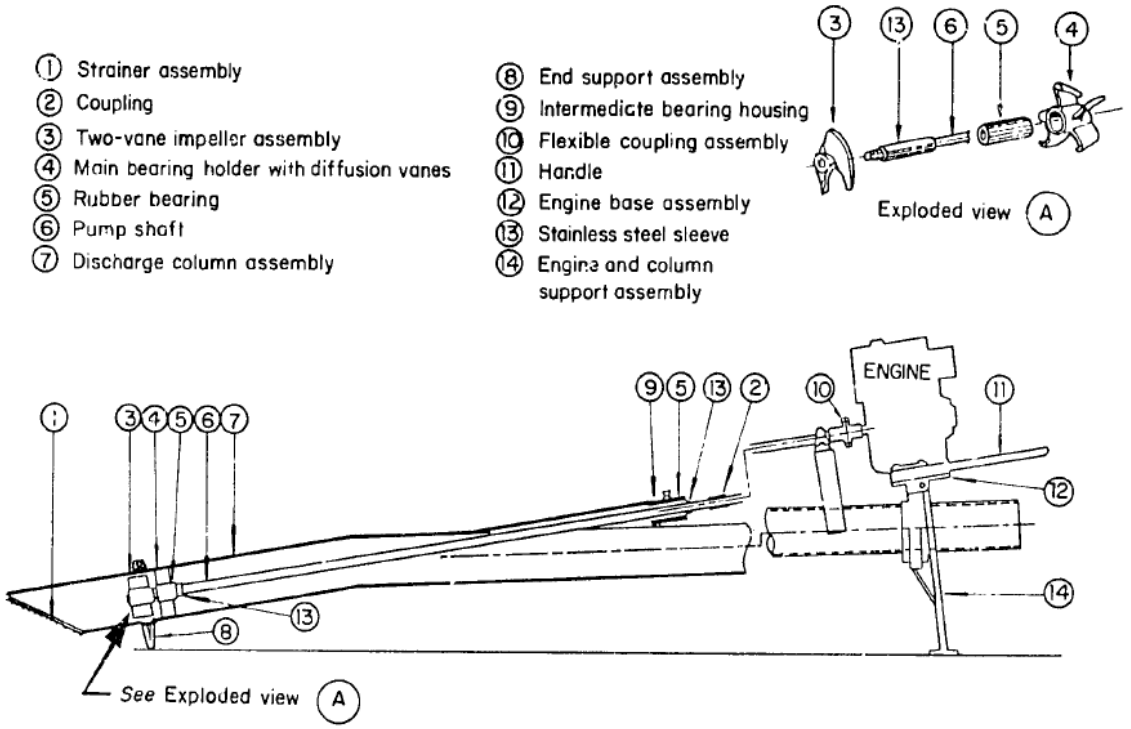

Figure 2.4. Schematic of Water Irrigation System by IRRI (Aban and IRRI, 1985)

In recent years, the technique of numerical simulation was used to study propeller pumps of complex geometries. In 2011, a study on the geometry of MFP in an internal impeller flow was presented (Varchola and Hlbocan, 2012). By calculating the pressure distribution along streamlines in the computational domain, the study determined an optimum design in terms of energy efficiency, as shown in Figure 2.5, and demonstrated its performance at various operating conditions. At its most efficient operating point, the MFP obtained a theoretical mechanical efficiency of greater than 75%.

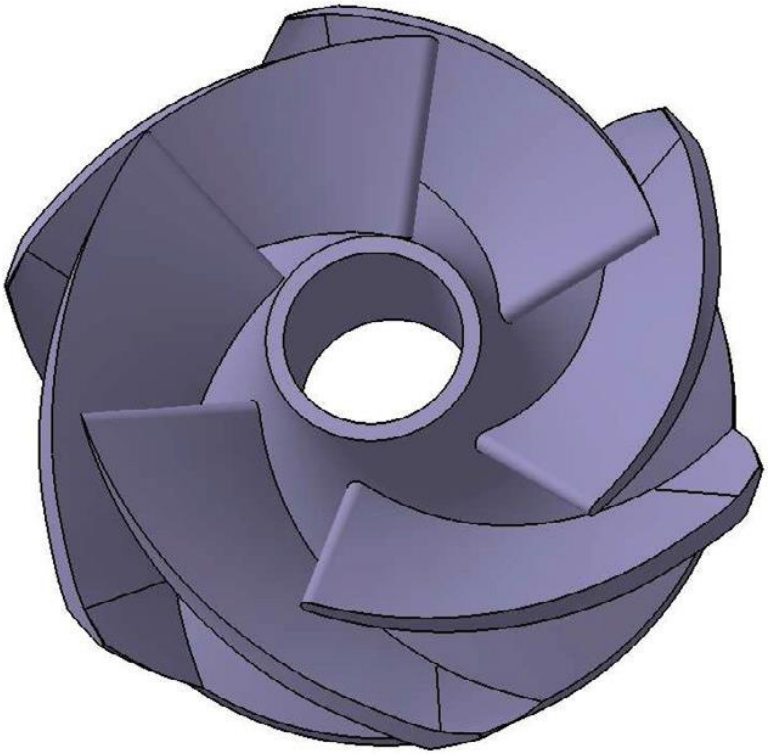

Figure 2.5. Optimum MFP Design based on Linear Distribution of Pressure

Using this numerical simulation technique, more studies on pumps were performed, such as the Thai AFP model presented in the next section.

2.3 Thai Irrigation Pump Model

In 2014, an investigation on a popular commercial Thai-made irrigation pump (TmIP) impeller was conducted using the technique of computational fluid dynamics (CFD) (Kasantikul and Laksitanonta, 2014). Similar to the previous study, the study on the TmIP attempted to optimize the design in terms of energy efficiency by analyzing the effects of various design parameters. This research investigated four factors: the influence of number of blades, the influence of length of blades, the influence of hub height, and the cavitation of the blades. A schematic of the TmIP is shown in Figures 2.6 and 2.7, with the hub colored in blue.

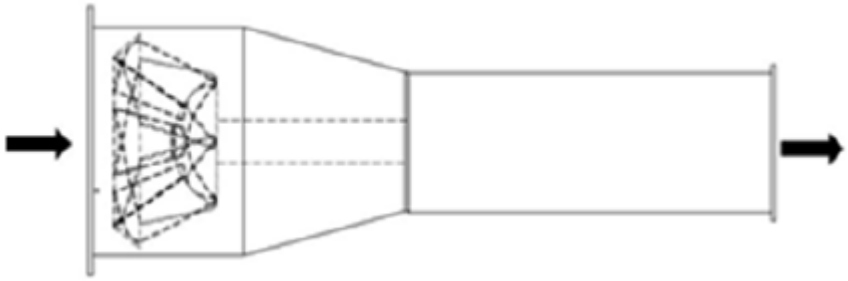

Figure 2.6. TmIP (Kasantikul and Laksitanonta, 2014)

Figure 2.7. Impeller of TmIP (Kasantikul and Laksitanonta, 2014)

This research used ANSYS CFX to numerically analyze the flow phenomenon and the effects of geometric factors on the TmIP efficiency (Kasantikul and Laksitanonta, 2014). The definition of each geometric factor is shown in Figures 2.8 and 2.9. The optimum design of geometry had following parameters: the number of blades was six, the length of the blade was 120 mm, the height of the hub was 45 mm, the blade inlet angle was 54°, the blade outlet angle was 68°, and an operation range of 700 to 1100 RPM. The study experimentally compared the performance of the new design with that of the

original TmIP on market. At an impeller speed of 1000 RPM, the original TmIP had a flow rate of 57.7 L/s, a total head pressure of 4.28 m, and an efficiency of 56.08%, whereas the new design when operated at 1100 RPM had a flow rate of 50.53 L/s, a total head pressure of 4.82 m, and an efficiency of 69.65%. Overall, the flow rate for the optimized design decreased 12.43%, the total head pressure increased 12.86%, and the efficiency increased 13.57%.

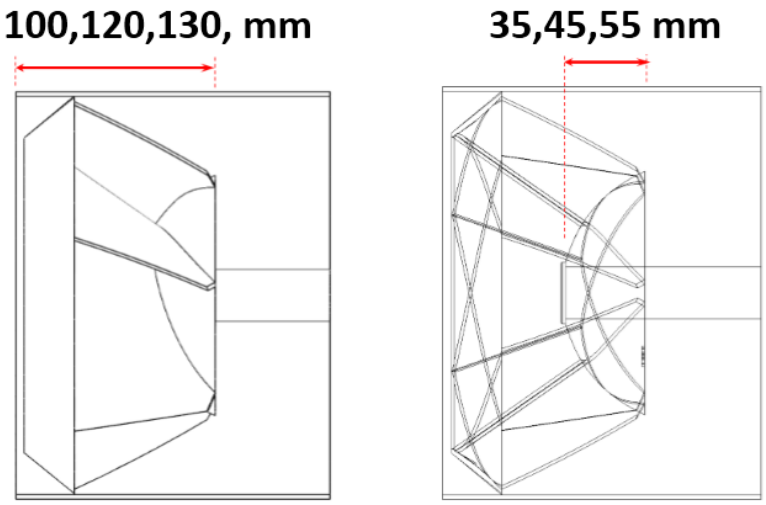

Figure 2.8. Variations of the Length of Blade (L) and the Height of Hub (R) (Kasantikul and Laksitanonta, 2014)

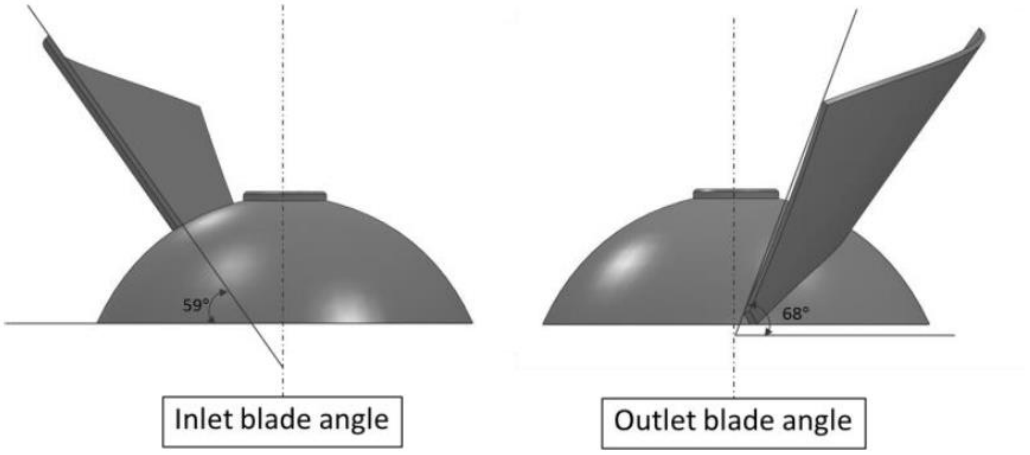

Figure 2.9. Inlet and Outlet Blade Angle (Kasantikul and Laksitanonta, 2014)

The results of this research demonstrated the effects of geometric factors on the performance of TmIP. It also validated the potential of customizing the design parameters to satisfy the needs of different operating conditions. Because of the similarity in geometry between TmIP impellers and irrigation pump impellers manufactured in Bangladesh, this research is used as a reference for the study in this thesis. However, due to the neglect of other components in the irrigation system, such as motor, pipe, etc., and the limited variation on head and impeller speed, this study can be further specified to suit the needs of the Bangladesh people and integrated into with the other components of the irrigation system. This study can also be further validated for local farmers by field testing using locally manufactured samples in Bangladesh. Room for improvements in the TmIP study motivated more research on propeller pumps, such as this thesis.

2.4 Chapter Summary

This chapter discussed the development of irrigation pumps in Southeastern Asia and previous studies on AFPs and MFPs in irrigation. Early designs and the use of

numerical approaches to optimize recent pump models were presented and discussed. Due to the similarity between the pump model in this thesis and the TmIP, the research results in Section 2.3 serve both as a reference and guide for this thesis, and was thus reviewed in detail.

With this background information, the next chapter presents fluid mechanics and numerical simulation principles relevant to this project.

CHAPTER 3

THEORETICAL PRINCIPLES

This chapter presents a synopsis of the principles applicable to this research. It begins with the identification of axial flow pumps (AFP), mixed flow pumps (MFP), and centrifugal pumps (CP) based upon their operational ranges in terms of specific speed. Then, this chapter introduces the principles of major and minor losses, which are used to estimate the friction loss factors associated with each component. After that, the Affinity Law is discussed to relate the small-scale prototype test results from Georgia Tech to the full-scale test results from Bangladesh. Finally, the models involved in the computational fluid dynamics (CFD) simulations are introduced.

3.1 Specific Speed and Pump Selection

In common engineering usage, a pump is a piece of turbomachinery that adds energy to a fluid. Pumps may be classified into two categories: dynamic, in which energy is continuously added to increase the fluid velocities within the machine to values greater than those occurring at the discharge such that subsequent velocity reduction within or beyond the pump produces a pressure increase; and displacement, in which energy is periodically added by application of force to one or more movable boundaries of any desired number of enclosed, fluid-containing volumes, resulting in a direct increase in pressure up to the value required to move the fluid through valves or ports into the discharge line (Wilcox, 2000).

In this thesis, only a subcategory of the dynamic pumps that involves rotary motion is considered. In this manner, the great variety of pumps can be reduced to a few

fundamental hydraulic types based on the direction of the flow through the rotor. Among them are AFPs, MFPs, and CPs. By definition, AFPs generate flow in axial direction $\hat{\mathbf{z}}$, CPs generate flow in radial direction $\hat{\mathbf{r}}$, and MFPs generate flow in both directions. In terms of applications, AFPs are used to pump large flow rates through a small pressure difference, CPs are used to pump small flow rates through a large pressure difference, and MFPs are in between AFPs and CPs.

A commonly used dimensionless term to describe the application range of different types of pumps is specific speed, N_s, which is defined in Equation 3.1,

$$N_s = \frac{N\sqrt{Q}}{(gh_a)^{3/4}} \qquad \textit{Equation 3.1}$$

where N is the shaft speed, Q is the volumetric flow rate, g is the gravitational constant, and h_a is the head. In U.S. customary units, a dimensional form of this concept is expressed in Equation 3.2.

$$N_{sd} = \frac{N\sqrt{Q}}{(h_a)^{3/4}} \qquad \textit{Equation 3.2}$$

In this case, N is expressed in rpm, Q is expressed in gpm, and h_a is expressed in ft, so in U.S. customary units = [rev·gal$^{1/2}$·min$^{-3/2}$·ft$^{3/4}$].

Physically, the specific speed is the operating speed at which a pump produces unit head at unit volume flow rate. Low specific speeds ($N_{sd} < 4000$) typically correspond to the most efficient operation conditions for centrifugal-flow pumps, moderate specific speeds typically correspond to design points for mixed-flow pumps, and high specific speeds ($N_{sd} > 9000$) correspond to the most efficient operation of axial-flow pumps. This concept is shown in Figure 3.1. Based on this concept, AFPs are suited for applications

with high flow rate and low head, CPs are best suited for that with large head and small flow rate, and MFPs operate between the other two.

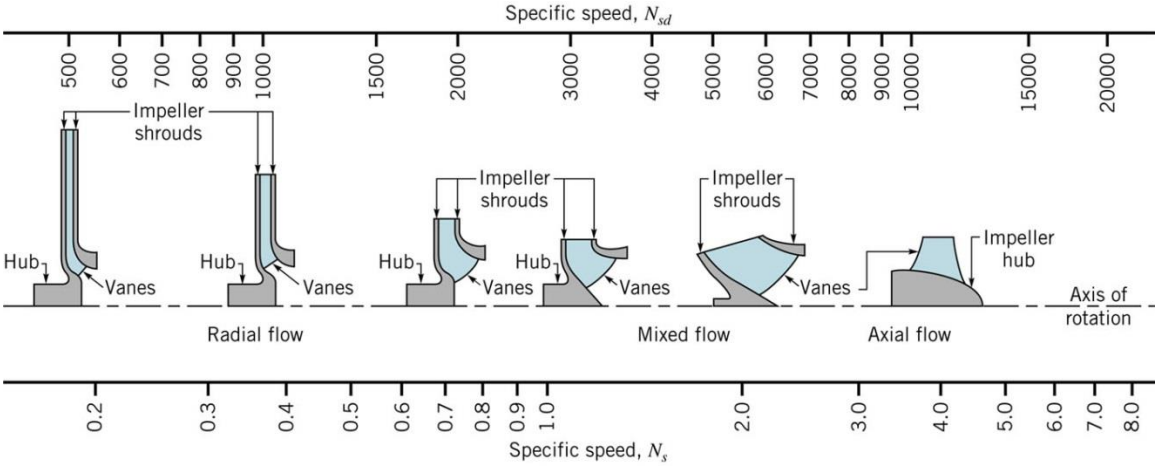

Figure 3.1. Pump Selection based on Specific Speed (Fig. 12.18 in Wilcox, 2000)

3.2 Major and Minor Losses

To study the characteristics of pipe flow in a pump system, it is necessary to account for the head loss. The head loss consists of a head loss due to viscous effects in the straight pipes, termed the major loss, $h_{L\,\text{major}}$, and a head loss due to geometry of pipe components, termed the minor loss, $h_{L\,\text{minor}}$ (Munson, Okiishi, and Huebsch, 2009).

Assuming a steady incompressible flow with a pipe of constant diameter, the major loss, $h_{L\,\text{major}}$, is defined in Equation 3.3,

$$h_{L\,\text{major}} = f\frac{l}{D}\frac{V^2}{2g} \qquad \textit{Equation 3.3}$$

where l is the length of the pipe, D is the diameter of the pipe, V is the velocity of the fluid, g is the gravitation constant, and $f = \phi(Re, \frac{\epsilon}{D})$ is the friction factor that is a function of Reynolds Number, Re, and relative roughness, $\frac{\epsilon}{D}$. In the case of laminar flow,

f is simplified to $f = 64/Re$. In general, f can be determined from the Moody Chart provided in Figure 3.2 (Munson, Okiishi, and Huebsch, 2009).

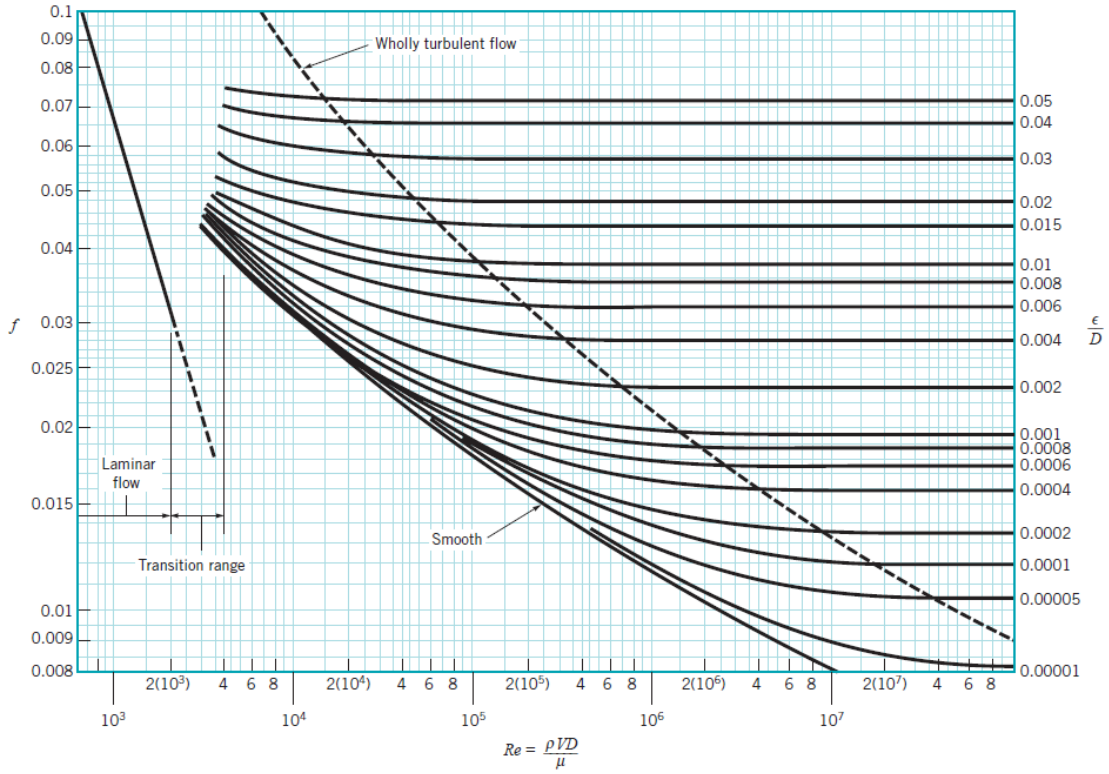

Figure 3.2. The Moody Chart (Fig. 8.20 in Wilcox, 2000)

The minor loss, $h_{L\,\text{minor}}$, is commonly determined by the specification of the loss coefficient, K_L, is defined in Equation 3.4.

$$h_{L\,\text{minor}} = K_L \frac{V^2}{2g} \qquad \textit{Equation 3.4}$$

Note that the loss coefficient, K_L, is dimensionless and is dependent only on the geometry of the component. In this thesis, most K_L values are obtained from the reference *Flow of Fluid through Valves, Fittings and Pipe* by Crane (Crane Co. Engineering Division, 2012).

With the addition of head loss and pump head, the modified Bernoulli Equation, also known as the Steady 1-Dimensional Energy Equation and shown in Equation 3.5, can be used to characterize the flow profiles across a pump system (Wilcox, 2000).

$$\left(\frac{V^2}{2g} + z + \frac{p}{\rho g}\right)_1 - \left(\frac{V^2}{2g} + z + \frac{p}{\rho g}\right)_2 = h_L - \frac{w_p}{g} \qquad \textit{Equation 3.5}$$

where $\frac{V^2}{2g}$ is the velocity head, z is the elevation head, $\frac{p}{\rho g}$ is the pressure head, $h_L = h_{L\,\text{major}} + h_{L\,\text{minor}}$ is the head loss, $-\frac{w_p}{g}$ is the pump head, and w_p is the water power.

In practice, the head loss is first estimated from the geometry of the pump system and then validated by experiments. With the values of the head losses of the pump and of the control-measurement sections that are used for testing that will be described in Section 6.1.2, the actual pump performance in the field (without measurement equipment) can be estimated. This approach is further discussed in Section 4.1.

3.3 Dimensional Analysis and Affinity Law

The application of dimensional analysis to problems of similitude in the study of turbomachinery is a useful tool. It reveals the functional relationships among the quantities involved and establishes dimensionless criteria of flow for dynamically similar conditions. It also shows the way to evaluate various factors affecting the flow. As the principal of dimensional analysis requires that all of the terms of a correct and complete physical equation have the same dimensions, dimensional analysis facilitates the development of constants in dimensionless forms that allow one to draw conclusions regarding the behavior of turbomachinery. In the case of pumps, the study of dimensional analysis begins with the common quantities listed in Table 3.1. (Stepanoff, 1957)

Table 3.1. Common Quantities to Describe Pumps' Behavior

Abbreviation	Name	Dimension
H	Pump head	l
Q	Discharge rate	l^3/t
N	Speed in RPM	l/t
D	Impeller diameter	l
g	Gravitational constant	l/t^2
ρ	Fluid density	m/l^3
μ	Absolute viscosity	m/lt
$E = gH$	Energy applied to the shaft	l^2/t^2

In this case, the energy applied to the shaft, $E = gH$, will be used instead of head because it includes the gravitational constant. This reduces the number of quantities necessary to describe the pump's operation to six, which can be expressed in a general functional equation Equation 3.6.

$$f(Q, E, N, D, \rho, \mu) = 0 \qquad \textit{Equation 3.6}$$

These quantities can be measured by three fundamental unites: length (*l*), time (*t*), and mass (*m*). Based on a theorem of dimensional analysis, a complete equation describing the relation among n (6) different quantities measured with k (3) fundamental units can be reduced to the form

$$f(\pi_1, \pi_2, \ldots \pi_{n-k}) = 0 \qquad \textit{Equation 3.7}$$

or in this case, $$f(\pi_1, \pi_2, \pi_3) = 0$$ *Equation 3.8*

where π_i represents a dimensionless product expressed as

$$\pi = Q^a E^b N^c D^d \rho^e \mu^g$$ *Equation 3.9*

By selecting E, D, ρ as three independents, π_1, π_2, π_3 can be expressed as in Equation 3.10

$$\begin{aligned} \pi_1 &= E^{x_1} D^{y_1} \rho^{z_1} Q \\ \pi_2 &= E^{x_2} D^{y_2} \rho^{z_2} N \\ \pi_3 &= E^{x_3} D^{y_3} \rho^{z_3} \mu \end{aligned}$$ *Equation 3.10*

where x, y, z are unknown exponents. When solved, these equations yield

$$\pi_1 = \frac{Q}{E^{\frac{1}{2}} D^2} = \frac{Q}{(gH)^{\frac{1}{2}} D^2}$$ *Equation 3.11*

$$\pi_2 = \frac{ND}{E^{\frac{1}{2}}} = \frac{ND}{(gH)^{\frac{1}{2}}}$$ *Equation 3.12*

$$\pi_3 = \frac{\mu}{\rho D E^{\frac{1}{2}}} = \frac{\mu}{\rho D (gH)^{\frac{1}{2}}}$$ *Equation 3.13*

Using the same logic, additional dimensionless parameters can be developed. As shown by Stepanoff in 1957, these dimensionless parameters include the Reynolds Number in Equation 3.14 and specific speed in Equation 3.15,

$$Re = \pi_1 \pi_2 = \frac{Q\rho}{\mu D}$$ *Equation 3.14*

$$N_s = \pi_2^{\frac{1}{2}} \pi_3 = \frac{N Q^{\frac{1}{2}}}{(gH)^{\frac{3}{4}}}$$ *Equation 3.15*

One may also derive the Affinity Law for a family of geometrically similar centrifugal pumps from dimensional analysis. The Affinity Law is used for scaling between pumps of similar geometry. Here, it is used to compare results from prototype tests performed at Georgia Tech and full-scale tests performed in Bangladesh. The derivation of the Affinity Law begins with defining the two additional dimensionless parameters in Equation 3.16 and 3.17 from the three independent parameters, π_1, π_2, π_3,

$$\pi_6 = \frac{\pi_2}{\pi_3} = \frac{Q}{ND^3} \qquad \textit{Equation 3.16}$$

$$\pi_7 = \frac{1}{\pi_3^2} = \frac{gH}{N^2D^2} \qquad \textit{Equation 3.17}$$

By keeping π_6 and π_7 constant among geometrically similar pumps with different rotational speeds and diameters, the Affinity Law can be expressed by Equations 3.18 and 3.19 (Stepanoff, 1957).

$$\frac{Q_1}{Q_2} = \frac{N_1}{N_2}\left(\frac{D_1}{D_2}\right)^3 \qquad \textit{Equation 3.18}$$

$$\frac{H_1}{H_2} = \left(\frac{N_1 D_1}{N_2 D_2}\right)^2 \qquad \textit{Equation 3.19}$$

where Q is the volumetric flow rate, H is the pressure head, N is the shaft rotational speed, and D is the impeller diameter. Note that this law only applies to geometrically similar impellers.

Although the Affinity Law stands theoretically, stated in *Pump Handbook* "[t]he assumptions [on which it is] based are rarely if ever fulfilled in practice, so exact predictions by the equations should not be expected" (Karassik, Messina, and Cooper, 2007). In this thesis, the Affinity Law is tested in Chapter 6.

3.4 Chapter Summary

This chapter presents the principles associated with the experiments and analyses of this thesis. It introduces the concept of specific speed, major and minor head losses, and the Affinity Law. Specific speed helps one to select the most efficient type of pump at a given operating condition. Major and minor losses are used to analyze the resistance in a pump system and to predict the real performance without the control-measurement segment of the pump system. The Affinity Law for scaling is used to correlate the prototype and full-scale testing. With the above principles being addressed, this thesis is ready to describe the procedures for prototype- and full-scale testing.

CHAPTER 4

EXPERIMENTAL METHODS AND PROCEDURES

In this study, experimental testing is performed on full-scale samples and prototypes to evaluate the performance and effectiveness of the locally-manufactured axial flow pumps. Full-scale sample testing is performed in Bangladesh, using impeller samples produced by standard manufacturing processes. Prototype tests are performed at Georgia Tech using impellers produced by rapid prototyping techniques. Impellers used in both tests have the same geometry, but different scales. Due to different equipment availability, the testing apparatus exhibit similar, but not identical, geometries. These differences, mostly in scaling and flow resistances, are analyzed using the major and minor losses and scaling principles presented in Chapter 5. The testing procedure and apparatus are recorded in detail to capture these differences.

4.1 Full-Scale Sample Testing

Full-scale testing evaluates the performance of six 6-inch diameter pump impellers of the same nominal design. These pump impellers produced from iron replicating the geometry of a commercial Thai AFP impeller. An exemplar impeller is shown in Figure 4.1 below. Because of variations in the manufacturing process, each impeller has a slightly different geometry, and thus expected performance.

Figure 4.1. AFP Impeller

The test apparatus is composed of two parts, the AFP section and the control-measurement section. The AFP section is shown in Figures 4.2 and 4.3, with detailed CAD schematics in Figures 4.4 and 4.5. It includes a 6-in AFP impeller, a 6-in galvanized iron (GI) pipe with a length of 6 m, a shaft at the center of the pipe, a V-belt power coupling consisting of two pulleys, a weight scale, an external fuel tank, and a Changchai S195 Diesel Engine. The impeller is attached to the end of the shaft and placed at the inlet of the GI pipe. A shaft bearing and a diffuse vane are located within the pipe to center the shaft. A cage is placed at the inlet to filter stones and fish from the water. The inlet of the pipe is slightly enlarged, and the outlet is bent at a 45˚angle. During the experiment, the impeller is submerged under water. The engine drives the shaft at various testing RPMs through a V-belt.

Figure 4.2. AFP Section 1

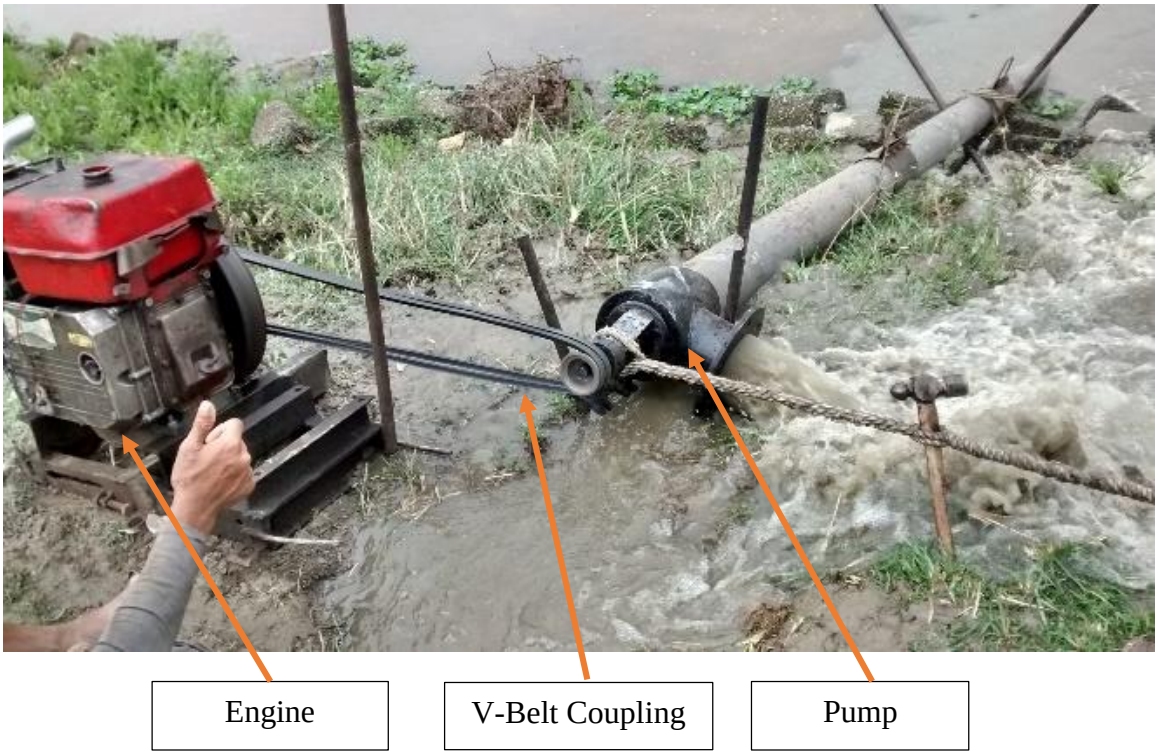

Figure 4.3. AFP Section 2

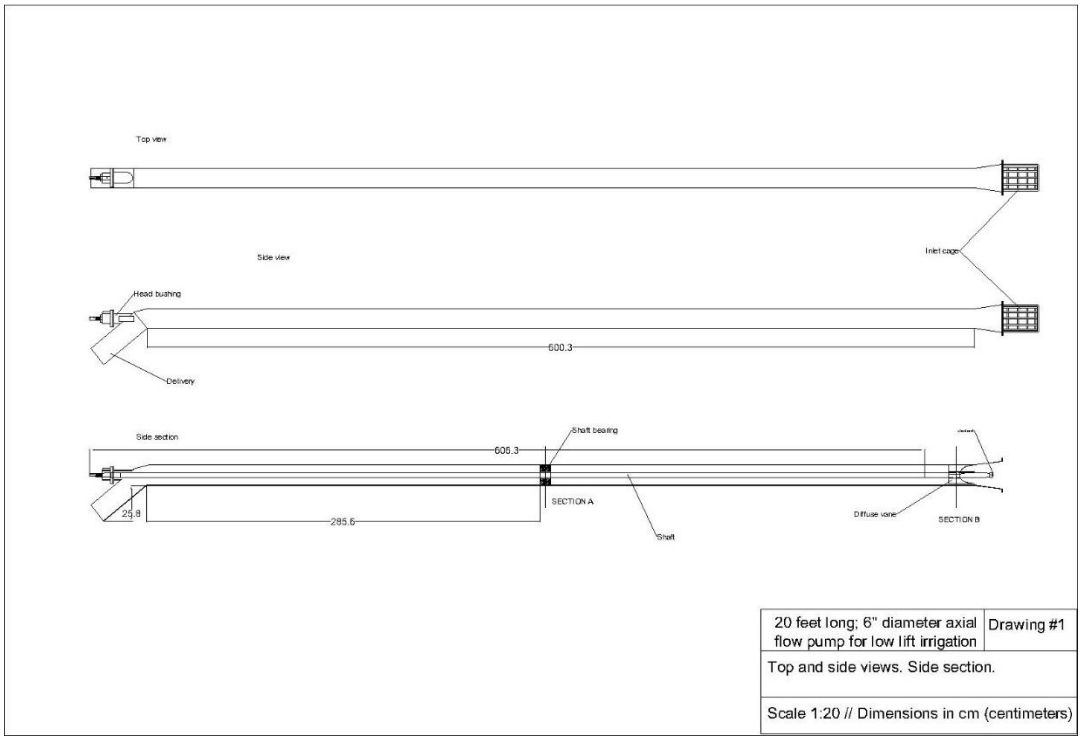

Figure 4.4: The AFP Section CAD Drawing 1

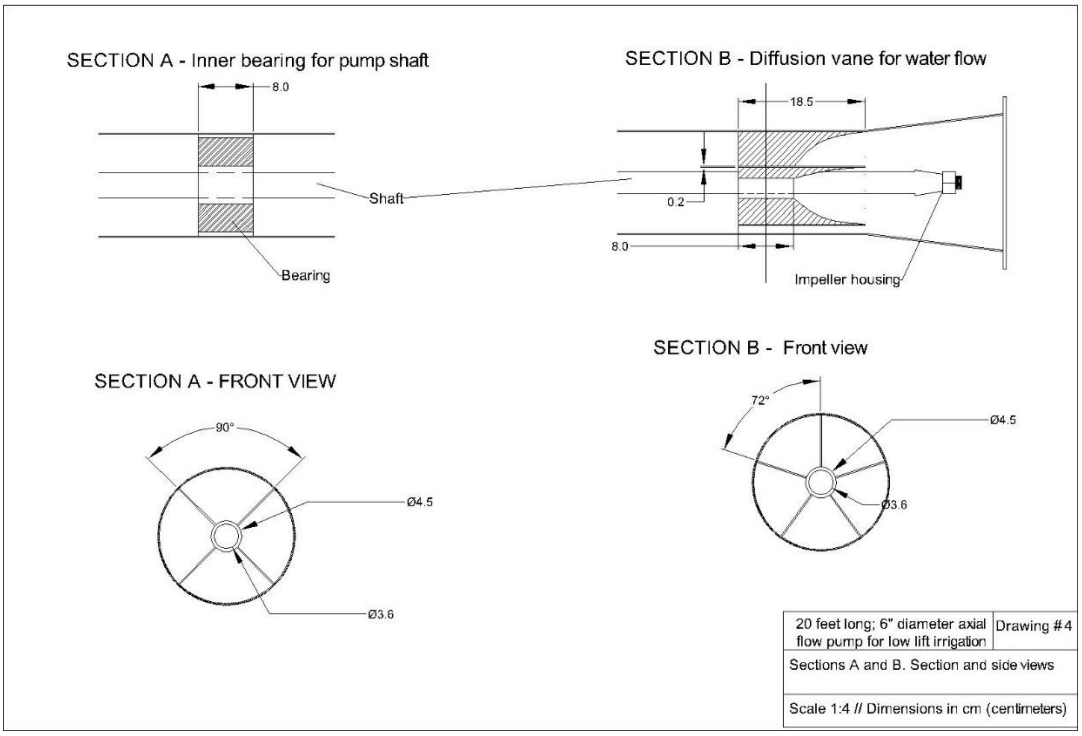

Figure 4.5: The AFP Section CAD Drawing 2

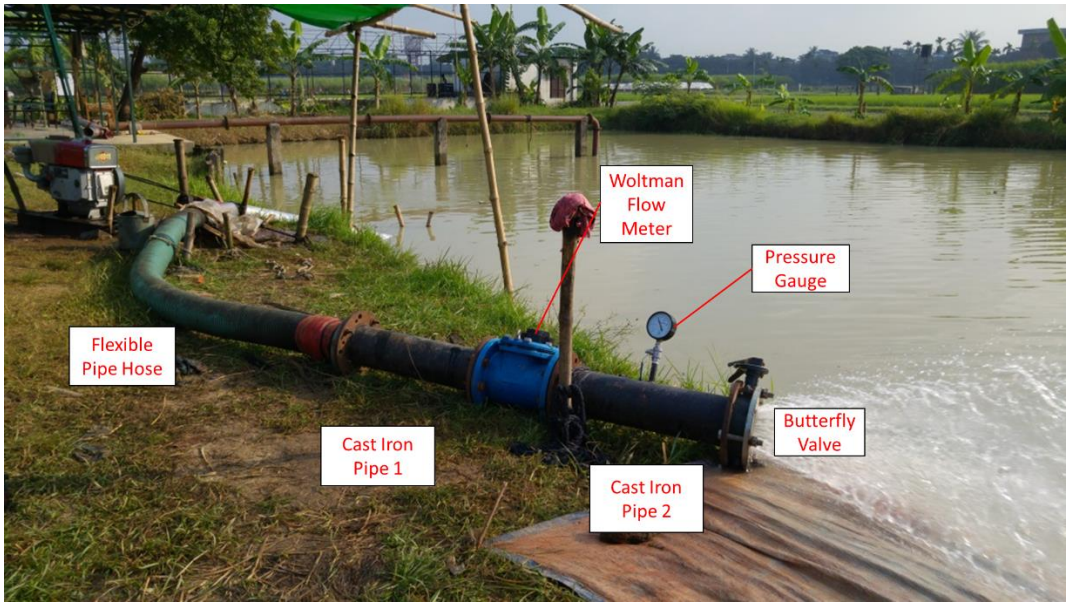

Figure 4.6. Control-Measurement Section

The control-measurement section, shown in Figure 4.6, includes a flexible hose, two segments of cast iron pipe, a Woltman flow meter, a pressure gauge, and a butterfly control valve. The outlet of the AFP section is connected to the flexible hose, and then to the flanged cast iron segment with a slip-to-flange adapter. The Woltman flow meter is located between the two cast iron segments, which are flanged, and measures the flow rate. The butterfly valve is placed at the end of the second cast iron segment to control the flow rate. A pressure gauge is also placed on the second cast iron segment to measure the pressure immediately before the outlet.

To test the performance of the impeller, each impeller is tested at three different RPMs (1000, 1500, and 1744) each for three replicate trials. Limited by the engine speed and the selection of pulley ratio, the pump may not operate exactly at the above speeds, but as close as possible. The testing procedure can be summarized in the following steps.

1. Connect the engine fuel lines.

2. Connect the power transfer coupling between the engine and the pump.
3. Place the intake of the pump into the water.
4. Connect the discharge of the pump with the intake of the testing platform (flexible hose).
5. Run the engine for a few minutes. Check/calibrate the test rig if necessary. Record the initial volume and fuel weight. Start the timer.
6. Start with the control valve at the fully open position. Continue running the test for 10 min. Record the open pressure reading during this process. Record the final volume and fuel weight after this process.
7. Move the control valve to the fully closed position. Record the closed pressure reading.
8. Open the valve again. Repeat steps 5-8 at different RPMs.
9. Stop the engine and reset. Repeat the test for the different impellers.

4.2 Rapid Prototype Testing

4.2.1 Reverse Engineering and Scaling Using Method of Rapid Prototyping

The prototype test uses the method of reverse engineering and rapid prototyping to produce six impeller prototypes with the following steps.

1. Measure the important design parameters of the impellers manufactured in Bangladesh, such as height, outer diameter, hub height, and hub diameter.
2. Reconstruct six CAD files based on the measurements.
3. Uniformly scale each impeller down to a fixed outer diameter of 3 inches and record its scaling ratio.

4. Insert a ¼-in hole at the center of the prototype in each of the CAD files for the shaft.
5. 3D-print these six prototypes.

4.2.2 Testing Prototypes in Laboratory

The prototype test rig is composed of a controller (Reliance Electric GV 3000/SE Sensorless Enhanced AC Drive), a manometer, a motor (Reliance Electric Duty Master A-C Motor Type P), a ¼-in shaft, a 3-inch prototype of the AFP impeller, a pipe system, a water tank, several buckets, a floor jack (Multiton MIC Corp. M-50 Hydraulic Pallet Truck), a wood frame, and several clamps. Figure 4.7 shows an overview of the test rig. Figure 4.8 gives a close view of the upper part of the rig. Figure 4.9 gives a close view of the lower part of the rig.

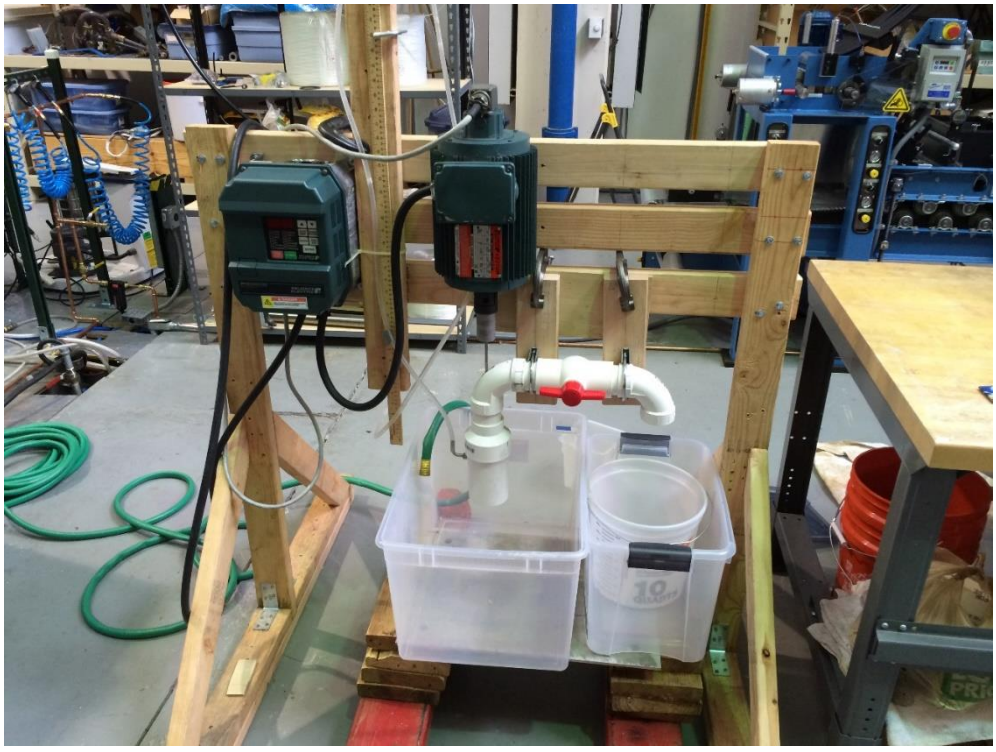

Figure 4.7: Prototype Test Rig

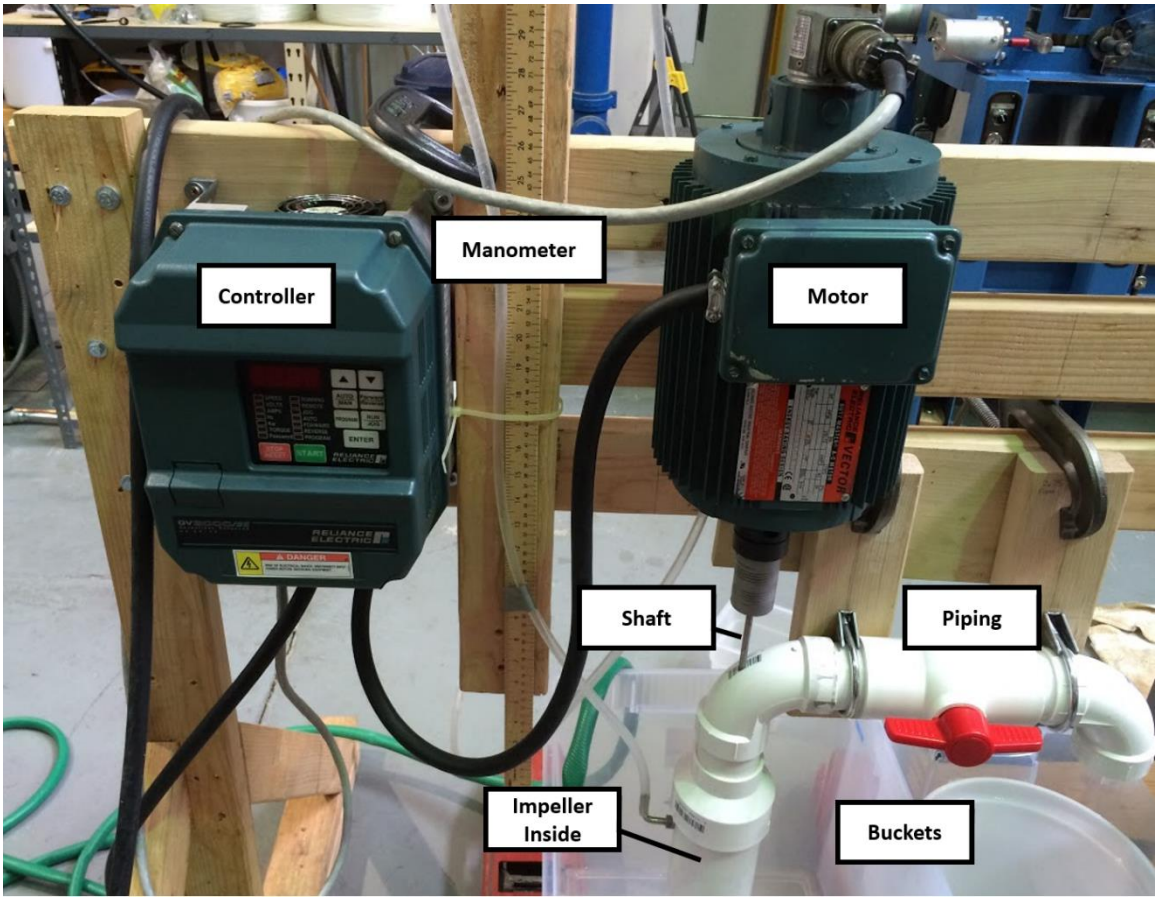

Figure 4.8: Upper Section of Prototype Test Rig

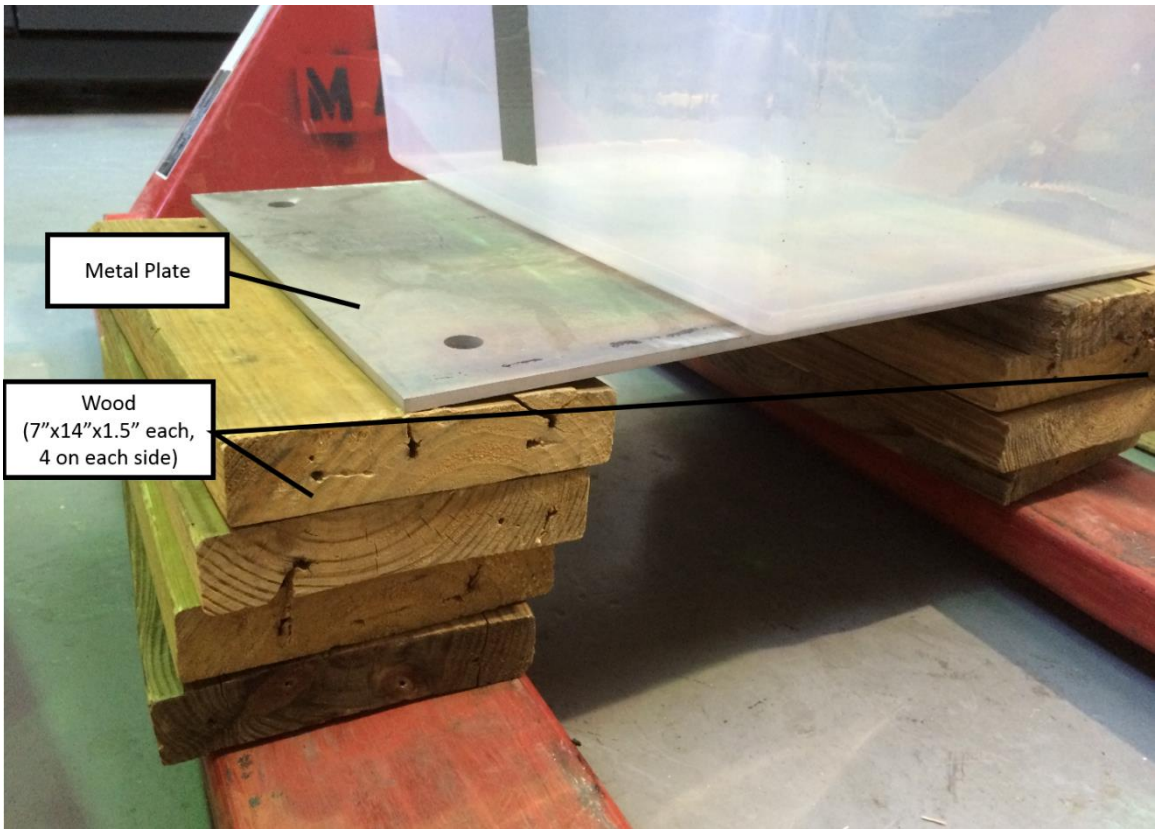

Figure 4.9: Lower Section of Prototype Test Rig

As shown in Figures 4.8 and 4.9, the prototype test rig is mounted on a wooden frame. The controller, manometer, motor, and pipe system are attached to the wooden frame by screws and clamps. The shaft that goes through the vertical components of the pipe is fixed onto the motor at one end and attached to the prototype impeller at the other end. The floor jack is bridged by a piece of metal plate and several scrap pieces of wood to support and elevate a large water tank and a 7.5-L bucket. Together with the floor jack, the tank and the bucket are placed below the pipe inlet and outlet, respectively.

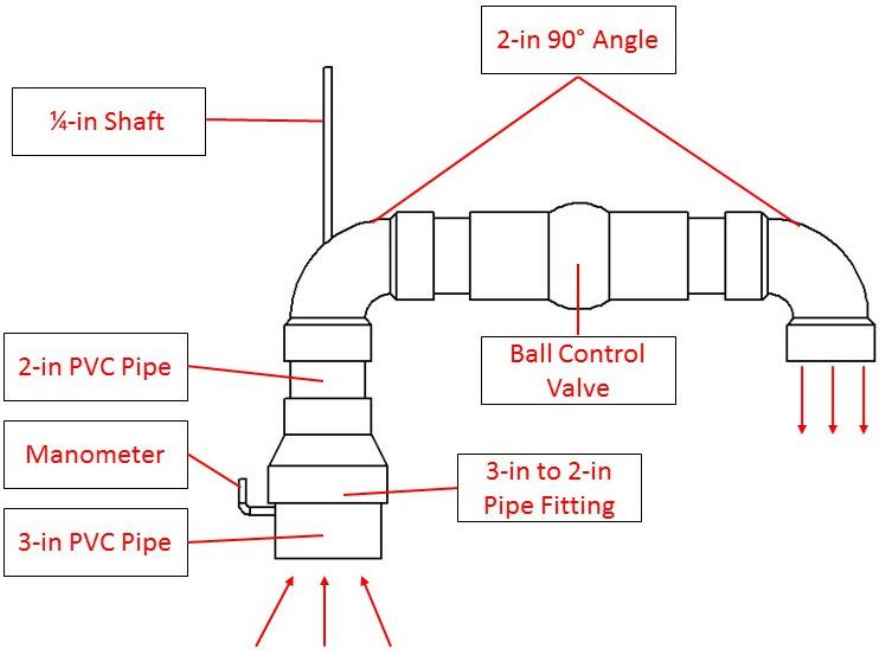

Figure 4.10. Schematic of the Piping System in Prototype Testing

The PVC piping system is designed to be similar in structure to the full-scale test rig, as shown in Figure 4.10. According to Figure 4.10, the 3-in prototype is placed at the inlet of a 3-in PVC pipe to lift water from the tank in a vertical direction. After that, a 3-in to 2-in reducer is attached. It is then connected to a 2-in 90° elbow, a 2-in ball valve, and another 2-in 90° elbow. Finally, the outflow is collected in a 7.5-L bucket. Prior to the testing, the piping system is carefully adjusted to ensure its inlet is vertical and aligned with the shaft. This guarantees the effective lift height and prevents rubbing between the prototype impeller and inner wall of the PVC pipe.

Note that the manometer used to measure pressure, shown in Figure 4.8, is hand-constructed from a long wood bar, a long plastic tube, and two meter-long rulers. One end of the plastic tube is attached to a hole in the PVC pipe just above the level of the prototype impeller. This allows for the measurement of the gage pressure increase

generated by the prototype impeller. Therefore, the ruler is carefully adjusted to a vertical position prior to the testing process.

The following testing procedure is performed for each impeller at 1000, 1500, and 1744 RPM.

1. Bridge the floor jack with wood and the metal plate. Place the water tank and the bucket on top of the bridge.
2. Move the floor jack underneath the frame. Align the tank and bucket to the piping system.
3. Fill the tank with water.
4. Plug in the controller, which also powers the motor.
5. Attach an impeller prototype onto one end of the shaft. Lock it in place with locknuts.
6. Mount the shaft onto the motor.
7. Raise the floor jack to its maximum height. Check that the impeller is completely submerged.
8. Align one end of the ruler to the water surface of the tank. Check that the ruler is vertical.
9. Input a desired RPM into controller, but do not start yet.
10. Set the ball valve to the closed position.
11. Initiate the controller to run the motor at the desired RPM.
12. Set the controller to measure the current RPM of the motor. Wait until the motor reaches a steady state condition.
13. Measure the manometer reading in closed position.

14. Fully open the ball valve. Immediately start timing.
15. Continuously refill the tank with water to maintain the water surface level.
16. Closely inspect the water level inside the bucket. As soon as it reaches 7.5 liters, stop timing.
17. Use a scoop to return the outflow back to the water tank to complete the flow circulation as shown in Figure 4.11. This provides time to take the measurements.

Figure 11. Scoop in Position

18. Record the elapsed time.
19. Record the average, maximum, minimum pressure readings from the manometer.

20. Record the power consumption from the controller.

21. Use the controller to turn off the motor.

22. Empty the bucket. Reset the water level in the tank.

23. Repeat steps 9-22 for different desired RPMs.

24. Dismount the shaft and the prototype impeller.

25. Repeat steps 5-24 for the rest of the prototype impellers.

Due to the large flow rate at 1744 RPM, the time elapsed to fill a 7.5-L bucket is too short to obtain an accurate result. Therefore, a 20-L container is used to collect the outflow and maintain the accuracy of the result.

4.3 Chapter Summary

This chapter describes the procedures for full-scale and prototype testing. Full-scale testing is performed in Bangladesh. Irrigation pumps are tested with different impellers, lift heights, and rotational speeds. As they are tested, flow rates and pressures are measured to evaluate their performance. Prototype testing is performed at Georgia Tech. First, 3D-printed impeller prototypes are produced using reverse engineering, and then are tested at different rotational speeds. The performance evaluation process is similar to full-scale testing. After this description of physical testing, the next chapter discusses the process of computer simulation performed in SolidWorks Flow Simulation and ANSYS CFX using CFD.

CHAPTER 5

COMPUTATIONAL FLUID DYNAMICS SIMULATION

This chapter describes the CFD simulations. A CFD simulation is typically divided into four stages. The first stage prepares the geometric model. This stage imports the CAD model of the impeller and places it in a pipe segment represented by a cylinder. The second stage generates a mesh for the computational domain. Then, the third stage determines the problem conditions, such as boundary conditions, rotational speeds, etc. Finally, the fourth stage defines the solver control. In the simulation process, the above four stages are applied to the setup of both SolidWorks Flow Simulation and ANSYS CFX. Prior to the results collection process, the CFD simulation is also subject to a grid independence study in order to validate its accuracy. After that, the CFD model is used to estimate the performance of each impeller, as well as to improve the impeller designs. The setups of CFD models for both software tools are discussed in this chapter, whereas the results are presented in Sections 6.3 and 6.4.

5.1 SolidWorks Flow Simulation Setup

5.1.1 Geometry Modelling

SolidWorks Flow Simulation is a CFD tool that enables one to perform fluid flow simulations on SolidWorks CAD models. The setup of CFD analysis with SolidWorks Flow Simulation begins with modeling the geometry. In the first stage, the program uses a SolidWorks part file to construct a geometric model of the impellers under study, as shown in Figure 5.1.

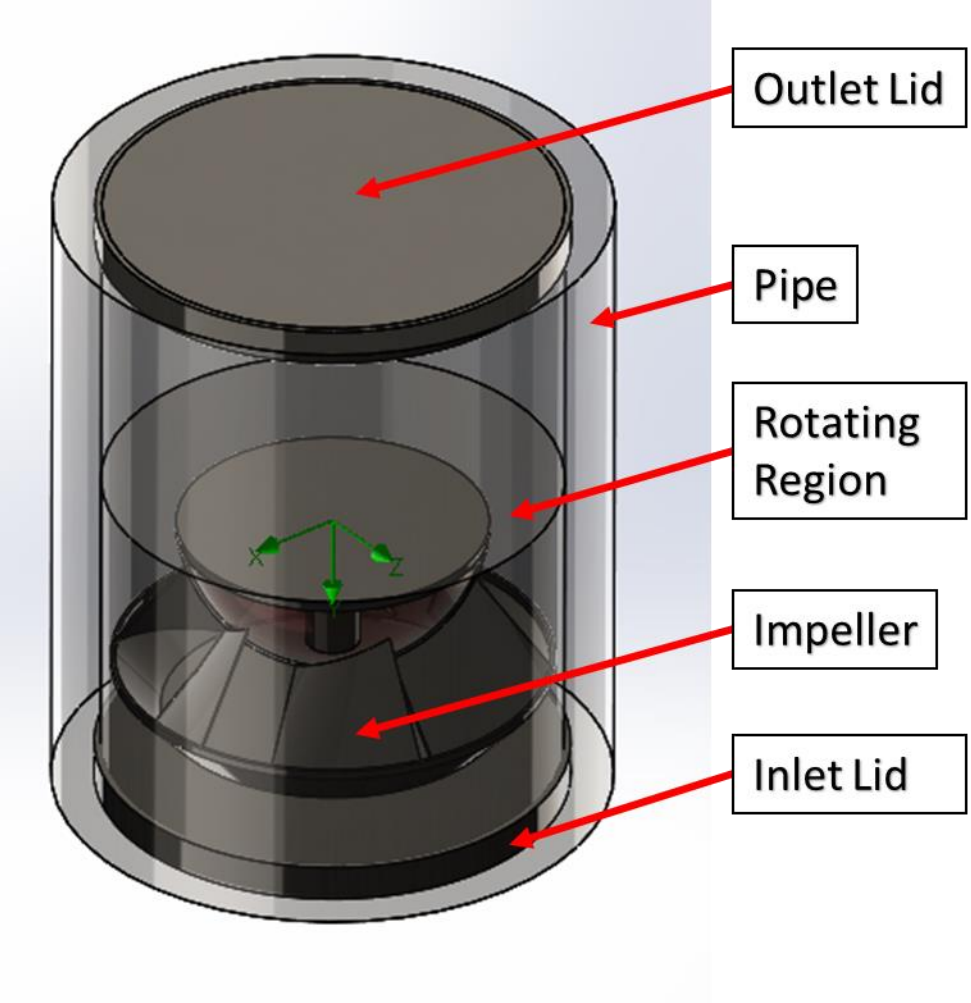

Figure 5.1. SolidWorks Flow Simulation Geometry Model

In Figure 5.1, a full-scale impeller is placed in a pipe segment, which is represented by a thin cylindrical shell with a diameter of 187 mm and a length of 270 mm. Due to the different outer diameters of the set of six full-scale impellers, a clearance of 3-4 mm is expected between the outer diameter of the impeller and the inner wall of the pipe. In this case, the pipe and the impeller are defined to be solid, while all other regions within the pipe are defined as water. As required by the software, two additional lids of small thickness are generated at the inlet and outlet to seal the fluid region. Finally, a rotating region, defined as the lower half of the fluid region, encloses the

impeller and is prescribed to rotate about the negative y-axis at a defined speed. When the system operates, the impeller is expected to move the water up in the figure, which is defined as the negative-y direction.

5.1.2 Mesh Generation

In the second stage, the system generates a mesh for the model by dividing the region of interest into small cells. Because of parameters that are only in the fluid region of interest, the mesh is generated for the fluid region inside the pipe but outside of the impeller. A three-dimensional view of a sample mesh profile for the tested impeller, which is Impeller 3 in Appendix A, is shown in Figure 5.2.

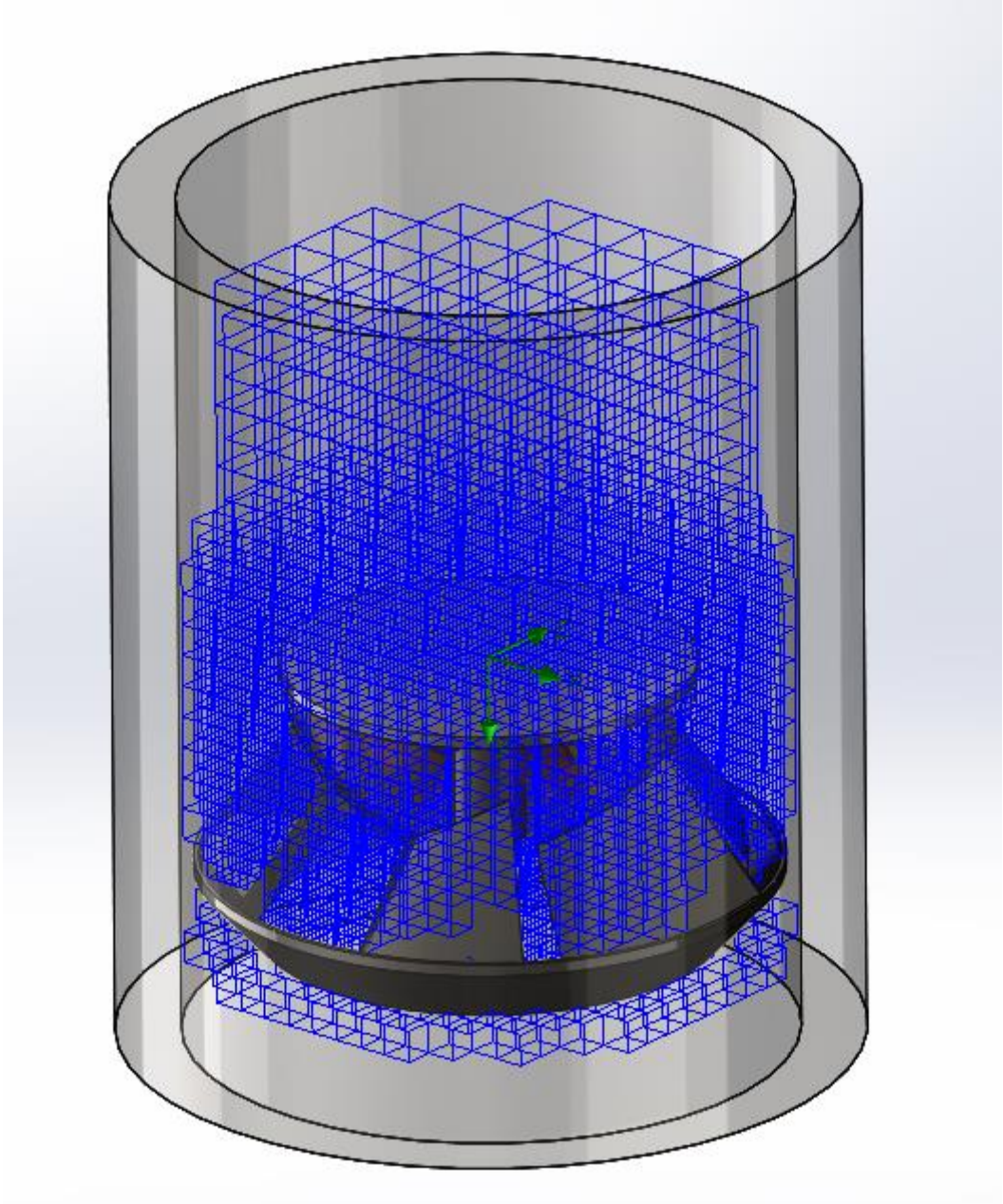

Figure 5.2. SolidWorks Flow Simulation Mesh Profile

In the case of Figure 5.2, SolidWorks Flow Simulation adopts cubic cells of different sizes to mesh the fluid regions. The mesh becomes more refined in the rotating region, where the geometry is more complex due to the impeller it contained. The mesh profile contains a total of 2,285 cells, with their volumes ranging between 8.8E-7 and

7.0E-6 m^3. In other cases, such as the grid independence study, the mesh may be further refined. After the mesh is initialized, the setup proceeds to the definition of the problem conditions.

5.1.3 Problem Conditions

In the third stage, the problem conditions are defined. This problem is generally described as an internal pipe flow. It assumes no cavitation during the operation. It also assumes pure liquid water as the only fluid in the problem. Based on a hydraulic diameter (pipe diameter) of 0.19 m and a reference flow velocity of 2 m/s, the Reynolds number is calculated as approximately 3.9E5. Because the Reynolds Number is much beyond 4,000, the problem simulates with a turbulent model. Specifically, the software solves this problem using a modified k-ε two-equation turbulence model. The model defines a low turbulent intensity of 2% and a turbulence length of 0.072 m, which is 3.8% of hydraulic diameter. The model also neglects any heat transfer in the system.

Several boundary conditions are defined to describe the operation. As commonly practiced, the fluid in the rotating region and the pipe segment is defined to rotate about negative y-axis at a constant speed, while keeping the impeller stationary. Because the rotational motion is a relative motion between water and impeller, this approach is adopted to reduce the number of moving objects. In order to measure the shut-off head, the outlet lid is defined as a wall with a smooth surface that rotates at the same angular velocity as the pipe wall. The inlet lid is defined as an opening with an environmental pressure of one atmosphere. All boundaries are assumed to be adiabatic.

Some initial conditions are defined as well. Fluid in all regions is defined initially at a pressure of one atmosphere and room temperature. Fluid outside the rotating region is defined with an initial velocity of zero, whereas the fluid inside the rotating region is defined previously.

With the above conditions determined, the problem is solved by an automatic SolidWorks Flow Simulation solver for a steady-state solution.

5.2 ANSYS CFX Setup

5.2.1 Geometry Modeling

The simulation is also performed with ANSYS CFX. ANSYS CFX is a high-performance CFD software that is recognized for its accuracy, robustness, and speed when simulating rotating machinery such as pumps. Similar to the procedure described in the previous section, the simulation with ANSYS CFX begins with modeling the geometry.

In the first stage of CFX simulation, the geometry of the impeller in the format of STEP is generated from the SolidWorks part file and imported to the CFX Design Modeler. A cylindrical enclosure is created to serve as a pipe segment, as shown in Figure 5.3. The enclosure has a diameter of 187 mm with an inlet and an outlet placed 0.2 m and 0.1 m away from the impeller, respectively. In this model, the imported impeller is a solid object, whereas the other volume within the enclosure is liquid water. When the pump operates, the impeller rotates clockwise to lift the water up. Because only the flow profile of the liquid water is to be studied, the solid model of the impeller is suppressed.

Therefore, the model contains only water and has the shape of a cylinder with the impeller at its center removed.

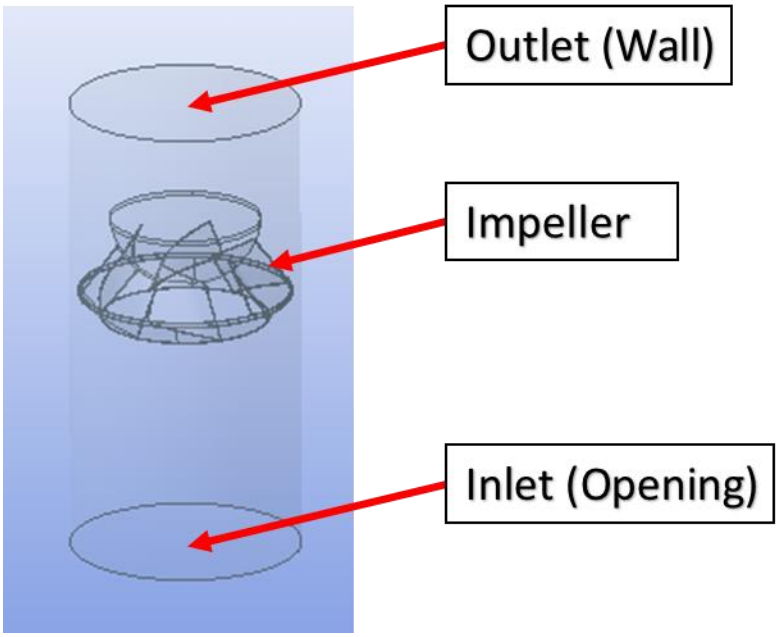

Figure 5.3. CFX Geometry Model

5.2.2 Mesh Generation

The second stage of CFX simulation generates the mesh profiles based on the geometric model discussed in the previous section. This stage uses the built-in CFX tool for meshing. In this thesis, most of the setup of the default CFX solver was adopted. The software defines the inlet and the outlet as two named selections, then solves the mesh at a fine relevance center. The fine relevance center is chosen because a mesh fails to be generated at coarse or medium levels. The mesh sample generated using the impeller No. 3 with the above settings is shown in Figure 5.4.

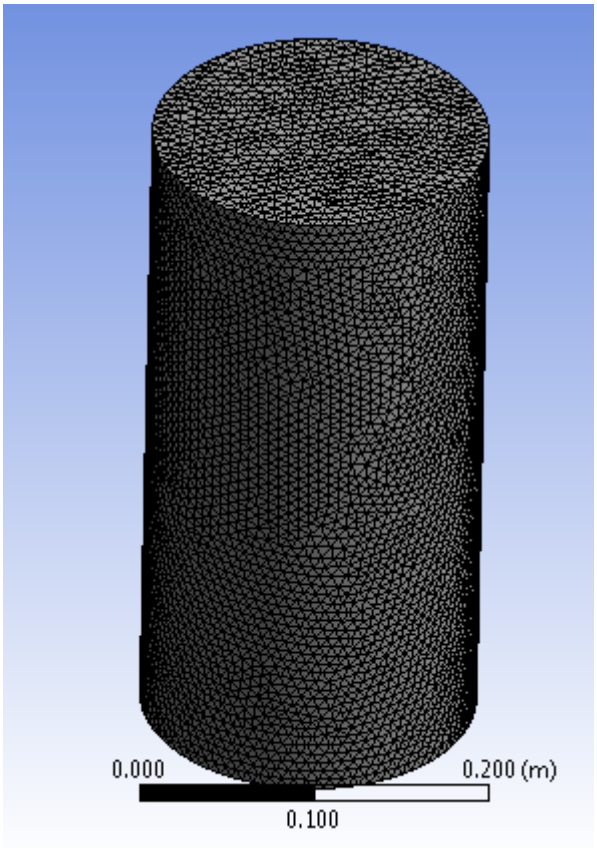

Figure 5.4. CFX Sample Mesh Profile

In Figure 5.4, the mesh profile is generated using an unstructured tetrahedral grid. It contains a total of 49,899 nodes and 265,735 elements. The mesh profile has a minimum edge length of 1.64E-4 m, a maximum face size of 6.92E-3 m, and a maximum size of 1.38E-2 m. Note that this mesh profile is further refined by reducing the value of its maximum sizes, thus increasing the number of nodes and grids in order to perform the grid-independence study.

5.2.3 Problem Conditions

In the third stage, the setup is specified by problem conditions. Similar to the previous approach in SolidWorks Flow Simulation, this problem assumes no cavitation.

It adopts the turbulent model based on the calculated Reynolds Number of 3.9E5. It also neglects heat transfer.

In determining the boundary conditions, the same concept discussed in Section 5.1.3 that keeps the impeller stationary by simulating the fluid region to rotate at an opposite direction is introduced. Under this concept, four boundaries are identified: "outer wall," "inner wall," "inlet," and "outlet." The "outer wall" and "inner wall" are the boundaries between water and pipe, and between water and impeller, respectively. The "inlet" and "outlet" are the circular surfaces at the bottom and top. Note that although the name "outlet" is given for its position after the impeller, it is in fact simulated as a wall in order to measure the shut-off head. In this case, all three walls mentioned above are defined as no slip, smooth walls that rotates at the same angular velocity as the fluid region. The "inlet," nevertheless, is defined as a rotating opening with a static gage pressure of zero atmospheres. The "inlet" assumes a subsonic operating condition and adopts a turbulence model with a default turbulence intensity and an auto-computed length scale.

With the above boundary conditions, the problem then initializes the computational domain with the user-defined angular velocity and solves for the steady-state solution with a k-epsilon turbulence model and a scalable wall function.

5.2.4 Solver Controls

In this last stage, the computation process is specified by the solver control settings. This problem adopts a high resolution advection scheme and a first order turbulence numeric. The solver then determines an automatic timescale that leads to the

convergence of continuity and momentum in x, y, and z directions, where convergence is defined by an RMS residual of 1E-4.

5.3 Chapter Summary

This chapter discusses the procedures for CFD simulations. Simulation is accomplished using both SolidWorks Flow Simulation and ANSYS CFX. Each simulation includes geometry modeling, mesh generation, problem definition, and solver control before the software solves for a solution. Each simulation assumes a turbulent model without heat transfer or cavitation. Note that in SolidWorks Flow Simulation, solver control is not included because it sets itself automatically. Chapter 6 describes the results and analysis of the testing.

CHAPTER 6

RESULTS AND DISCUSSION

This chapter presents the results obtained from full-scale and prototype impeller experiments, as well as the simulations performed using SolidWorks and ANSYS CFX. The testing process described in the previous two chapters is outlined in Figure 6.1.

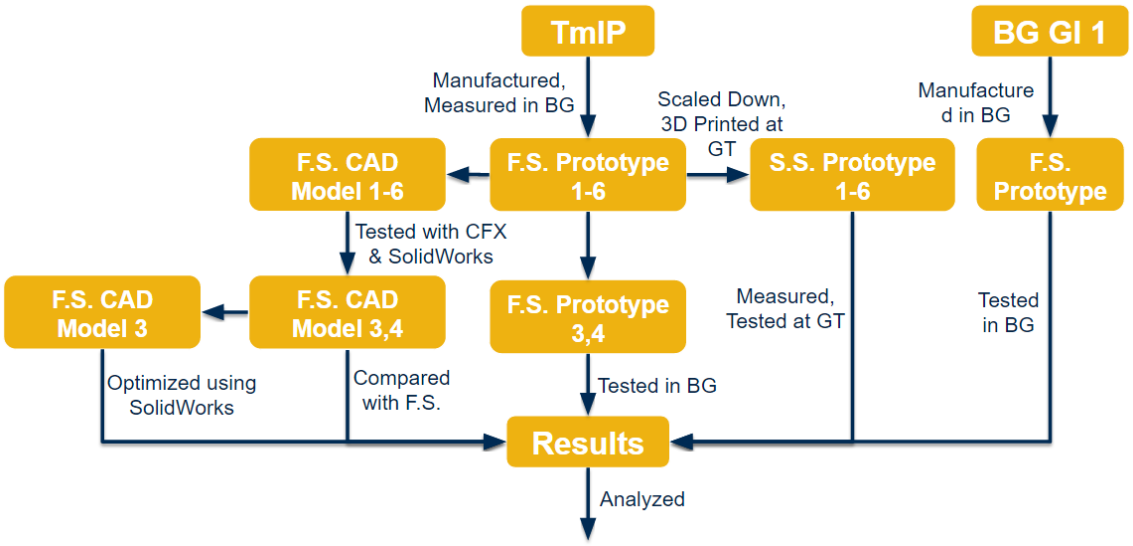

Figure 6.1. Impeller Testing Flow Chart

The results of each test are discussed in turn. In Section 6.1, the chapter begins by analyzing the results of full-scale experiments performed in Bangladesh using major and minor losses and the Affinity Law at different rotational speeds. The analysis is then used to estimate the field performance without the testing rigs. The testing procedure and corresponding analysis described in Section 6.1 can be used as methods for pump selection. Next, the chapter validates the full-scale experimental results with prototype testing and software simulation. Section 6.2 discusses the results obtained from

prototype-scale experiments. These results are compared with the full-scale results qualitatively and quantitatively. They are also used to identify the manufacturing capabilities of the Bangladeshi factory, as well as the corresponding effects on pump performance. Once the experimental results are discussed, Sections 6.3 and 6.4 review the full-scale simulations obtained using SolidWorks and CFX, respectively. Each test and its associated format are listed in Table 6.1. After the full-scale results are validated, this chapter investigates the potential for design optimization in Section 6.5 using rapid prototyping and numerical simulations, which are aimed at further savings of energy and operating costs.

Table 6.1. Tests and Corresponding Test Formats

	Tests for				
Test format	Geometric Differences due to Manufacturing	Friction Losses	Different RPMs	Different Lift Heights	Method of Pump Selection
Full-Scale		√	√	√	√
Prototype	√	√	√		
SolidWorks Simulation	√		√		
CFX Simulation	√		√		

6.1 Full-Scale Results

The full-scale results are generated by two sets of testing. The first set tested Thai mixed-flow impellers using the full-scale testing procedure described in Section 4.1. Among the six impellers manufactured, only two (numbers 3 and 4) were tested due to a limited budget. The first set was tested at pump rotational speeds of approximately 1000, 1500, and 1744 RPM to match the prototype tests. The first set was also tested at fully closed and fully open valve positions to obtain the shut-off pressure head and the maximum volumetric flow rate. The second set tested another sample (GI 1) of the same model using the same procedure in Section 4.1. Different from the first, the second set operated at pump rotational speeds of approximately 1500, 1750, and 2000 RPM, and at valve positions of 90%, 50%, 40%, 30%, 20%, and 0% open. The geometry of manufactured impellers is presented in Section 6.1.1, and the pump performances are discussed in other Sections of 6.1.

Note that in this section, a total of seven impellers of the same model are tested at full scale. These impellers and the tests they are associated with are listed below in Table 6.2.

Table 6.2. Full-Scale Testing

	Tests for				
Impellers	6.1.1: Geometric Differences due to Manufacturing	6.1.2: Friction Losses	6.1.3: Different RPMs	6.1.4: Different Lift Heights	6.1.5: Method of Pump Selection
No. 1	√				

No. 2	√				
No. 3	√	√	√		
No. 4	√	√	√		
No. 5	√				
No. 6	√				
BG GI 1		√	√	√	√

6.1.1 Geometry of Sample Bangladesh Impellers

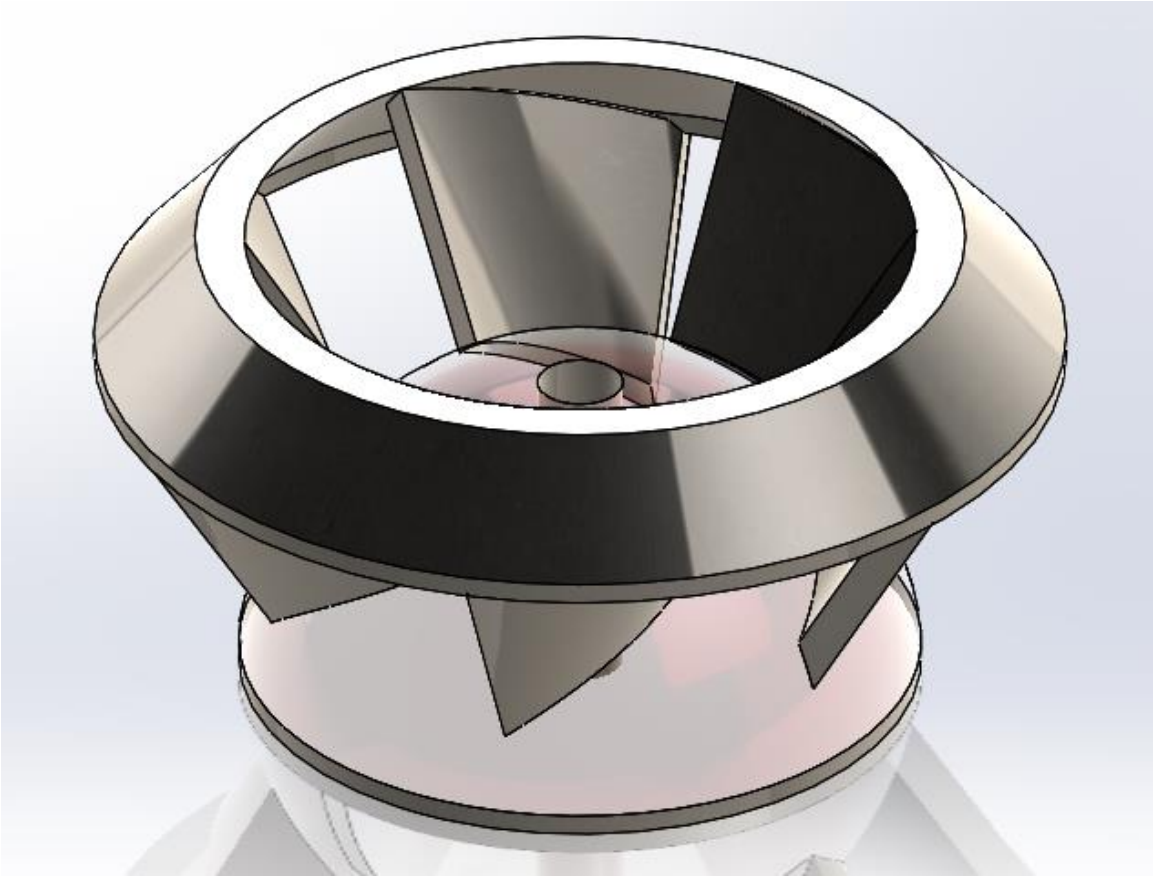

Figure 6.2. SolidWorks Outline of a Sample Impeller

A sample Bangladesh impeller is shown in Figure 6.2. In this section, a set of six sample impellers were manufactured by a Bangladeshi factory and measured to identify its manufacturing capability. The measurements are given in Appendix A. In brief summary, the six impellers have an average impeller height of 88.03 mm, cone height of 56.92 mm, outer diameter of 180.49 mm, and cone diameter of 126.71 mm. The standard deviations of the above parameters are 1.86 mm, 1.70 mm, 1.18 mm, and 0.90 mm, respectively. The locations of these measurements in mm are shown in Figure 6.3. The measurements of all parameters are listed in Appendix A and summarized in Table 6.3. Based on these measurements, the average standard deviation for all geometric parameters is calculated to be 3.36%.

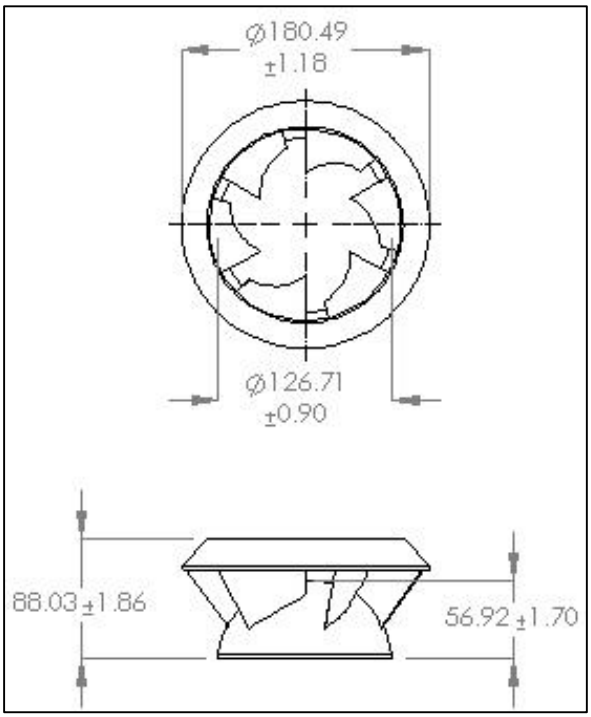

Figure 6.3. Average and Standard Deviation of Sample Impellers

Table 6.3. Summary of Design Parameter Measurements

Impeller	Measurements								
	Vane Width (mm)	Cone Height (mm)	Impeller Height (mm)	Distance Between Top of Vanes (mm)	Distance Between Edges of Vanes (mm)	Hole Diameter (mm)	Cone Diameter (mm)	Outer Diameter (mm)	Weight (kg)
1	57.99	59.63	91.37	59.97	133.90	30.80	126.97	180.97	1.14
2	56.49	55.13	85.87	60.57	129.38	37.68	127.13	179.77	1.10
3	57.15	58.17	87.50	52.78	132.47	32.45	126.60	178.90	1.14
4	56.14	55.03	87.77	61.54	133.53	32.37	125.15	180.85	1.16
5	56.96	57.03	57.13	64.92	128.35	36.18	127.73	181.58	1.10
6	56.61	56.50	88.57	61.89	126.70	38.01	126.65	180.87	1.12

Note that although all six vanes may exhibit different geometries for a given impeller sample, they are modeled as identical in SolidWorks. This approximation is made because the differences are not significant based on the measurements in Table 6.3. In the case of sample No. 3, which is used for design optimization in Section 6.5, each of the six vanes is defined to follow a path line that revolves 45° about the shaft with an elevation of 30 mm and a vane angle (taper) of 43°.

6.1.2 Tests Corresponding to Friction Losses

In this section, the concept of major and minor losses is introduced to estimate the pump performance with different components, or in other words, with different losses. In this case, the loss coefficients of the AFP and the testing rigs are calculated. Then, the actual pump performance can be calculated from the test performance by subtracting the loss coefficient due to the control measurement segment.

To begin this loss analysis, the loss coefficients of each component within the system are estimated from its material and geometry. Sources of the major loss are summarized in Table 6.4, and those of the minor loss are summarized in Table 6.5. These sources of loss are also labeled in the CAD model of the AFP and the photos of the testing apparatus shown in Figures 6.4 to 6.5. The modeling and calculation of the following losses are further discussed in Appendix B. From those results, the sum of the major loss coefficient is 3.94, and the sum of the minor loss coefficient is 13.24. This results in a total loss coefficient of 17.18. In this case, the minor loss ironically plays a dominant role in the friction loss analysis.

Table 6.4. Major Losses

No.	Pipe Material	Major Loss Coefficient K=fL/D
1	GI Pipe with Inner Shaft	1.22
2	Flexible Pipe	2.43
3	Worn Cast Iron	0.29
	Total Major Loss	3.94

Table 6.5. Minor Losses

No.	Feature	Minor Loss Coefficient K	No.	Feature	Minor Loss Coefficient K
1	Inlet Cage	2.62	9	Pressure Fitting 2	1.00
2	Diffuse Vane	1.08	10	Woltman Flowmeter WPH-150	1.43
3	Protruding Pipe Entrance	0.80	11	Tee Threaded Dividing Line Flow	0.90
4	Gradual Contraction	0.26	12	Ball Valve	0.05

5	Shaft Bearing	1.08	13	Pressure Gauge	0.27
6	Wye Flow	0.32	14	Butterfly Valve	1.62
7	Crossing Shaft	0.005	15	Sharp Edged Exit	1.00
8	Pressure Fitting 1	0.80		Total Minor Loss	13.24
				Sum of Minor and Major Losses	**17.18**

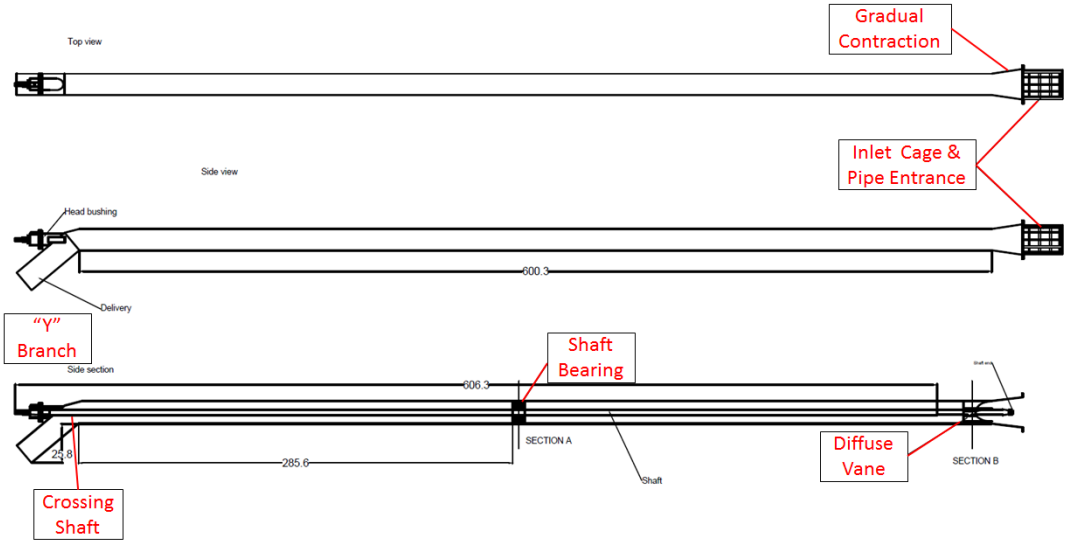

Figure 6.4. AFP Section Component Identification for Friction Losses 1

Figure 6.5. AFP Section Component Identification for Friction Losses 2

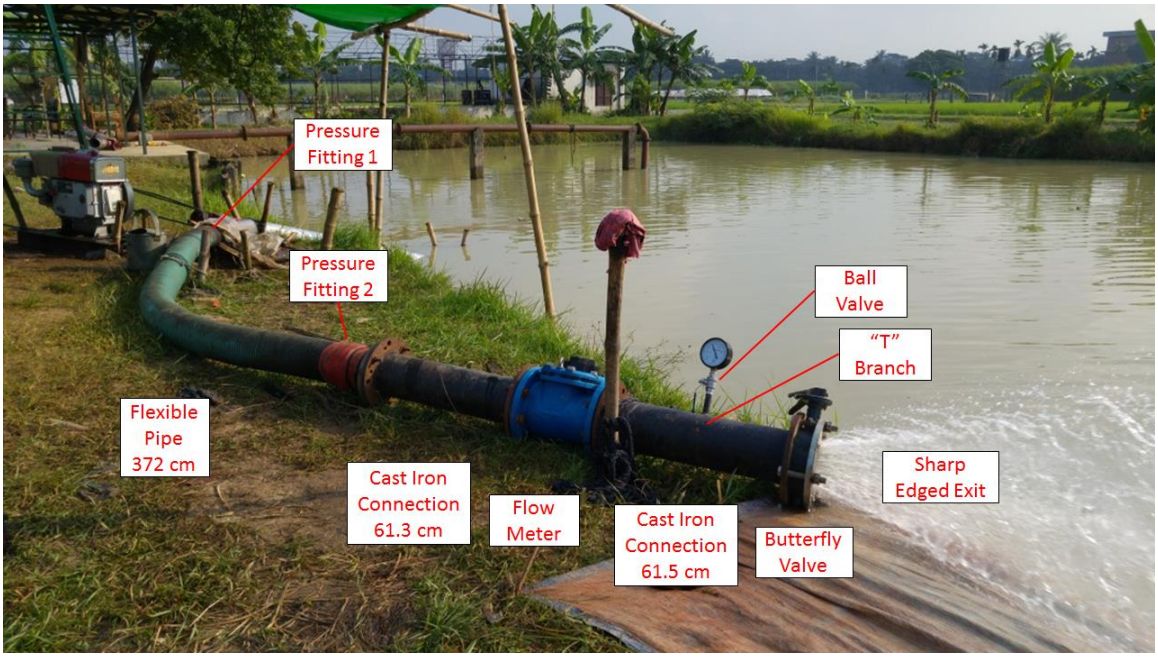

Figure 6.6. Control-Measurement Section Component Identification for Friction Losses

The calculated loss coefficient is validated by the results of two sets of testing. By running the AFP using the same apparatus and different RPMs, the shut-off head and maximum velocity are obtained to calculate the loss coefficient. This is done using Equation 6.1, which may be derived from the modified Bernoulli's Equation shown in Equation 3.5.

$$K = \frac{H^2 g}{V^2} - 1 \qquad \textit{Equation 6.1}$$

where K is the loss factor, H is the shut-off head, g is the gravitational constant, and V is the average velocity at fully-open valve position. From the results listed in Table 6.6, the sum of the major and minor loss coefficient has an average of 21.75 and a sample standard deviation of 1.74 (8%). Experimental data and calculations are included in Appendix B and are highlighted in Table 6.6.

Table 6.6. Summary of Experimental Loss Coefficient Values

		RPM	Loss Coefficient	Average		STD	
Impellers 3 and 4	3	1006	24.94	22.67	21.75	1.77	1.74
		1498	21.58				
		1748	21.88				
	4	1004	24.94				
		1510	21.34				
		1741	21.35				
BG GI 1 Model	Replication 1	1740	20.62	20.84		1.22	
		1498	23.23				
		2065	20.06				
	Replication 2	1757	20.38				
		2059	19.88				
		1553	20.86				

The estimated loss coefficient (17.18) is smaller than that calculated for the experiments (21.75) by 4.57, or 21%. This falls into a 99% confidence interval. A main reason for this difference is the relatively higher loss coefficient at low RPMs. As shown in Figure 6.6, the calculated loss coefficient at around 1000 RPM exhibits much higher values than the average and becomes an outlier that raises the average loss coefficient. This may be due to the unstable flow at low RPMs. Another reason may be incomplete and imperfect estimation. In this estimate, the loss coefficient of each component is calculated based upon a reference (Crane Co. Engineering Division, 2012). In practice, a data from references are not exactly the same as the actual object and may result in this difference. For example, the minor loss that results from the bending angle of the flexible pipe is not included in the model because the amount of bending may vary in each trial. Though insignificant, this factor can contribute up to 0.24 (calculated from a 90° elbow) to the minor loss coefficient (Crane Co. Engineering Division, 2012). A third reason is the assumption of pure water. The water source was assumed to contain only water, but it may carry many other objects, such as pebbles, sands, and small fish. When water is sucked up by the pump, it is to imagine that some pebbles may stick to and block the inlet cage. This will reduce the total area of holes at the inlet cage, and thus reduce the flow velocity and underestimate the total loss coefficient. Also, it can change the density of the fluid, which would have an effect on the calculations. In summary, a combination of the above factors may result in the difference between loss coefficient estimation and experimental calculation.

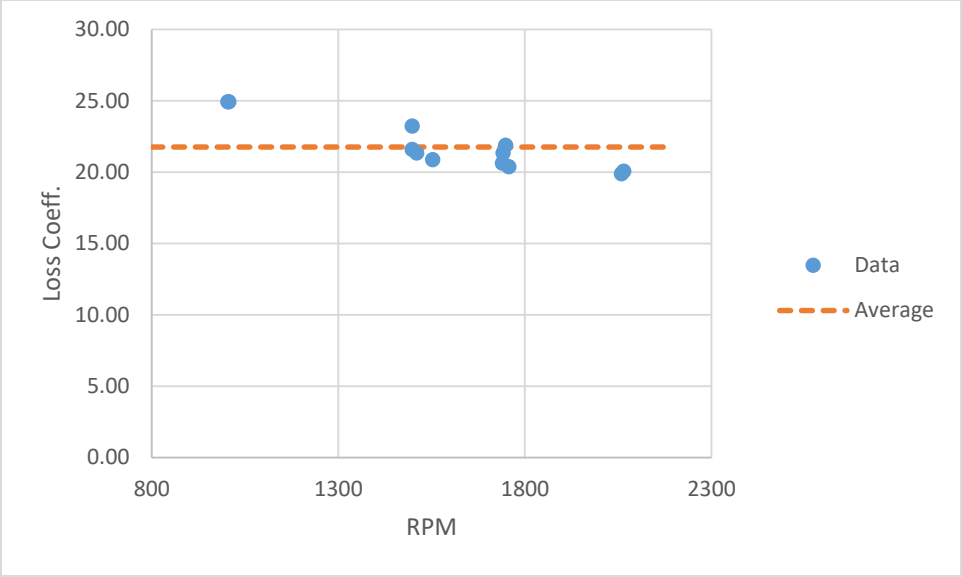

Figure 6.7. Calculated Experimental Loss Coefficient

This approach of loss analysis with major and minor losses can be further improved by inserting an additional pressure gauge at the entrance of the control-measurement segment. In this manner, the loss coefficient of each segment can be calculated directly from the measurements, which saves effort and eliminates the inaccuracy from estimation. From Equation 6.1, one may derive a new equation to obtain the loss coefficient at both segments as shown by Equations 6.2 and 6.3,

$$K_{CM} = \frac{H_{CM}^2 g}{V^2} - 1 \qquad \textit{Equation 6.2}$$

$$K_p = K - K_{CM} \qquad \textit{Equation 6.3}$$

where K_{CM} is the loss factor of the control-measurement section, K_p is the loss factor of the pump section, $H_{CM} = \frac{p_{CM} - p_{atm}}{\rho g}$ is the head measurement at the new pressure gauge, and p_{CM} is the absolute pressure reading at the new pressure gauge.

Proceeding with this approach, the performance of an irrigation system with customized components can be estimated. For instance, a customer may wish to install the system without the control-measurement segment. Then, at the same RPM and lift height, the maximum discharge of this pump is estimated using Equation 6.4,

$$Q_{est} = Q_{test} * \sqrt{\frac{K+1}{K_p+1}} \qquad \textit{Equation 6.4}$$

where Q_{est} is the estimated discharge without the control-measurement segment and Q_{test} is the measured discharge during the test. If the customer also wishes to modify the piping system, such as adding angles or valves, the above equation may be modified as Equation 6.5 to estimate the maximum discharge of the newly customized system.

$$Q_{mod} = Q_{test} * \sqrt{\frac{K+1}{K_{mod}+1}} \qquad \textit{Equation 6.5}$$

where Q_{mod}, K_{mod} are the discharge and loss factor of the system after modification.

In conclusion, the approach of loss analysis enables the performance prediction of pump at systems with customized components. The following two sections discuss the pump performance at different RPMs and lift heights.

6.1.3 Tests Corresponding to Different RPMs

The Affinity Law can estimate the pump performance at different RPMs. As shown in Equations 3.18 and 3.19 in Section 3.3, the discharge rate is expected to be directly proportional to the pump speed. Therefore, a first order trend line fit through the origin is applied to the two sets of results to study the relationship between maximum

discharge rate and pump speed. The results for Impellers 3 and 4 and GI 1 Model are contained in Appendix C and highlighted in Figures 6.8 and 6.9.

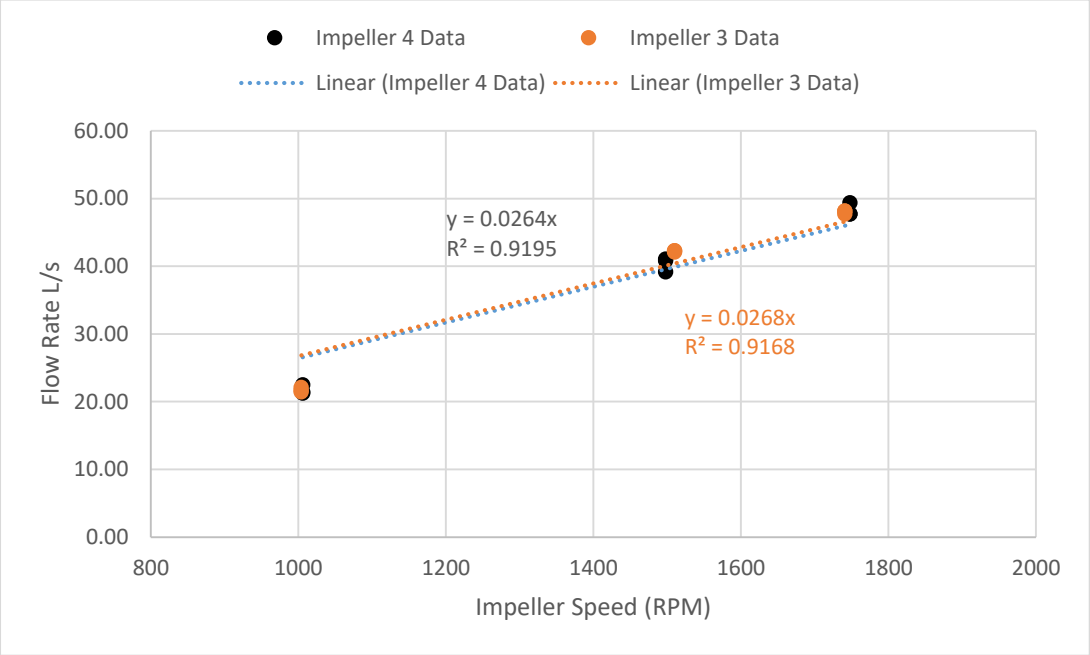

Figure 6.8. Maximum Flow Rate vs. Pump Speed of Impellers 3 and 4

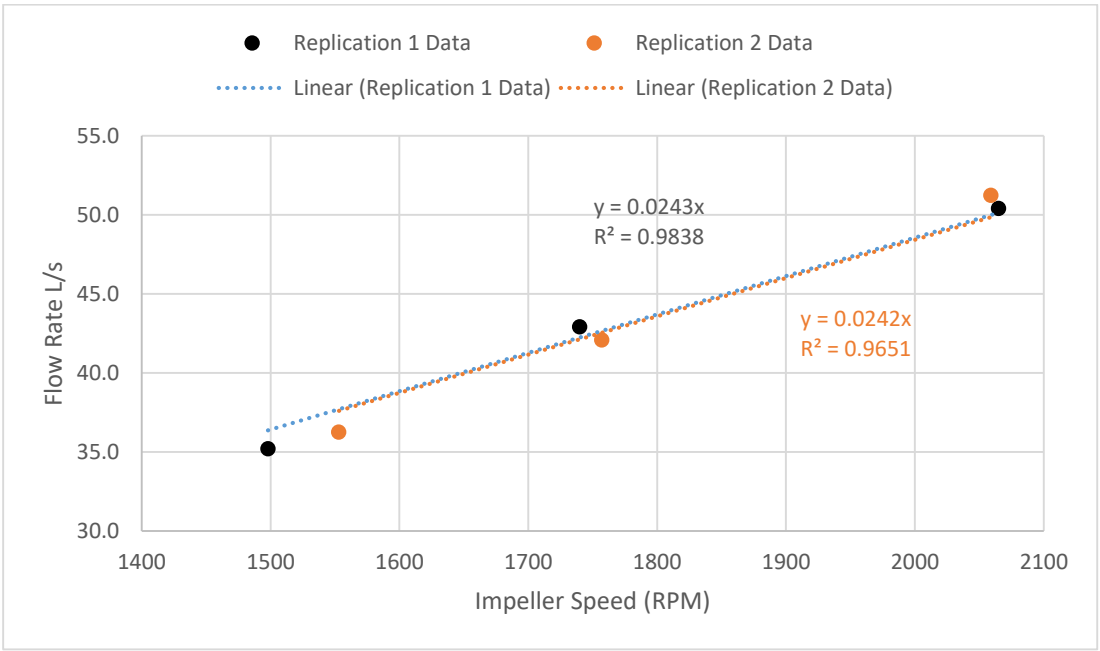

Figure 6.9. Maximum Flow Rate vs. Pump Speed of GI 1 Model

In both Figures 6.8 and 6.9, the experimental data demonstrate good agreement with the Affinity Law, as shown by R-squared values above 0.9. The results also show high consistency within each set. In both cases, the slopes of the linear-fit line have differences of 1.54% and 0.41% between replications. These results indicate that the Affinity Law is a reliable method to correlate pump performance and pump speed. Pump performance at a customized RPM may be estimated using the Affinity Law shown in Equations 3.18 and 3.19 of Section 3.3 when its performance at other RPMs is known.

6.1.4 Tests Corresponding to Different Lift Heights

The pump performance at different lift heights can be simulated by different valve positions. When the pump's performance at a new lift height is to be studied, a direct approach is to elevate the outlet to the specific height. This approach, nevertheless, requires a flexible pipe attached to the end, a supporting frame, as well as heavy lifting capability. A new approach using control valves is introduced to save cost and effort in the testing procedure. Using this new approach, the performance of a pump tested at a customized lift height within the operation range can be estimated. This section discusses the development and application of this approach.

This approach is developed from the Bernoulli's Equations for turbomachinery. Recall Equation 3.5 in Section 3.2,

$$\left(\frac{V^2}{2g} + z + \frac{p}{\rho g}\right)_1 - \left(\frac{V^2}{2g} + z + \frac{p}{\rho g}\right)_2 = h_L - \frac{w_p}{g} \qquad \textit{Equation 3.5}$$

where H is the original lift height. If position "1" is defined as the level of the water source (pond, river, etc.), and position "2" is defined as the level of the outlet of the pump system, then the reservoir assumption may be made. Thus, Equation 6.6 is generated,

$$z_2 - z_1 = H;\ p_1 = p_2 = p_{atm} \qquad \textit{Equation 6.6}$$

Assuming the water source has a large surface area, thus V_1 is negligible. Then the Equation 6.6 may be simplified to Equation 6.7,

$$\frac{V_2^2}{2g} + H + h_L = \frac{w_p}{g} \qquad \textit{Equation 6.7}$$

or as

$$(K+1)\frac{V_2^2}{2g} + H = \frac{w_p}{g} \qquad \textit{Equation 6.8}$$

where $h_L = K\frac{V_2^2}{2g}$ and K is the sum of major and minor loss coefficients.

Suppose a new lift height, H^*, is to be studied, with a corresponding flow velocity, V_2^*. Assume a pump performs consistently and generates a constant w_p. Then, Equation 6.9 can be written in terms of H^* and V_2^*,

$$(K+1)\frac{V_2^{*2}}{2g} + H^* = \frac{w_p}{g} \qquad \textit{Equation 6.9}$$

As the control valve allows one to control the water flow rate, one expects the same V_2^* within the operation range to be reached at a lift height of H at some valve position. Thus, Equation 6.9 may be rewritten as Equation 6.10,

$$(\Delta K + K + 1)\frac{V_2^{*2}}{2g} + H = \frac{w_p}{g} \qquad \textit{Equation 6.10}$$

where ΔK is the change of minor loss coefficient of the control valve from its nominal position. Combining Equations 6.9 and 6.10 results in Equation 6.11,

$$H^* - H = \Delta K \frac{V_2^{*2}}{2g} \qquad \textit{Equation 6.11}$$

If position "3" is defined as the position of pressure gauge, which is located immediately before the butterfly control valve, Equation 6.12 can be generated when Bernoulli's Equation is applied to positions 2 and 3,

$$\left(\frac{V^2}{2g} + z + \frac{p}{\rho g}\right)_3 - \left(\frac{V^2}{2g} + z + \frac{p}{\rho g}\right)_2 = h_{L\ valve} \qquad \textit{Equation 6.12}$$

where $V_2 = V_3 = V$ from continuity, $z_3 = z_2$, and $h_{L\ valve} = \Delta K \frac{V^2}{2g}$. Equation 6.12 can be simplified to Equation 6.13,

$$\Delta K \frac{V^2}{2g} = \frac{P}{\rho g} \qquad \textit{Equation 6.13}$$

where P is the gage pressure reading from the pressure gauge. Inserting Equation 6.13 into Equation 6.11, the new lift height H^* may finally be expressed as Equation 6.14,

$$H^* = \frac{P^*}{\rho g} + H \qquad \textit{Equation 6.14}$$

where P^* is the gage pressure reading at $V = V^*$.

Using this equation, which correlates the theoretical lift height and pressure reading at each valve position, the pump is tested at different valve positions and RPMs by measuring the pressure and flow rates. The results of this test are contained in Appendix D and highlighted in Figure 6.10.

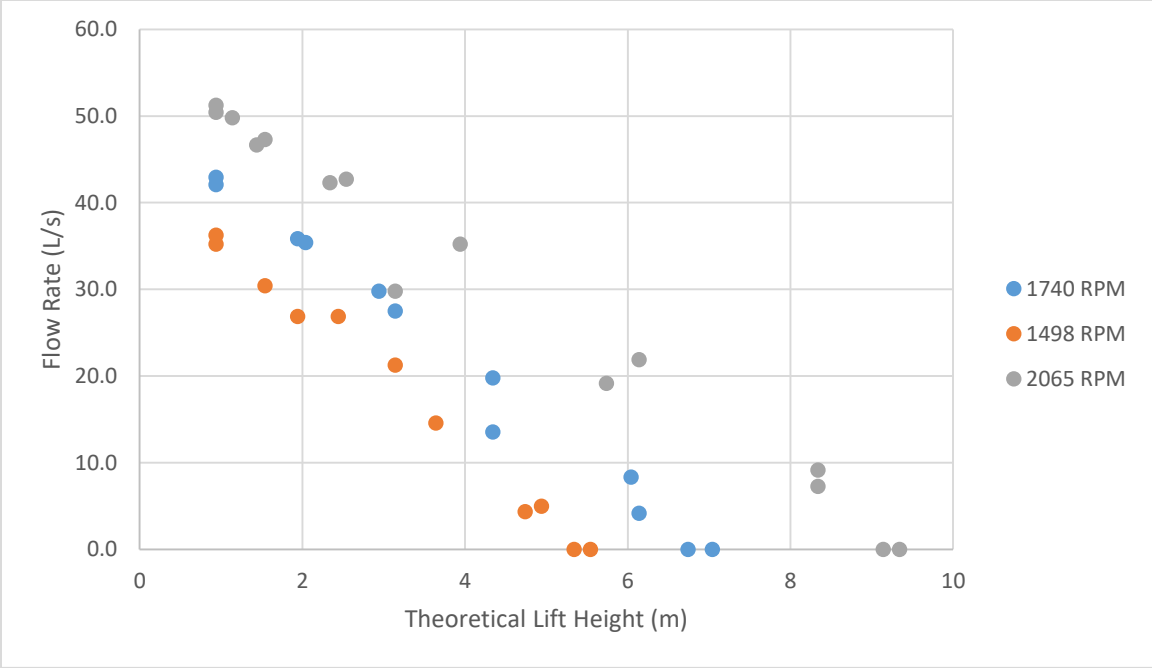

Figure 6.10. Flow Rate vs. Theoretical Lift Height

Figure 6.10 plots the measured flow rate versus expected lift heights. Based on this figure, the flow rate decreases with an increase in the theoretical lift height at all tested RPMs. In fact, because the flow rate is directly proportional to the flow velocity at a constant pipe diameter, the relationship between flow rate and theoretical lift height can be represented by Equations 6.15 and 6.15,

$$(K+1)\frac{V_2^{*2}}{2g} + H^* = \frac{w_p}{g} \qquad \textit{Equation 6.15}$$

and

$$H^* = \frac{w_p}{g} - (K+1)\frac{V_2^{*2}}{2g} \qquad \textit{Equation 6.16}$$

Assuming the pump operates consistently and generates a constant w_p, then a linear relationship is expected between theoretical lift height and the velocity squared with a

slope of $-\frac{K+1}{2g}$. Thus, theoretical lift is plotted against the square of the velocity in Figure 6.11 to study this behavior.

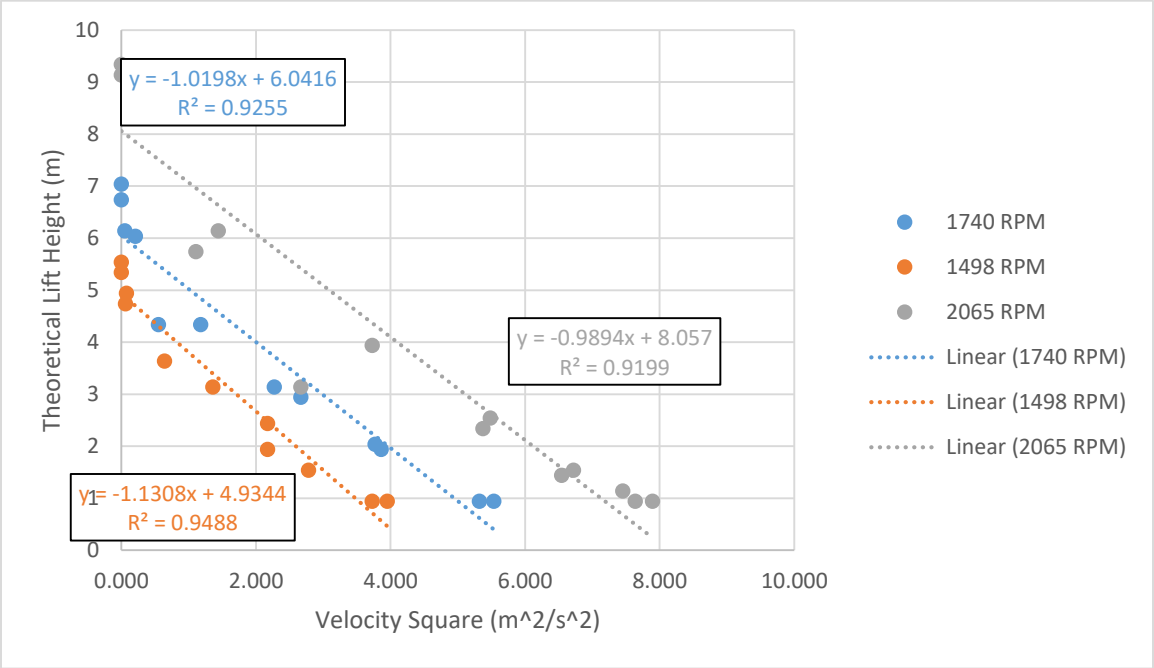

Figure 6.11. Theoretical Lift Height vs. Velocity Squared

In Figure 6.11, the theoretical lift height decreases with the square of the velocity. The relationship between these two variables is curve fit linearly, with R-squared values greater than 0.90 at all three RPMs. These three linear fits also exhibit similar slopes, which are -1.1308, -1.0198, and -0.9894. From Equation 6.11, the loss coefficient can be calculated from the average of these slopes as 19.54. This is consistent with the 21.75 value calculated in Section 6.1.2, with a difference of only 5.6%. Thus, this section validates the loss factor analysis from Section 6.1.2 and suggests an effective approach to mathematically estimate the pump flow rate at a specific lift height by testing using a valve at different valve positions.

Now with this correlation defined, a method to select the most efficient pump can be developed for customers in the next section.

6.1.5 Method of Pump Selection

After the analyses in Section 6.1 have been completed, performance parameters, such as total dynamic head (TDH) and fuel efficiency of the pump, may be evaluated, and a method of pump selection developed based on its efficiency at the specified operating conditions. This section begins with the performance evaluation.

The first step in the performance evaluation process is to eliminate the effects of the test rigs. As discussed in Section 6.1.2, the testing apparatus introduced in this thesis will not be used by customers in their irrigation system. The addition of these components with their attendant friction losses leads to underestimates of the discharge rate. Therefore, it is pointless to simply study the test results without eliminating the extra losses. This is solved by using Equation 6.4, which gives the expected discharge rate at a given operating condition.

The second step calculates the expected total dynamic head (TDH) from the expected discharge rate. By definition, TDH of a pump system is the change of the sum of pressure head, velocity head, and elevation head across the system, as shown in Equation 6.17 (Pump Handbook),

$$\mathrm{TDH} = \Delta\left(\frac{V^2}{2g} + \frac{p}{\rho g} + z\right) \qquad \textit{Equation 6.17}$$

By defining the fluid entrance to the pump as at the surface level of the water source, then the velocity, gage pressure, and elevation are all zero. Therefore, TDH may be simplified as Equation 6.18,

$$\text{TDH} = \left(\frac{V^2}{2g} + \frac{p}{\rho g} + z \right)_{\text{outlet}} \qquad \textit{Equation 6.18}$$

where $V = \frac{Q}{\frac{\pi d^2}{4}}$ is the average velocity, *z* is the theoretical lift height from Section 6.1.4, and *p* has a gage pressure of zero atmosphere. Note that due to the friction loss being directly proportional to V^2, TDH decreases at high flow rates.

The third step calculates the fuel efficiency. This requires the definition of several other terms. The equivalent delivered water power is defined by Equation 6.19,

$$w.p = Q * TDH * \rho * g \qquad \textit{Equation 6.19}$$

and the fuel consumption rate is defined by Equation 6.20,

$$f_{cr} = \frac{(f_i - f_f)}{\rho_{fuel} * t} \qquad \textit{Equation 6.20}$$

where f_f is final fuel weight, f_i is initial fuel weight, ρ_{fuel} is fuel density = 0.832 kg l^{-1} for diesel fuel, and *t* is elapsed time. The input brake power is defined by Equation 6.21,

$$b.p = E_f * f_{cr} \qquad \textit{Equation 6.21}$$

where E_f is fuel energy content = 35.86 x 10^6 J $l^{-1}$for diesel fuel. The fuel efficiency can thus be calculated in percentage by Equation 6.22,

$$\eta_f = \frac{w.p}{b.p} * 100\% \qquad \textit{Equation 6.22}$$

and water delivery efficiency can be calculated in liters water per liter fuel by Equation 6.23,

$$\eta_{wd} = \frac{Q}{f_{cr}} \qquad \textit{Equation 6.23}$$

The pump curve of expected TDH and fuel efficiency now may be generated for a pump running at a fixed RPM. Note that this performance evaluation method is not limited to axial flow pumps. It works on mixed flow pumps and centrifugal pumps. In Figure 6.12, a sample plot is generated for a mixed flow impeller running at 1740 RPM from Replication 1 of BG GI 1 Model. In this figure, the best operation point is found at the point of highest fuel efficiency, approximated 30 L/s.

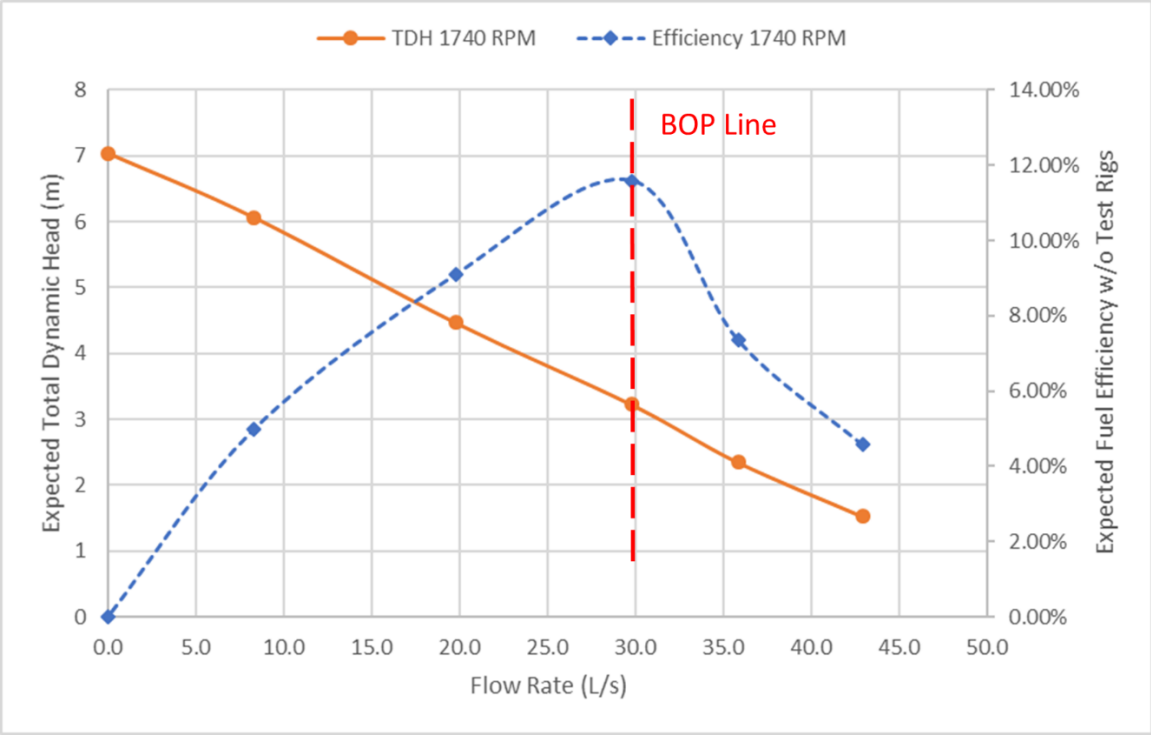

Figure 6.12. Sample Pump Curve from BG G1 Model

Similar pump curves can be generated for different pumps and different RPMs. Nevertheless, a figure of theoretical lift heights and expected fuel efficiency is more straightforward than a traditional pump curve. Considering Bangladeshi customers, this should be a more effective approach. To demonstrate such an approach, a sample figure generated using the same set of data from Replication 1 of BG G1 Model is shown in Figure 6.13. In this case, the performance of pump at various rotational speeds are plotted together.

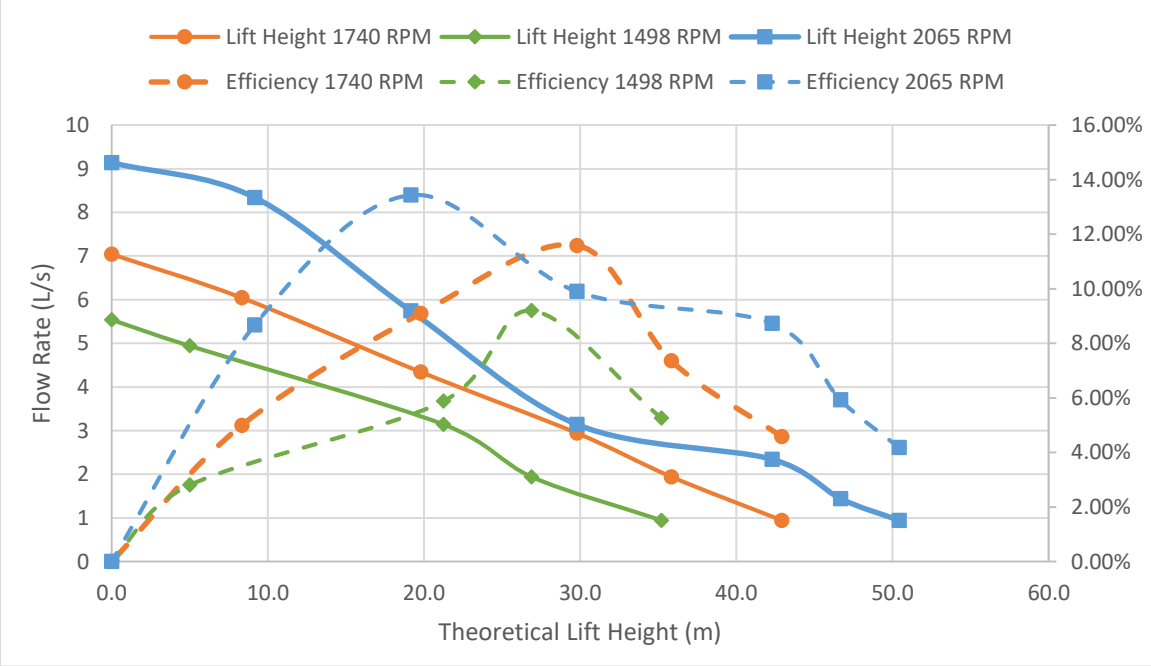

Figure 6.13. Sample Theoretical Lift Height and Expected Efficiency vs. Flow Rate

In Figure 6.13, the flow rate is on the x-axis, while the theoretical lift height and expected fuel efficiency in the field are shown on the primary and secondary y-axes, respectively. At each RPM, the theoretical lift height vs. flow rate is plotted as solid lines, while that of expected fuel efficiency vs. flow rate is plotted as dashed lines. In this case,

six curves at three different operating RPMs are included. This figure allows customers to easily find the expected fuel efficiency and compare it to that of other types of pumps.

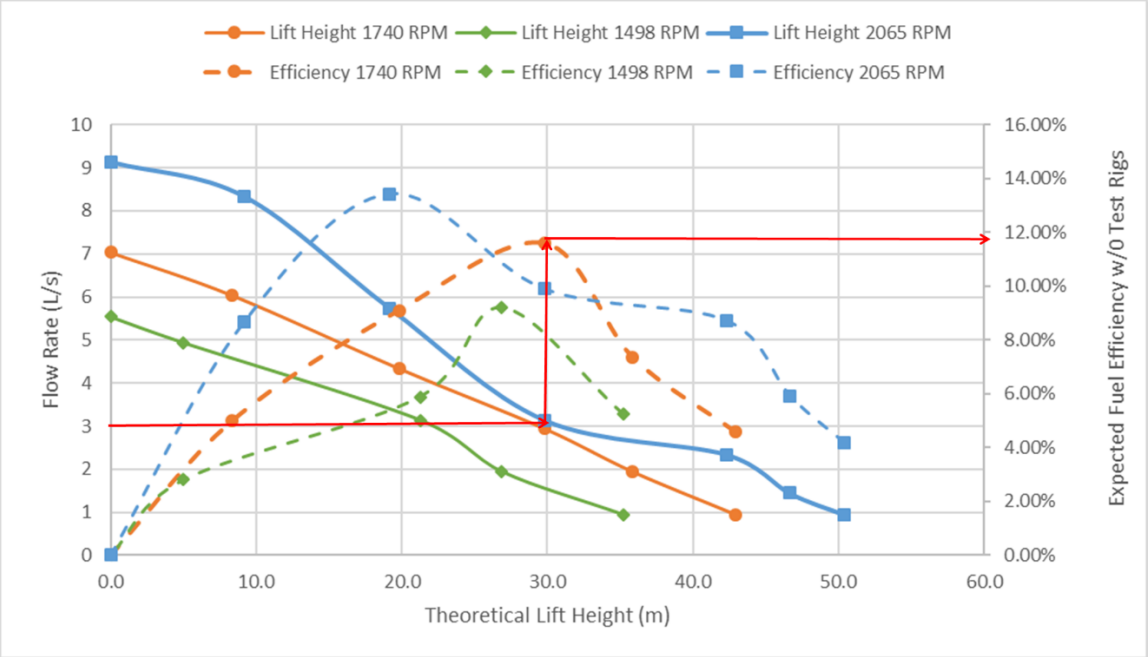

Figure 6.14. Demonstration to find Expected Fuel Efficiency

This process can be performed by following the demonstration above in Figure 6.14. Typically, customers purchase pumps having lift height and flow rate expectations. Using this figure, customers can locate a desired pump speed from the theoretical lift height curve. After that, customers can find an expected efficiency by locating the efficiency curve at the same flow rate. For example, as demonstrated in Figure 6.14, a customer looking for a lift height of 3 m and a flow rate of 30 L/s may find a desired pump speed of 1740 or 2065 RPM and a fuel efficiency of approximately 12% or 10%, respectively, for this pump. Typically, a pump operates at 1740 RPM because of a higher fuel efficiency. By performing this process on other pumps, customers will be able to compare their fuel efficiency, and thus select the most energy efficient pump. Note that

the customer may not be able to obtain a pump speed that exactly matches the desired lift height and flow rate. In this case, the solution may be approximated using the Affinity Law discussed in Section 6.1.3 to scale from the closest testing data.

6.1.6 Section Summary

Section 6.1 analyzes the full-scale testing results and discusses the significance of the full-scale testing in Bangladesh. Section 6.1.1 introduces the geometry of the impeller and the geometrical variation among the six samples. Because results from testing are limited, Sections 6.1.2 – 6.1.4 analyze the test results in order to extend application to fit all customer needs. Section 6.1.2 discusses the pump performance estimation at different friction losses from different components. Section 6.1.3 discusses the pump performance estimates at different pump speeds. Section 6.1.4 discusses the pump performance estimates at different lift heights. Finally, Section 6.1.5 utilizes knowledge of all previous sections and develops a pump selection method from the efficiency analysis. These full-scale results are further validated by prototype testing and CFD simulations.

6.2 Prototype Results

This section presents and discusses the results of testing prototype impellers performed with a small-scale test apparatus on the Georgia Tech campus. Prototype testing is designed as experimental validation of full-scale testing. Specifically, the validation is done similarly to Section 6.1. Section 6.2.1 investigates the effect of geometric variation from manufacturing on the pump performance. Section 6.2.2 validates the concept of major and minor losses on the prototype testing apparatus. Section 6.2.3 applies the Affinity Law to study the prototype results at different RPMs.

Section 6.2.4 qualitatively and quantitatively compares the full-scale and small-scale test results using the Affinity Law at different impeller sizes. Section 6.2.5 summarizes the essential outcomes of this section.

6.2.1 Tests Corresponding to Geometric Variation

This section studies the effects of geometric variations on pump performance due to manufacturing. It begins with the production of prototypes. After the measurements of the set of six full-scale impeller samples, six geometrically similar impeller prototypes are 3D-printed using full deposition modeling. These prototypes are scaled down from the full-scale samples to a uniform diameter of 2.84 in, or 72.2 mm, in order to have a constant clearance of 4 mm, which is selected from a previous irrigation pump study (Aban and International Rice Research Institute, 1985). Note that during the scaling process, each prototype is scaled down uniformly from the corresponding sample except the hole at the center, of which the diameter is kept at 0.25 inches to match that of the shaft. Once the prototypes are printed, measurements of some major design parameters are taken to examine the quality of the scaling. From results listed in Table F1 of Appendix F, the prototypes are proved to be geometrically similar to the full-scale samples by having an average difference of 1.2% in height and 0.1% in hub diameter between measured and expected values.

These prototypes are tested in the small-scale apparatus using the procedures described in Section 4.2. The small-scale apparatus, however, is not geometrically similar to the full-scale apparatus due to different available equipment. For example, the total length of the pipes is reduced due to the limited space in the laboratory. A 90° angle is

also used in the small-scale apparatus to replace the flexible hose in the full-scale one used for the same purpose. During the prototype testing process, each impeller prototype is tested three times at each shaft speed (1000 RPM, 1500 RPM, and 1744 RPM). The highest shaft speed of 1744 RPM is chosen to match the maximum available RPM of the motor in the prototype apparatus. The results from 54 sets of experiments in both open and closed valve positions are listed in Table F2 of Appendix F and highlighted in Figures 6.15 and 6.16.

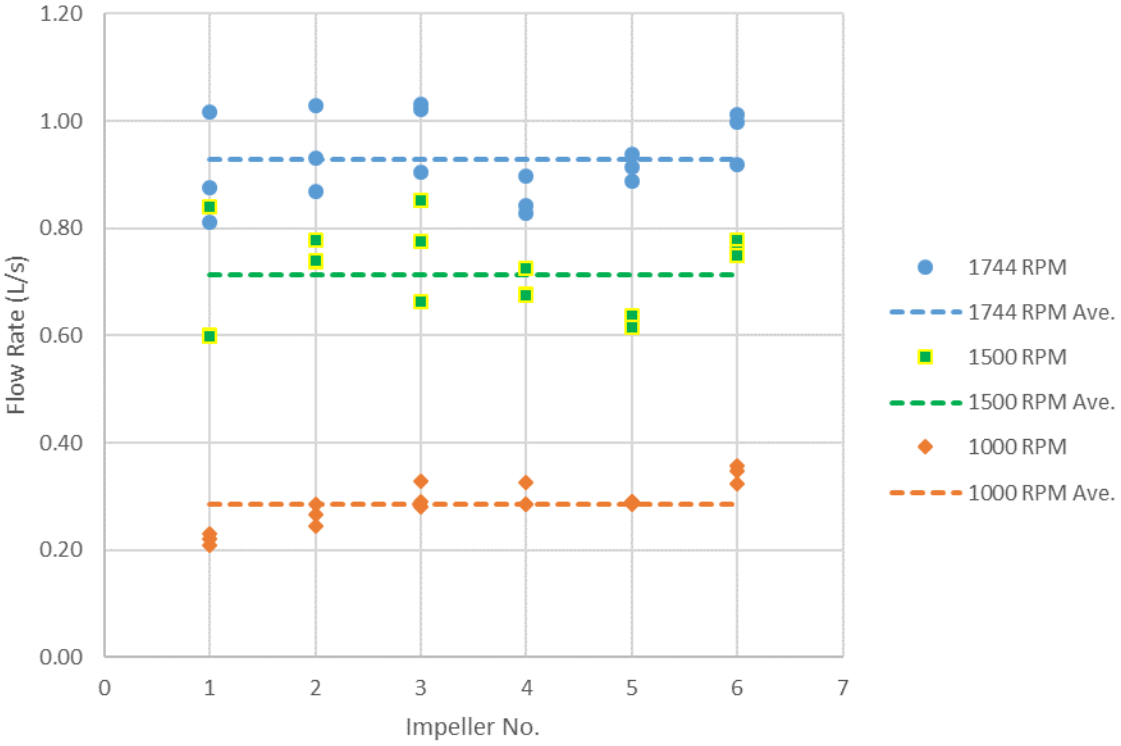

Figure 6.15. Maximum Flow Rates of Prototype Impellers

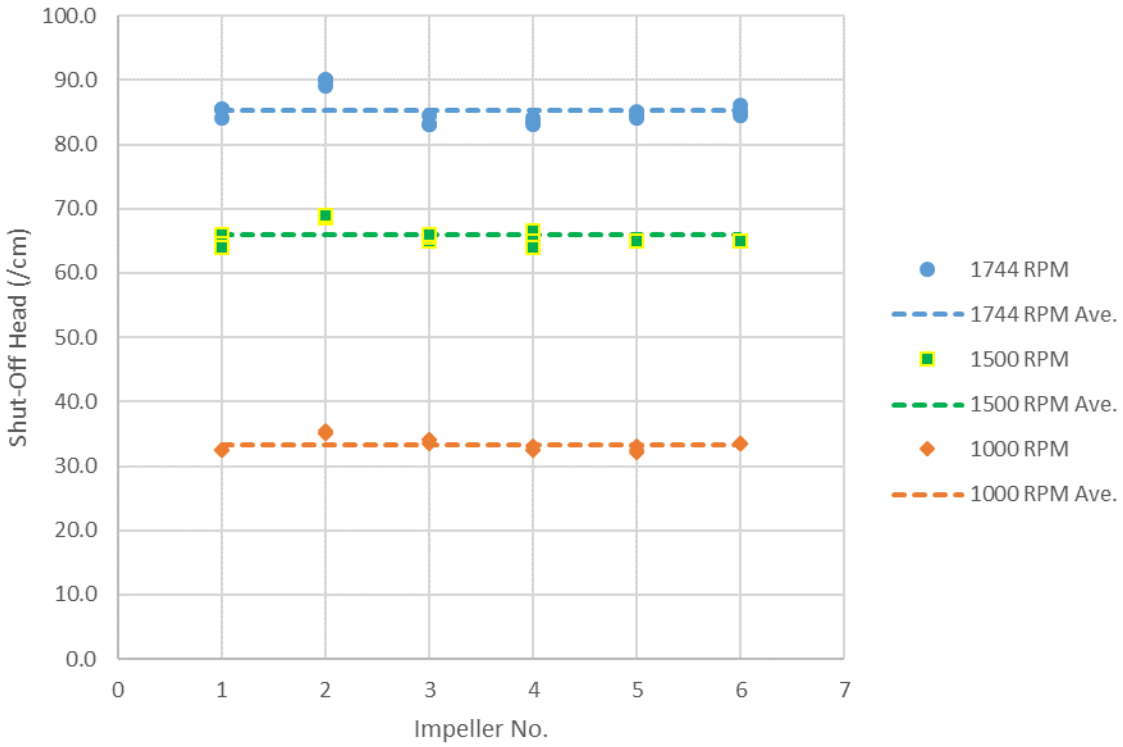

Figure 6.16. Shut-Off Heads of Prototype Impellers

From Table F2 in Appendix F, impeller prototypes have average flow rates of 0.93, 0.72, and 0.29 L/s and average shut-off heads of 85.2, 65.7, and 33.4 cm at shaft speeds of 1744, 1500, and 1000 RPM. The sample standard deviations of the flow rate are 0.07, 0.08, and 0.04 L/s for these shaft speeds, which correspond to 7.8%, 11.1%, and 14.3% of the average flow rates. The sample standard deviations of the shut-off head are 2.23, 1.56, and 1.01 cm, which correspond to 2.6%, 2.4%, and 3.0% of the average shut-off heads. The ratio of standard deviation and average value are plotted in Figure 6.17.

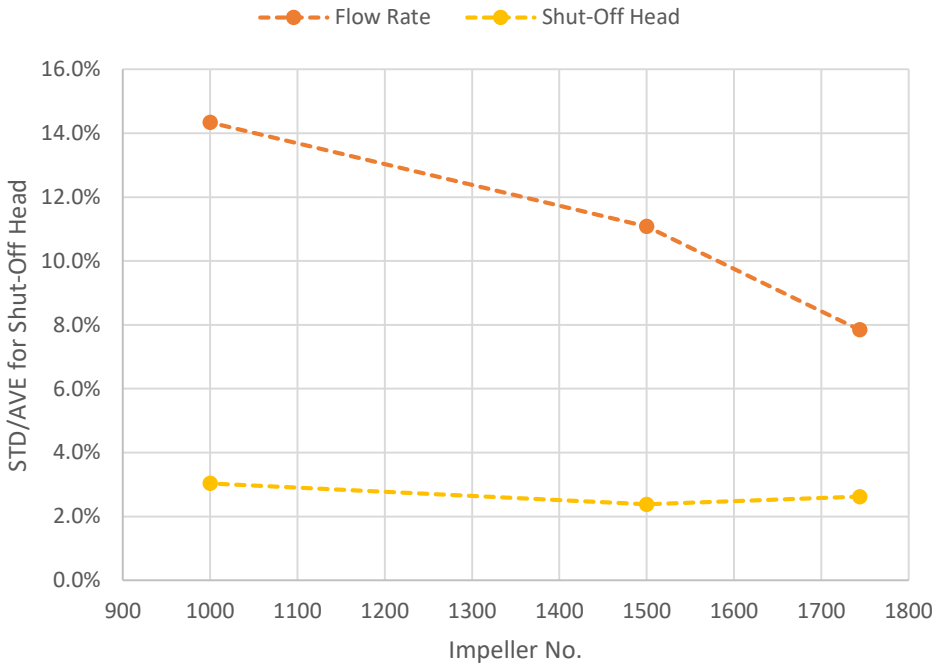

Figure 6.17. Ratio of Standard Deviations and Averages for Prototype Impellers

Based on these results, the performance of the six impeller prototypes demonstrates a strong consistency in terms of shut-off head, of which the standard deviation is limited to within 3.0% of average for all three shaft speeds. This consistency is ensured by the approximate steady-state behavior of the system when the valve is closed, which significantly reduces the uncertainty from measurements. Because the 3.0% variation in standard deviation accounts for the geometric variations of prototype impellers as well as experimental errors such as the vibration of pipe systems and the water leakage from the shaft hole, the real effect of geometric variation on the uncertainty of pump's performance will be smaller than that from this calculation.

The performance of the six prototypes in terms of flow rate keeps the ratio between standard deviation and shaft speed to within 15%. This is greater than that of the

shut-off head because the flow becomes less stable in the open-valve position. During the testing process, the flow rate sometimes experiences periodic oscillation resulting in variations in the data. In addition, a relationship between stability and RPM is observed. As reflected by flow rate behavior shown in Figure 6.16, the flow becomes unsteady as the shaft speed decreases. This is expected because at the shaft speed of 1000 RPM, the pump barely lifts the water above the level of the exit. In this case, most of the horizontal tube is filled with air, which results in an open-channel flow instead of an ideal pipe flow. In friction analysis, the fixed diameter is replaced by the hydraulic diameter of the "duct", which is defined by Equation 6.24,

$$D_{\mathrm{H}} = \frac{4A}{P} \qquad \textit{Equation 6.24}$$

where *A* is the cross-section area of the flow, and *P* is the corresponding parameter (Munson, Okiishi, and Huebsch, 2009). As shown by the Moody Chart in Figure 3.2, the hydraulic diameter defines the relative roughness, $\frac{\epsilon}{D_{\mathrm{H}}}$, that is used to calculate the friction factor of the major loss. Therefore, because of the open-channel flow in the horizontal tube in the case of a small shaft speed, a change in the volumetric flow rate results in a change in *A,* which further changes hydraulic diameter and friction loss and finally results in an additional change in the flow rate. This iterative loop, when combined with other factors discussed next, amplifies the friction effect at low shaft speeds such as 1000 RPM and causes unsteady flow.

Certainly, the theory of open-channel flow at low RPMs does not account for all of the unsteadiness of the flow at higher RPMs. Although not all causes of this phenomenon can be determined, a possible source is the turbulence from the assumed

system geometry. In modeling of the pump system, the inlet is assumed to be within an infinitely large water source (the reservoir model). In reality, however, the water source is a large water tank that is constantly filled in order to maintain the water level during the tests. Therefore, factors such as the position of the system's inlet inside the tank and the clearance between the inlet and bottom of the tank are all potential causes of turbulence that are not accounted for in the model. In fact, when the clearance between the inlet and the bottom of the tank is reduced by adding an extension tube below the inlet, the flow rate increases. Though there is not enough data to draw a conclusion, the extension tube seems to increase the performance by blocking turbulence generated in the tank.

In summary of the above error analysis, the causes of the relatively large ratio between standard deviation and the average include experimental error, such as the open-channel flow phenomenon and turbulence from the geometry, in addition to the geometric differences between the impellers in the set of six. Thus, it is likely that the real ratio caused by geometric difference from impellers alone is within 7.8%. It also makes the flow rate measurements less reliable than the shut-off head measurements. This flow rate estimation in combination with the small standard deviation (3% of the average) from shut-off head demonstrates a limited effect of geometric difference on pump performance among prototypes. As each of the six full-scale samples are geometrically similar to a scale model prototype that was fabricated and tested, similar limited effect is expected in full-scale products.

6.2.2 Tests Corresponding to Friction Losses

The concept of major and minor losses is also introduced to analyze the friction losses in prototype testing. This approach is used to match and validate the friction loss analysis in the full-scale testing. Thus, similar steps are followed. This section first establishes a theoretical model from geometry to calculate the loss coefficients and then compares this value with the loss coefficients calculated from test results. Unlike the full-scale model, the friction loss analysis does not need to isolate AFP and test rigs.

The friction loss analysis adopts a theoretical model with several assumptions. For example, the theoretical model adopts the reservoir assumption, and models the whole pump system as completely isolated from the atmosphere except at a single inlet and a single outlet. This assumption also models the water source to be infinitely large, which provides a steady flow at the entrance without any turbulence or cavitation. The water level is then maintained at the same level for the same reason. Within the reservoir, it is assumed that the reservoir is filled with incompressible liquid water that satisfies the continuity equations. Outside the reservoir, it is assumed that the atmosphere has a constant pressure of one atmosphere. Under these assumptions, a list of components within the “reservoir” are identified in a section view across the mid-plane of the pump system in Figure 6.18. Their loss coefficients are determined in Appendix G.

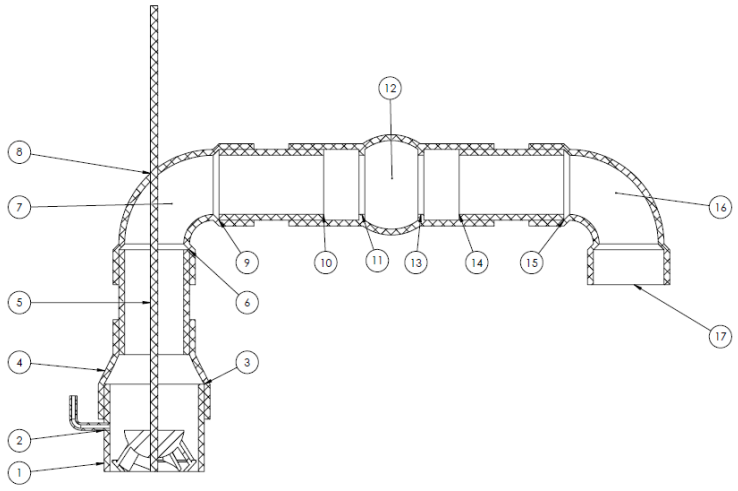

1	Protruding Inlet
2	Manometer (T-Flow)
3	Fitting (Expansion)
4	Contraction
5	Shaft
6	Fitting (Expansion & Contraction)
7	90 Degree Bend 1
8	Shaft Hole (Y-Flow)
9	Fitting (Expansion & Contraction)
10	Fitting (Expansion)
11	O-Ring 1 (contraction & Expansion)
12	Ball Valve
13	O-Ring 2 (contraction & Expansion)
14	Fitting (Contraction)
15	Fitting (Expansion & Contraction
16	90 Degree Bend 2
17	Sharp Edge Exit

Figure 6.18. Components in Prototype Testing System

As shown by the schematic of components in Figure 6.18, the prototype testing system is composed of two pipe segments of different diameters for major loss analysis and seventeen features for minor loss analysis. The major loss sums the friction effect from the inner wall of two PVC pipes with diameters of 2 inches and 3 inches, as listed in Table G1. The minor loss sums the friction effect from a ball valve, an inlet, two 90° bends, a contraction, an exit, a manometer, two sets of contraction and expansion joints, and the O-rings before and after the ball valve, as listed in Table G2. From Tables G2 and G3, the major loss again exhibits a minor friction effect in the system by having loss coefficients of approximately 0.3.

Table 6.7. Minor Loss Coefficient from Estimation and Experiments

	Estimated Minor Loss Coefficient	Loss Coefficient from Experiments
Average	13.6	14.2
STD	0.014	3.188
% Difference	4.2%	

The estimated result is then compared with experimentally calculated loss coefficients in Table G4, and highlighted in Table 6.7. It is important to note that the results of the experiments performed at 1000 RPM are not included in this comparison because of the open-channel issues discussed in Section 6.2.1. Based on results in Table G4, the estimated loss coefficient has an average of 13.6 with a standard deviation 0.014. The result shows a high consistency because the only difference between trials is the major loss under different flow velocities, of which the difference is limited to within 0.1. The calculated loss coefficient has an average of 14.2 with a standard deviation of 3.2. The standard deviation is higher than that of the estimated value largely because of the difference between the theoretical model and the real experiment. As discussed in Section 6.2.1, these differences failed to account for the turbulence generated, which caused an unsteady flow rate. From Equation 6.1, which calculates the experimental loss coefficient from the flow rate, the inconsistency of flow rate leads to an unsteady experimental loss coefficient calculation.

This unsteadiness, nevertheless, is effectively reduced by a large number of experiments. Using the averaging technique across the 36 experiments performed at 1500

and 1744 RPM, the average calculated loss coefficient demonstrated a high agreement to the estimated value by having a difference of 0.6, or 4.2% of the average calculated loss coefficient. This agreement validates the consistency of friction losses observed in prototype testing. More importantly, it assures the approach of estimating major and minor losses from geometry that is practiced in full-scale testing.

6.2.3 Tests Corresponding to Different RPMs

The Affinity Law that correlates a pump's performance at different RPMs is also applied to the prototype scale testing in order to validate the application of this approach to the full-scale analysis. Due to potential errors and variations in the experimental flow rate measurements, this analysis is applied only to correlate the shut-off head data obtained in the prototype-scale testing.

Based on Equation 3.7, the shut-off head value is proportional to the square of shaft speed. This may be expressed as a parabolic fit as shown in Equation 6.25,

$$\vec{y} = a\,\vec{x}^2 + c \qquad \textit{Equation 6.25}$$

where $\vec{x}$ represents the shaft speeds in RPM, and $\vec{y}$ represents the shut-off heads in cm of water. At x = 0, y is expected to be 0, thus yields c = 0. Then, the coefficient *a* can be calculated using Equation 6.26 as

$$a = (X^T X)^{-1} X^T \vec{y} \qquad \textit{Equation 6.26}$$

where $X = \vec{x}^2$. The corresponding R^2 value can also be determined using Equations 6.27 to 6.29,

$$SST = \sum_i (y_i - \bar{y})^2 \qquad \textit{Equation 6.27}$$

$$SSE = \sum_i (y_i - ax_i^2 - c)^2 \qquad \textit{Equation 6.28}$$

$$R^2 = 1 - \frac{SSE}{SST} \qquad \textit{Equation 6.29}$$

After calculation using Matlab, the relationship between shut-off head and shaft speed can be fit by a parabolic curve defined as $\vec{y} = 2.8762 \cdot 10^{-5} * \vec{x}^2$, with an R-squared value of 0.9745. The result is plotted in Figure 6.19.

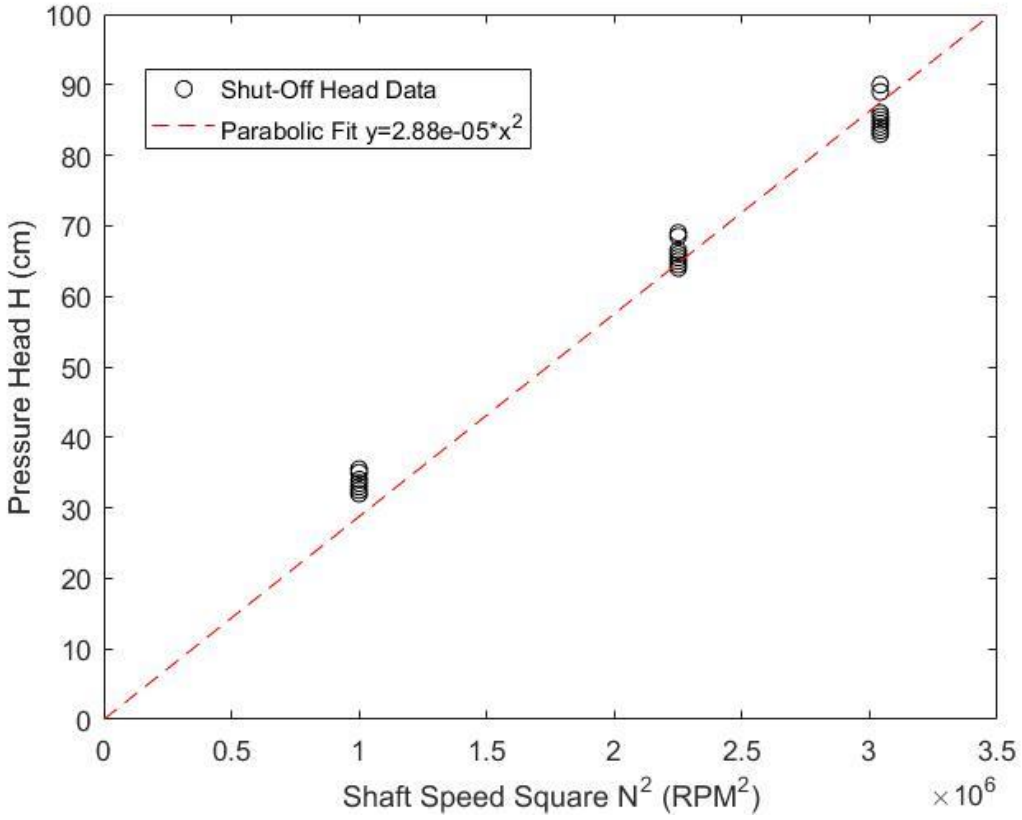

Figure 6.19. The Affinity Law Model of Prototype Shut-Off Head at Different RPMs

The result shows a high consistency between experimental data and the Affinity Law predictions at different RPMs. This validates the approach of using the Affinity Law to estimate pump performance at different RPMs in full-scale testing. The result of this

and previous subsections allows the thesis to further correlate the prototype and full-scale results using scaling.

6.2.4 Tests on Scaling between Full-Scale/Prototypes

This section attempts to match the prototype and full-scale results using the Affinity Law at different impeller sizes. As each of the six impeller prototypes is uniformly scaled down from a corresponding full-scale impeller sample, this allows the application of Equations 3.18 and 3.19 to scale the prototype results to the full-scale results. As only impellers number 3 and 4 are tested at full-scale, this approach is only applied to these two impellers. The results after scaling are included in Appendix H.

Table 6.8. Summary of Scaling between Full-Scale and Prototype Results

		Impeller 3			Impeller 4		
RPM		1741	1510	1004	1748	1498	1006
Full Scale	Flow Rate (L/s)	47.99	42.22	21.74	48.26	40.35	21.74
	Shut-Off Head (m)	8.40	6.50	2.00	8.70	6.00	2.00
Scaled Up from Prototype	Expected Flow Rate (L/s)	14.98	11.70	4.58	13.47	10.87	4.72
	Expected Head (m)	5.11	4.08	2.09	5.26	4.08	2.07

As shown in Table H1 of Appendix H and Table 6.8, the expected flow rate and shut-off head after scaling the prototypes using the Affinity Laws do not match those obtained in full-scale testing. The mismatch can be due to the differences in the testing apparatus. As the full-scale testing was performed at by BARI in Bangladesh, while the prototype-scale testing was performed at Georgia Tech, multiple factors such as the clearance between impeller and pipe interior diameter, the angle between the pipe and the water surface, the bending angle at the corners, the type of control valve, and the

measuring equipment are unavoidable. Other factors, such as turbulence, may also influence the agreement. The mismatch is expected because the Affinity Laws are rarely, if ever, successfully applied in practice, as noted in Section 3.3. As a result, the results are compared qualitatively.

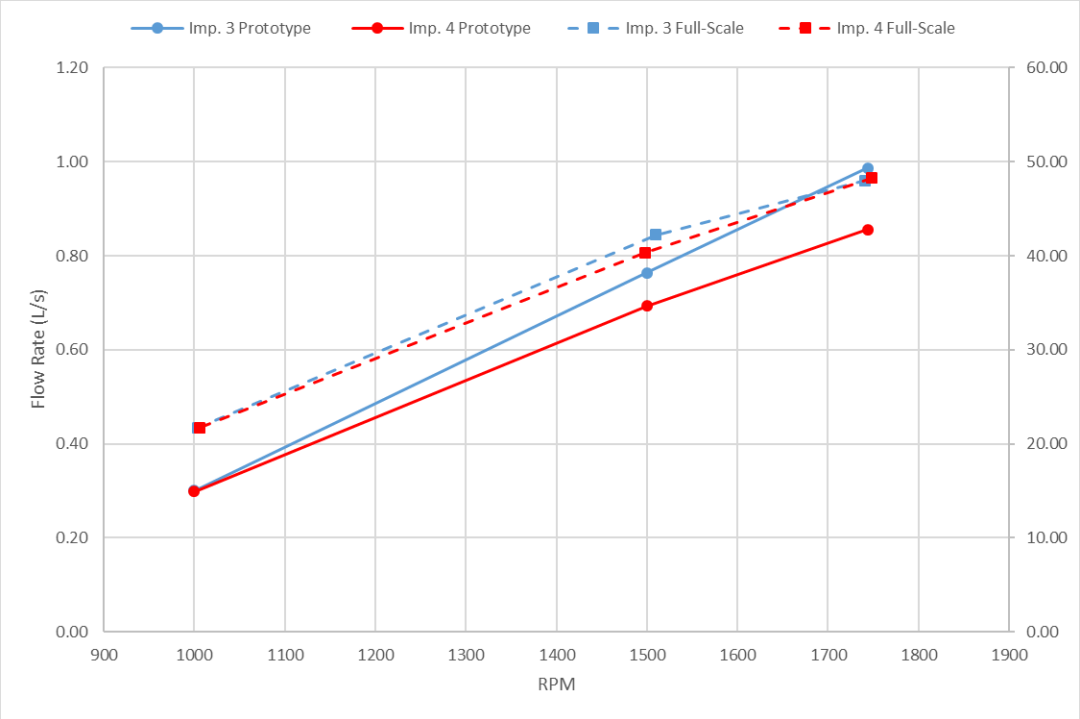

Figure 6.20. Flow Rate vs. RPM for Impellers 3 and 4

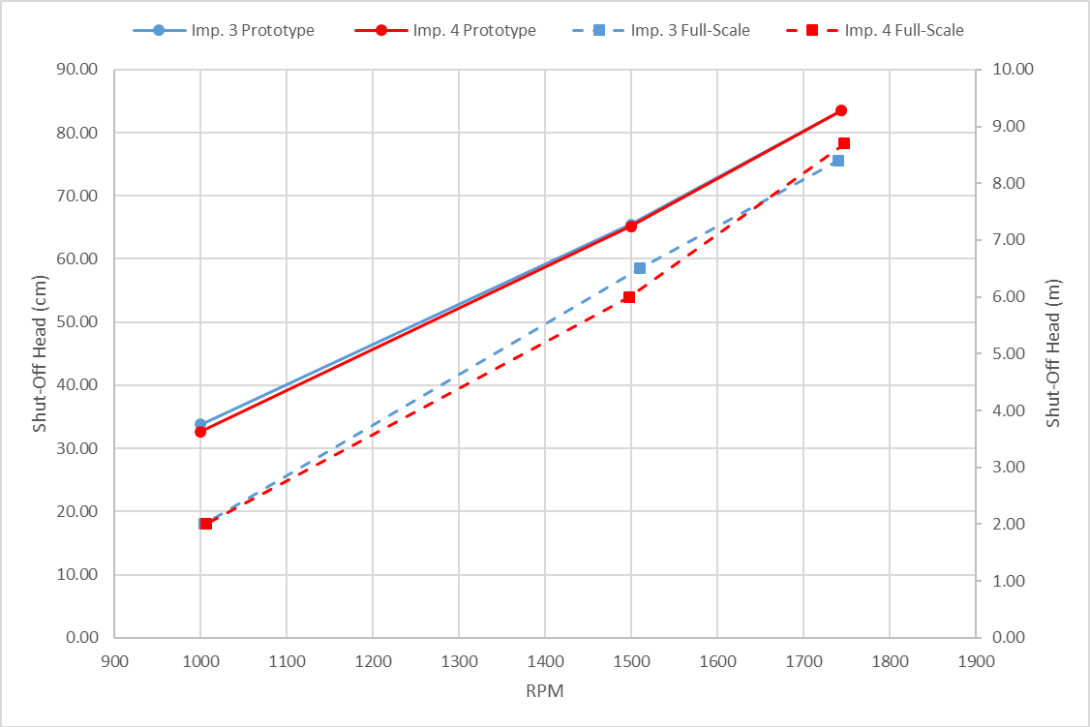

Figure 6.21. Shut-Off Head vs. RPM for Impellers 3 and 4

In Figures 6.20 and 6.21, prototype results are connected by solid lines and plotted with respect to the primary vertical axis on the left; the full-scale results are connected by dashed lines and plotted with respect to the secondary axis on the right. As both vertical axes are plotted from the origin, this allows the qualitative comparison between prototype and full-scale results. From these two figures, both tests demonstrate a similar rising trend line in each of the flow rate and shut-off head measurements. This fact indicates the qualitative consistency of prototype and full-scale behaviors in response to a change in shaft speed.

The quantitative mismatch from the direct scaling approach reduces the potential of prototype testing as a replacement for full-scale testing in this case. It emphasizes the necessity of the full-scale testing with the apparatus used in field operations. The

qualitative consistency, nevertheless, supports the use of Affinity Laws to estimate pump performance at different RPMs for tests on the same apparatus.

6.2.5 Section Summary

Section 6.2 demonstrates and analyzes the prototype testing results. This section focuses on using prototypes to reexamine various analytical approaches used for the analysis of the full-scale results. It investigates the effect of geometric variation, the modeling of friction losses and the Affinity Laws at different RPMs on impeller prototypes in Sections 6.2.1, 6.2.2, 6.2.3, respectively. During this process, error analysis is applied to quantify the differences of measured flow rates at each RPM. This section also questions the possibility of testing prototypes as a replacement of full-scale testing from direct scaling using the Affinity Laws at different impeller sizes in this case due to the limitations of the Georgia Tech test apparatus. The same approach, nevertheless, once again supports the method of pump performance estimates at different RPMs in Section 6.2.3 from a qualitative perspective.

With the validation from prototype testing, this chapter now evaluates the full-scale performances with CFD simulations in Section 6.3 and 6.4.

6.3 SolidWorks Flow Simulation Results

Section 6.3 validates the results of full-scale testing using CFD simulation performed in SolidWorks Flow Simulation. This section organizes its content in a similar manner to that for prototype testing. Due to limited computational capability, the CFD simulation only models at full-scale a short segment of the pipe entrance that contains the impeller. The other components and features of the actual pump are neglected in the

model. As a result, the CFD model is not able to examine the major and minor losses. Specifically, this section discusses the tests corresponding to geometric variations in 6.3.1, the tests corresponding to geometric variations in 6.3.2, and matching with full-scale results in 6.3.3.

6.3.1 Grid Independence Study

With the model set up as described in Section 5.1, a grid independence study is performed to validate the accuracy and reliability of the simulation results. This is done by comparing the pressure at multiple different grid sizes. When the change in pressure becomes small enough, grid independence is achieved. In this grid independence study, pump system at four different grid sizes are simulated. The results of this study are presented in Table 6.9, and a graph of which is shown in Figure 6.22.

Table 6.9. SolidWorks Grid Independence Study

Cell size /m	Shut-Off Pressure /Pa	Shut-Off Head /m	Error/Pressure
0.019	169592	6.97	
0.016	163106	6.30	4.0%
0.01	159414	5.93	2.3%
0.007	159767	5.96	0.2%

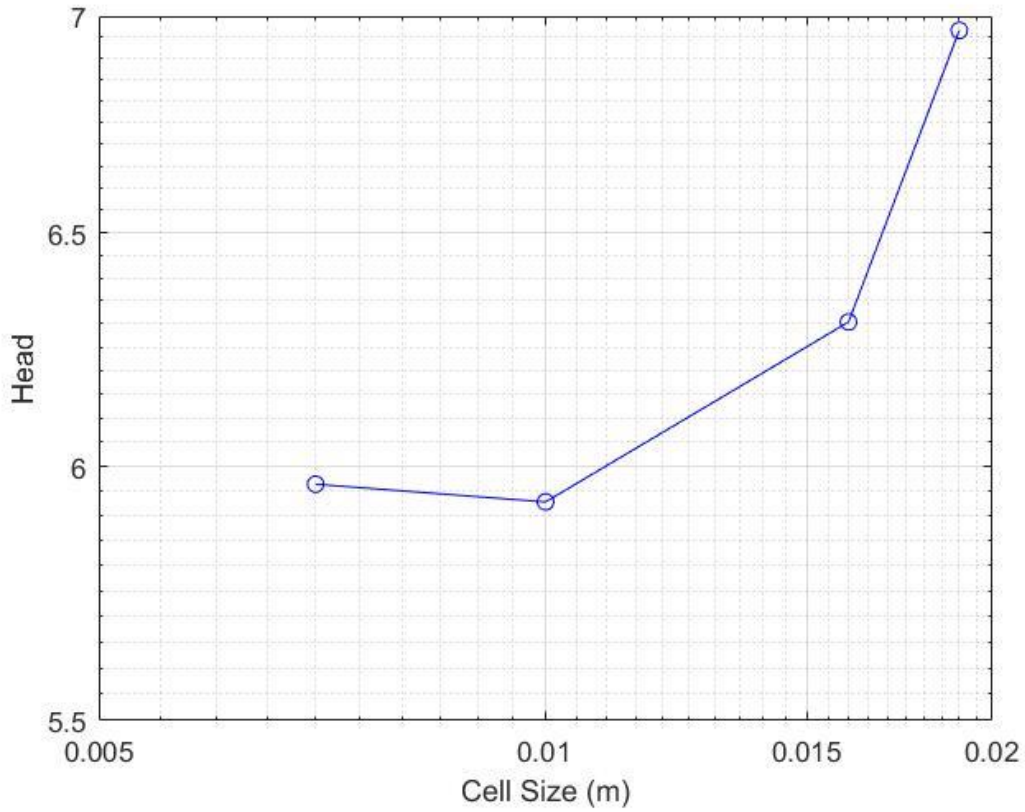

Figure 6.22. SolidWorks Grid Independence Study

The residuals at three different cell sizes are presented in Figure 6.22. As the cell sizes decreases from 0.019 m to 0.007 m, the shut-off head becomes more stable, and the error drops from 4% to 0.2% of the pressure. Based on this trend, it is expected that the error from simulation calculated at the next level will be smaller than 0.2%, or approximately 0.03 m in shut-off head. This will not result in significant differences in future analysis. Thus, the results will be grid independent at a cell size of 0.007 m. Due to geometric similarities among the set of six impellers, this grid level is carried into the modeling of this and the other five impellers.

6.3.2 Simulations Corresponding to Geometric Variation

The results of simulations corresponding to geometric differences within the set of six impellers are shown in Table 6.10. Because friction losses of components and features within the system other than the pump itself are not modeled in the simulation, calculating the volumetric flow rate from simulations would be pointless. Therefore, the simulation uses shut-off head, which theoretically is independent of friction loss within the system, to quantify the effect of geometric differences.

Table 6.10. Shut-Off Head Measurements in SolidWorks Simulation

Impeller #	RPMs		
	1744	1500	1000
1	8.57	6.06	2.83
2	8.60	6.76	3.02
3	9.04	6.89	3.01
4	8.72	6.45	2.85
5	8.28	6.65	2.80
6	8.94	6.52	2.93
Average	8.69	6.55	2.91
Standard Deviation	0.27	0.29	0.10
STD/AVE	3.2%	4.4%	3.3%

From Table 6.10, the sample standard deviations of shut-off heads of all six impellers at RPM of 1744, 1500, and 1000 are 0.27 m, 0.29 m, and 0.10 m, which correspond to 3.2%, 4.4%, and 3.3% of the average values, respectively. According to the simulation, the fact that the sample standard deviation of shut-off head at each RPM is less than 5% of the average value demonstrates a high consistency of pump performance. Based on this result, the Bangladesh factory can be 95% confident that their impellers

generate pressure heads of 7.8 to 9.6 m, 5.6 to 7.5 m, and 2.6 to 3.2 m at pump speeds of 1744 RPM, 1500 RPM, and 1000 RPM, respectively.

6.3.3 Simulations Corresponding to Different RPMs

Using the data in Table 6.10, this section validates the Affinity Law at different RPMs on the CFD model simulated in SolidWorks. Similar to Section 6.2.3, this section used Equations 6.26 to 6.29 to calculate the optimum parabolic fit for shut-off heads of the SolidWorks model and plotted the results using Matlab in Figure 6.23.

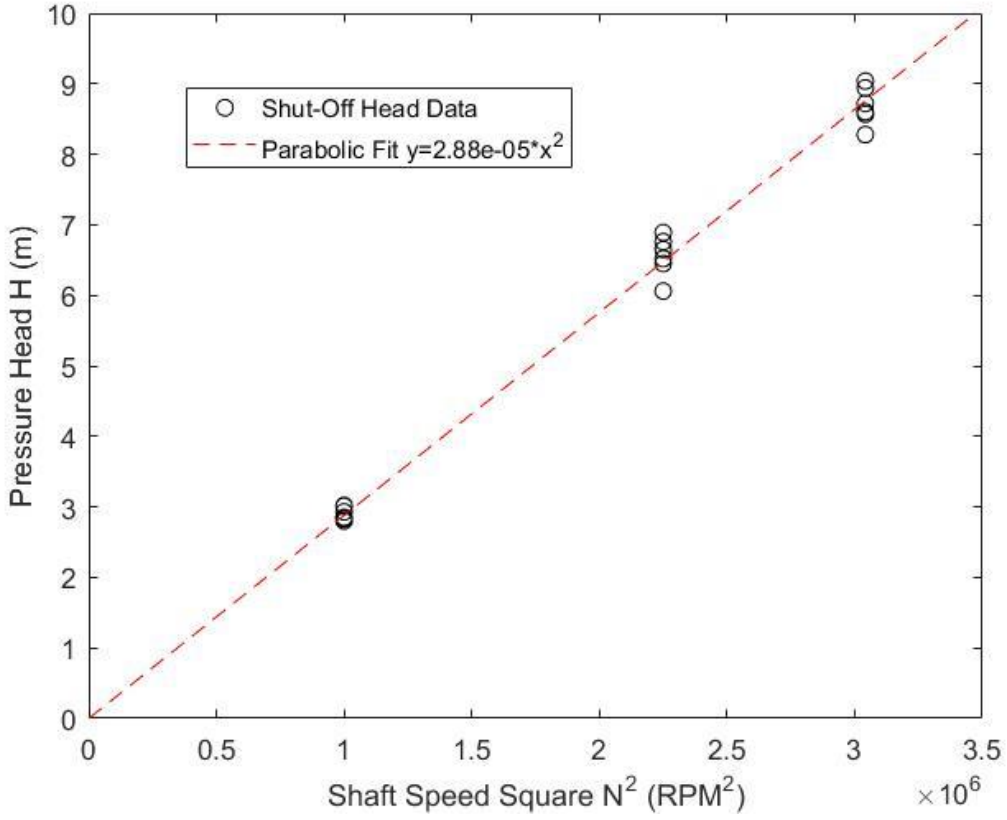

Figure 6.23. The Affinity Law Model for SolidWorks Shut-Off Head at Different RPMs

The relationship between shut-off head and shaft speed can be fit by a parabolic curve defined as $y = 2.8793 \cdot 10^{-6} * x^2$, where x represents the shaft speed in RPM and y represents shut-off head in meters. With an R-squared value of 0.9912, the result shows an excellent consistency between experimental data and the Affinity Law predictions at different RPMs. This once more validates the approach of using the Affinity Law to estimate pump performance at different RPMs in full-scale testing.

6.3.4 Matching with Full-Scale Results

The analysis now proceeds to comparing full-scale and simulated pump performance at each RPM tested. As only impellers 3 and 4 are tested at full-scale, the comparison only involves their simulation results and is shown in Table 6.11.

Table 6.11. Matching between SolidWorks Simulation and Full-Scale Testing

Impeller #	RPM	From Simulation		From Full-Scale Testing		% Difference	
		Shut-Off Head (m)	Flow Rate (L/s)	Shut-Off Head after Scaling (m)	Flow Rate after Scaling (L/s)	Shut-Off Head (m)	Flow Rate (L/s)
3	1744	9.04	48.89	8.37	47.90	8.0%	2.0%
	1500	6.89	42.07	6.59	42.50	4.6%	1.0%
	1000	3.01	25.96	2.02	21.82	49.4%	19.0%
4	1744	8.72	49.21	8.74	48.37	0.3%	1.7%
	1500	6.45	43.24	5.98	40.29	7.8%	7.3%
	1000	2.85	26.67	2.02	21.87	41.0%	22.0%

Within Table 6.11, the results encompass the shut-off head and the estimated flow rates from both the SolidWorks simulation and full-scale testing. In the case of simulation, the shut-off heads are calculated directly by the software and are identical to those in Table 6.11. However, the volumetric flow rates are estimated from the shut-off heads using Equation 6.7 in Section 6.1.4, for which the loss coefficients are obtained from Table C1 of Appendix C. In the case of full-scale testing, values of both shut-off heads and flow rates are scaled from the original values in Table C1 using the Affinity Laws at different RPMs in order to match those from the SolidWorks simulations, based upon the Affinity Law's validation in Subsection 6.3.2.

From the results shown in Table 6.11, the impellers demonstrate a steadier behavior at higher shaft speeds. At 1500 and 1744 RPM, both impellers have results within 8% of the full-scale testing value in categories of both shut-off head and flow rate. At 1000 RPM, this percent difference rapidly increases to approximately 20% in flow rate and over 40% in shut-off head. This indicates regular behavior of the pump at 1500 and 1744 RPM, but far from it at 1000 RPM. Possible sources of the non-ideal behavior may be the turbulence and open-channel phenomena discussed in Section 6.2. Due to their nature as shown in Section 3.1, AFPs and MFPs are most efficient at high shaft speeds. At low shaft speeds, such as 1000 RPM, these pumps are likely to be replaced by CPs for a higher efficiency. Therefore, it can be concluded that the SolidWorks simulations agree well with the results of the manufactured impellers in the desired range of operation.

6.3.5 Section Summary

Section 6.3 examines the results of full-scale testing using the SolidWorks Fluid Flow simulation. This section reviews the simulated results in perspectives of geometric variation, the Affinity Laws at different RPMs, and the agreement with data from full-scale experiments. Based on this simulation, the section shows a small standard deviation within 5% of the average, for the shut-off head for each of the six impellers, an excellent consistency with the Affinity Laws at different RPMs. There is also a good agreement between simulations and full-scale testing results at 1500 and 1744 RPM. In the next section, the thesis repeats the above approaches to test the CFX simulations.

6.4 ANSYS CFX Simulation Results

Section 6.4 discusses the CFD testing results of full-scale impellers using ANSYS CFX. As discussed in Section 5.2, the CFX simulation adopts a similar problem setup as described in the previous section for the SolidWorks Flow Simulation. Limited by computational capability, the simulation did not include features and components in the system other than the impeller and the pipe segment and evaluated the pumps' performance in terms of their shut-off head. The rest of this section is organized as follows. It first discusses the grid independence study in Section 6.4.1, the pressure distribution and measurements in 6.4.2, the tests corresponding to geometric variation in 6.4.3, the tests at different RPMs in 6.4.4, and finally the correlation between the simulation results and experimental results in 6.4.5.

6.4.1 Grid Independence Study

Once the model is setup as described in Section 5.2, a grid independence study is performed prior to other cases in order to validate the accuracy and reliability of the results. This is done by comparing the measured pressures at multiple different grid sizes. When the change in measured pressure becomes insignificant as the grid is further refined, grid independence is achieved. The results of this study are presented in Table I1 in Appendix I, and a graph of which is shown in Figure 6.24.

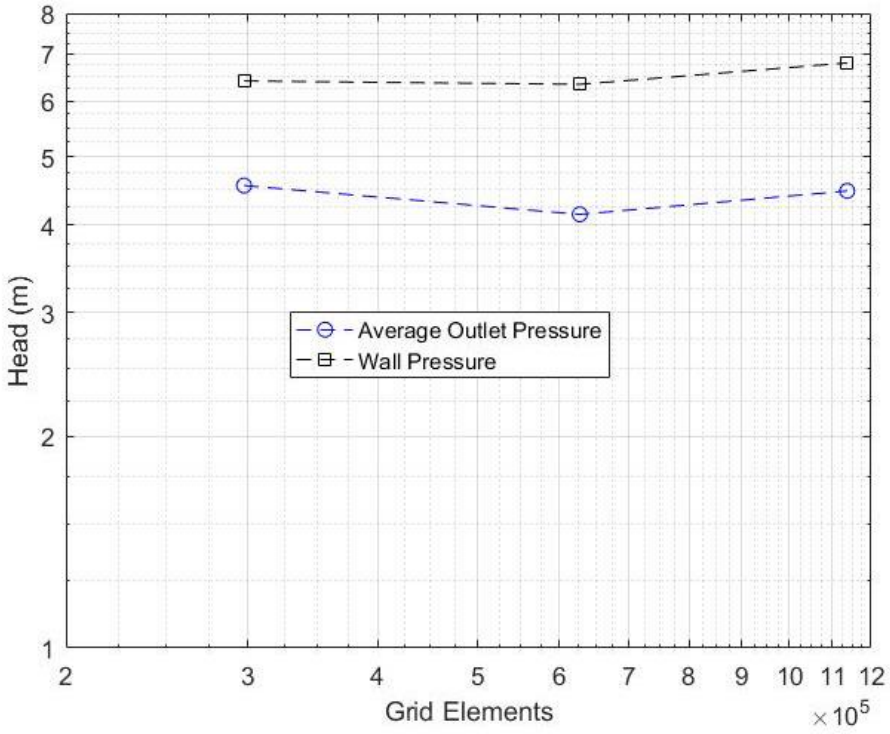

Figure 6.24. CFX Grid Independence Study

In order to study grid independence, three cases calculated under the same problem conditions but with different grid sizes are compared. As noted by Table I1, all cases are simulated with the CAD model of impeller 3 at a pump speed of 1500 RPM and a residual of 0.0001. As the maximum size of the element decreases from 0.01579 m to

0.005 m to 0.004 m, the total number of elements increases approximately by a factor of 2 to values of 2.97E5, 6.27E5, and 1.16E6, respectively. From the simulation results, the effective increase of pressure between the outlet wall and the inlet is calculated to be 4.56 m, 4.14 m, and 4.47 m, and that between the inner wall of the pipe segment after the impeller and the inlet is calculated to be 6.41 m, 6.34 m, and 6.80 m at each grid level. As shown by a logarithmic plot in Figure 6.23, two refinements of grid level lead to insignificant changes. In fact, the changes in both head measurements are limited to less than 7.4%.

Hence, the results are grid independent at a grid level of 0.01579 m. Due to geometric similarities of the six impellers, this grid level is carried into the modeling of this and the other five impellers. Thereafter, CFX is validated to test the performance of these impellers through CFD simulation.

6.4.2 Pressure Distribution and Measurements

In order to accurately reflect the impellers' performance and to connect the significance of the simulation to experimental testing, it is essential to address the pressure measurement process. This is better explained with the pressure distributions shown in Figures 6.25 and 6.26.

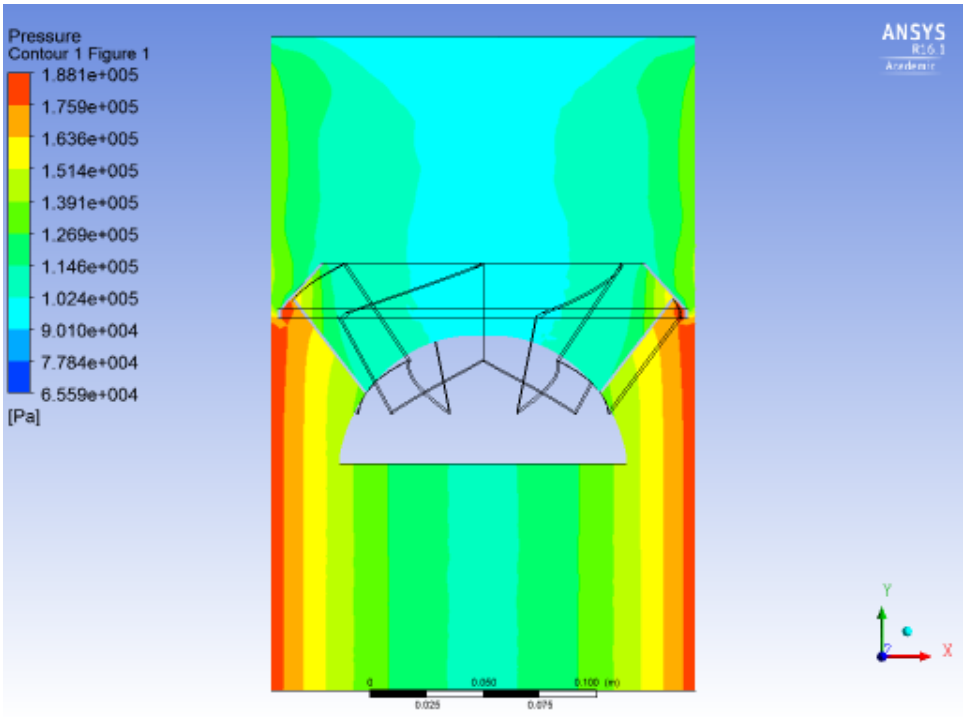

Figure 6.25. CFX XY-Plane Pressure Contour

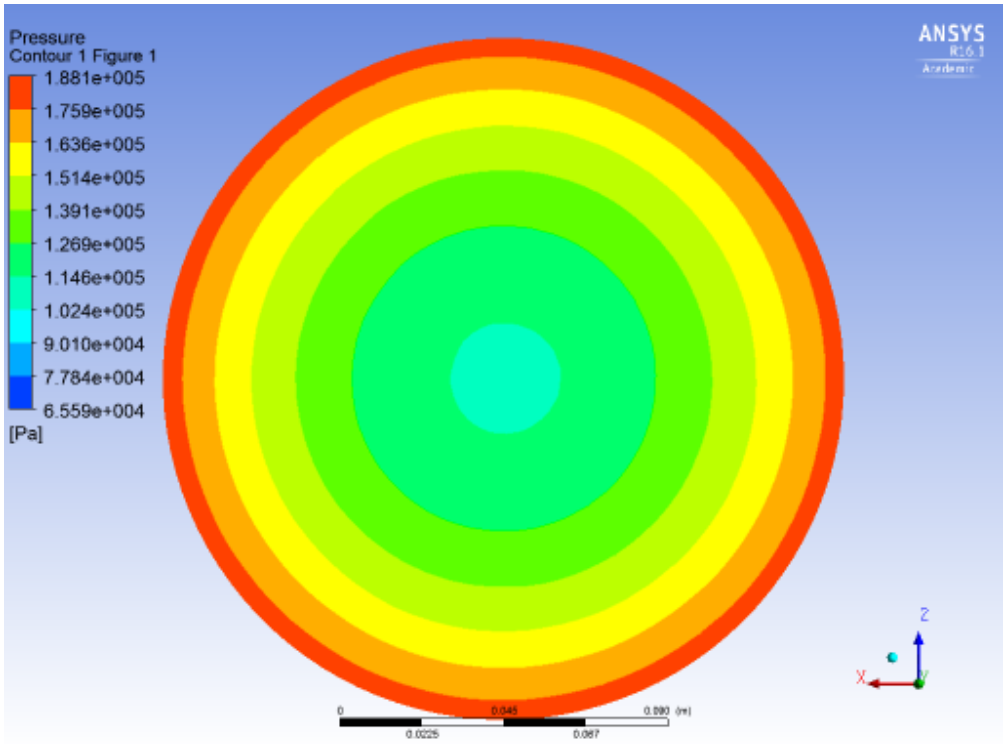

Figure 6.26. CFX Outlet Pressure Contour

Figures 6.25 and 6.26 are pressure distribution contours taken at the XY-Plane and the outlet, respectively. Both figures are obtained from a steady-state simulation for impeller 6 operating at 1744 RPM with a pressure of one atmosphere at the opening. Based on a qualitative observation of Figure 6.25, the pressure distribution becomes independent of the y-axis at the XY-Plane after the impeller. Similarly, by observing Figure 6.26, the pressure distribution appears to be axisymmetric about y-axis at the outlet. A combination of these two observations indicates a one-dimensional pressure distribution that is both independent of and axisymmetric about the y-axis. This matches the flow profile of a fully developed pipe flow as described in Munson, Okiishi, and Huebsch, 2009. Therefore, the pressure distribution can be simplified as shown in Figure 6.27.

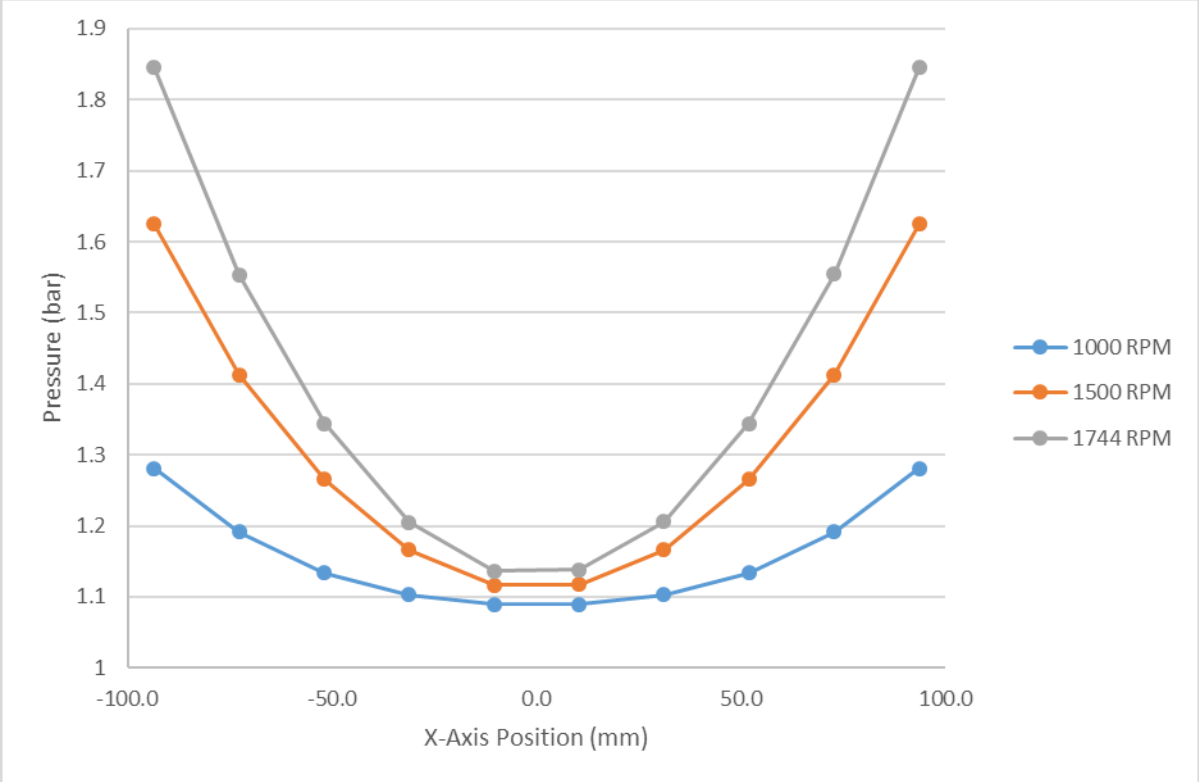

Figure 6.27. CFX Outlet Pressure Distribution Plot

Figure 6.27 demonstrates the one-dimensional pressure distribution at the outlet where $z = 0$. This is generated by impeller 6 at three different pump speeds - 1000, 1500, and 1744 RPM - with a pressure of one atmosphere at the opening. According to Figure 6.27, the pressure varies with respect to x-axis position, or the radius, in all three RPMs. Fluid cells closer to the inner wall of the pipe exhibit a higher pressure than those at the center. This phenomenon makes it critical to measure the shut-off head at the correct position.

Based on the full-scale testing apparatus shown in Figure 4.6, the pressure gauge measures the pressure approximately at the wall. Thus, the wall pressure, or the maximum pressure at the outlet, is collected for analysis in order to compare with data from full-scale experiments. Note that because the length of the pipe segment is limited, the comparison between simulation and experimental results assumes minimal effects of other geometric components on the qualitative pressure distribution. Using this assumption, the simulation results presented in the following sections are analyzed.

6.4.3 Tests Corresponding to Geometric Variation

Table 6.12. Shut-Off Head Measurements (in m) in CFX

	RPMs		
Impeller #	1744	1500	1000
1	9.26	6.83	3.04
2	8.83	6.63	2.96
3	7.96	5.96	2.64
4	9.22	6.80	3.03
5	9.16	6.76	3.01
6	9.17	6.70	2.99
Mean	8.93	6.61	2.95
Standard Deviation	0.50	0.33	0.15
STD/AVE	5.6%	5.0%	5.2%

Table 6.12 lists the measured shut-off heads from CFX simulations performed with the set of six impellers at pump speeds of 1744 RPM, 1500 RPM, and 1000 RPM. From Table 6.12, these impellers have an average shut-off head of 8.93 m, 6.61 m, and 2.95 m at pump speeds of 1744 RPM, 1500 RPM, and 1000 RPM, respectively. The sample standard deviations are calculated as 0.50 m, 0.33 m, and 0.15 m, corresponding to 5.6%, 5.0%, and 5.2% of the average at each of the three RPMs. This gives a 95% confidence interval of 1.0 m, 0.6 m, and 0.3 m on the shut-off head performance at 1744 RPM, 1500 RPM, and 1000 RPM. The limited variation of shut-off head that results within the set of six impellers validates the consistency of their performance from the CFX approach.

6.4.4 Tests Corresponding to Different RPMs

Using the data in Table 6.12, this section investigates the correlation of impeller performances at different RPMs based on CFX simulation results. Similar to Sections 6.2.3 and 6.3.2, this section uses Equations 6.26 to 6.29 to calculate the optimum parabolic fit for shut-off head and attempts to connect it with the Affinity Laws. The parabolic fit is plotted using Matlab in Figure 6.28.

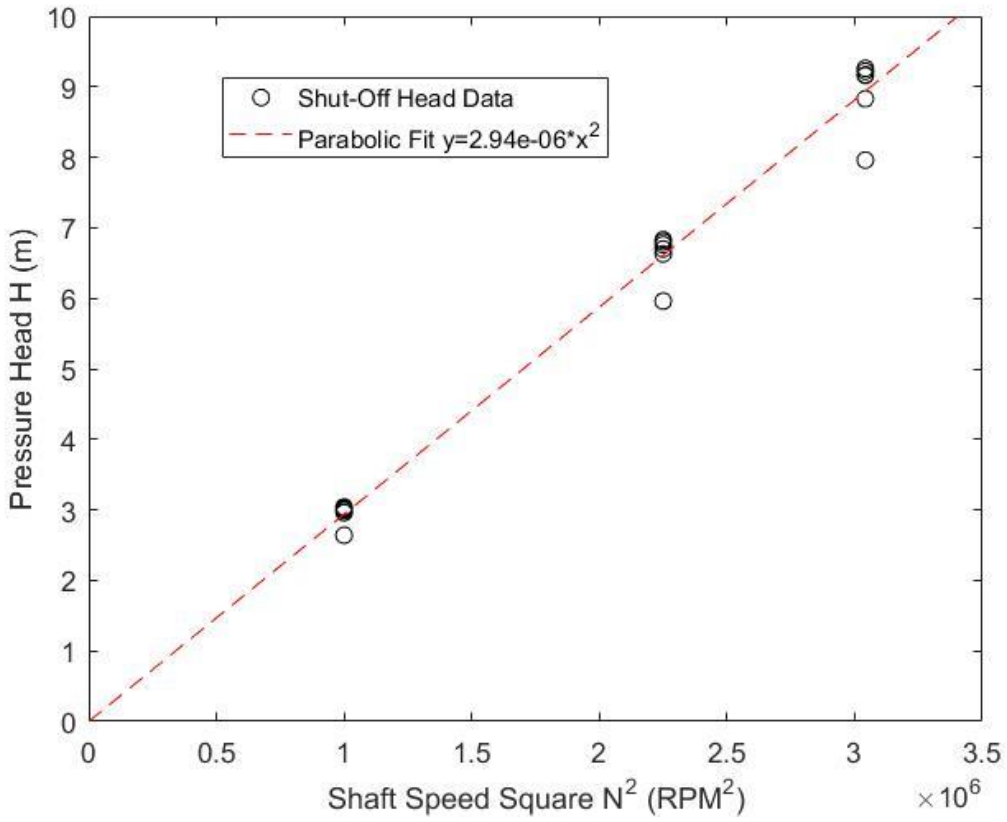

Figure 6.28. The Affinity Law Model for CFX Simulation at Different RPMs

As shown in Figure 6.28, the relationship between shut-off head and shaft speed is best described by the parabola $y = 2.9383 \cdot 10^{-6} * x^2$, where x represents the shaft speeds in RPM and y represents shut-off heads in m. With an R-squared value of 0.9829,

the results show a high consistency between experimental data and the Affinity Laws' predictions at different RPMs. This further validates the approach of using the Affinity Laws to estimate pump performance at different RPMs in full-scale testing.

6.4.5 Matching between Simulation and Experiments

With the results analyzed and validated, the section proceeds to comparing CFX simulation results and full-scale experimental results. As only the impellers 3 and 4 are tested in full-scale experiments, this section compares the performances of only these two impellers, as shown in Table 6.13.

Table 6.13. Shut-Off Head of CFX Simulation and Full-Scale Experiment

Impeller #	RPM	Shut-Off Head (m)		
		CFX Simulation	Full-Scale Experiment	% Difference
4	1744	9.22	8.74	5.4%
	1500	6.80	5.98	13.6%
	1000	3.03	2.02	49.6%
3	1744	7.96	8.37	4.9%
	1500	5.96	6.59	9.5%
	1000	2.64	2.02	30.8%

Table 6.13 contains the shut-off head measurements from CFX simulation and full-scale experiments. Similar to the previous observation of SolidWorks Flow Simulation in Section 6.3.3, the data demonstrate better agreement at higher RPMs. At a pump speed of 1744 RPM, both impellers have a difference of approximately 5% between experiments and simulations. At 1500 RPM, this difference increases to 13.6% and 9.5%. At 1000 RPM, this difference further increases to 30% and 50%. As discussed in Section 6.3.3, possible sources of the non-ideal behavior may be the turbulence and

open-channel phenomena. Because AFPs and MFPs are used mostly in high RPM ranges, it can be concluded that the CFX simulation is in good agreement with the results of the manufactured impellers in their desired range of operation.

6.4.6 Section Summary

Section 6.4 reviews and evaluates the results of full-scale testing using the ANSYS CFX simulation. This section first performs the grid independence study to ensure the accuracy and reliability of the modeling. Then, the section clarifies the position to measure shut-off head through the pressure distribution. After that, it reviews the simulated results in perspectives of geometric variation, the Affinity Law at different RPMs, and the agreement with data from full-scale experiments. Based on this simulation, the section concludes that there is a small variation between the shut-off head values for each of the six impellers caused by geometric differences, an excellent consistency with the Affinity Laws at different RPMs, and a good agreement between simulation and full-scale testing result at 1500 and 1744 RPM. In the next section, the thesis discusses the results for design optimizations.

6.5 Potential Design Optimization

Section 6.5 seeks potential design changes in order to optimize the pumping capacity, head, and efficiency of the current impeller. Due to the high cost and large time consumption of physical prototype testing, this study is performed in a virtual environment using the CFD approach. Because of the consistency in both SolidWorks Flow Simulation and ANSYS CFX results in the previous sections, this study is performed using SolidWorks Flow Simulation due to slightly faster converging speed.

This section first introduces some obvious design factors to be optimized and the design of experiment in Section 6.5.1. Then, this section analyzes the effects of single factors and two-way interactions from the results in Sections 6.5.2 and 6.5.3, respectively. Finally, important outcomes are summarized in Section 6.5.4.

6.5.1 Design of Experiments

In the process of design optimization, four design parameters are studied to optimize the impeller's performance. These four parameters are cone height, cone diameter, overall height, and vane angle, of which the first three parameters are defined in Appendix A. The final parameter, the vane angle, is the angle of the taper helix used to define blades for the impeller. In this case, the default vane angle is set to 43°. Note that however the vane angle changes, each vane is kept at a 45° revolution and 30 mm elevation throughout the optimization process. The parameters that define the shape of the impellers' vanes are shown in Figures 6.29 and 6.30. Although the vane angle is not measured directly in Appendix A, it is reflected in the measurements of vane width as shown in Figure A1.

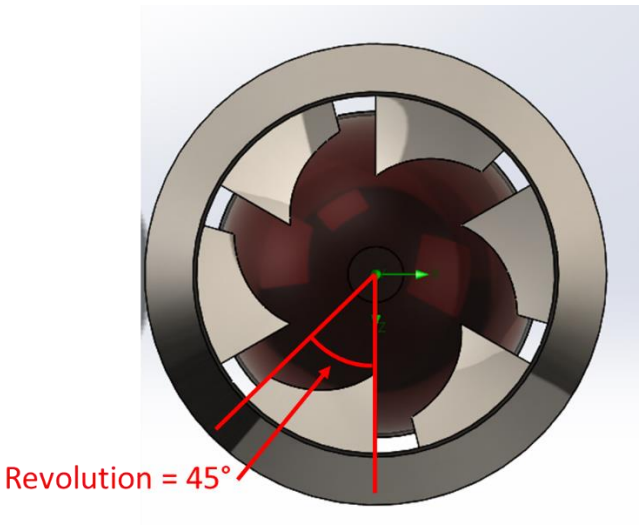

Figure 6.29. SolidWorks Parameters that Define Impeller Blades Top View

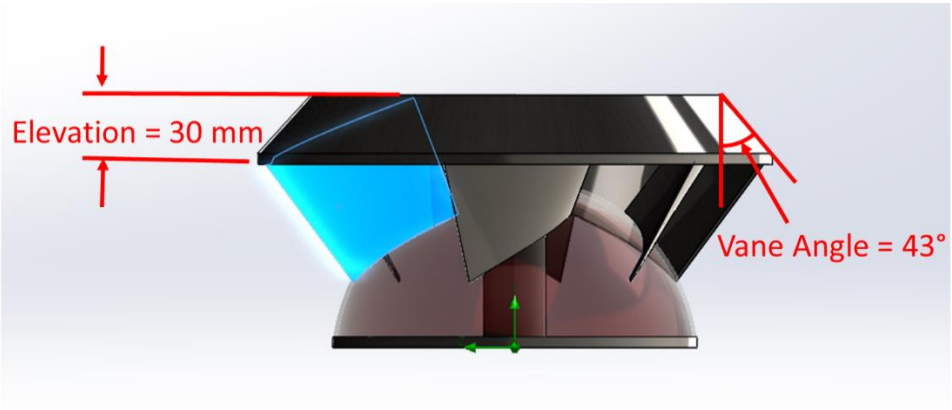

Figure 6.30. SolidWorks Parameters that Define Impeller Blades Side View

The study adopts impeller sample No. 3 as a standard to represent products from industry. Any changes of the above four design parameters are performed on this model. By specifying the grid size to be the same level as previously shown in Section 6.3.1 for all simulations in the optimization process, this study automatically validates the grid independence based on earlier analysis.

On the one hand, the design of experiments investigates the single factor effect of each individual design parameter. The study captures the impeller performance of an individual parameter at various levels. It begins with creating impeller CAD models at 4-9 different levels above and below the standard of each design parameter, with a difference of 10% of the value of the standard at each level. Then, the study runs these CAD models in SolidWorks Flow Simulation and collects their performance from CFD simulations. This approach allows the researcher to perform a detailed analysis of the behavior with respect to this parameter and thus to find its optimum value at the given operating conditions.

On the other hand, the design of experiments establishes a set of full factorial experiments at two levels to study the interaction between the first three design parameters (Wu and Hamada, 2000). In this study, three parameters – cone height, cone diameter, and overall height – are set to "high" and "low" levels, with the specific values shown in Table 6.14. Following the same procedure as described in the previous paragraph, a total of eight CAD models are tested and analyzed for the behavior of interactions. As the amount of experiments increases exponentially with the number of factors, the last parameter – vane angle – is not included due to computing power limitations.

Table 6.14. Values of Design Parameters at Two-Level Full Factorial Experiments

Design Parameters	Low	High
Cone Height /mm	52.4	58.22
Cone Diameter /mm	126.6	139.3
Overall Height /mm	87.5	96.25

The experiments use two performance parameters, π_1 and η, to evaluate the pump's performance. Performance parameter π_1 is the ratio of flow rate to head. This parameter allows one to compare the pumping capacity of different pumps for given heads. Assuming the pressure remains constant at the inlet and outlet, the pump head is measured by both lift height, H, and flow capacity, Q, based on Bernoulli's Equation (Equation 3.5). Therefore, performance parameter π_1 is a function of H and Q. Recall Equation 3.11, which defines π_1,

$$\pi_1 = \frac{Q}{(gH)^{\frac{1}{2}}D^2} \qquad \textit{Equation 3.11}$$

where g is the gravitational constant and D is the diameter of the pipe (Aban and International Rice Research Institute, 1985). According to the its definition, π_1 quantifies both lift height and flow capacity of the impeller's performance.

Performance parameter η quantifies the mechanical efficiency of the impeller, which may be defined as the ratio between water power and brake power as shown in Equations 6.30 – 6.32 (Lam, et al., 2015),

$$\eta = \frac{w.p}{b.p} \qquad \textit{Equation 6.30}$$

$$w.p = \rho * Q * \frac{v^2}{2} \qquad \textit{Equation 6.31}$$

$$b.p = T * N \qquad \textit{Equation 6.32}$$

where ρ is water density, v is the average flow velocity at the outlet, T is the torque on the shaft at axial direction, and N is the rotational speed. Both parameters are essential in evaluating the overall effectiveness of the impeller design.

6.5.2 Single Factor Optimization

The analysis begins with single factor optimization, the results of which are included in Tables J1-J4 in Appendix J. For each design parameter, the analysis attempts to model the experimental data with a general linear model or a multiple regression model, in order to observe the behavior of π_1 and η. The results are highlighted in Figures 6.31 to 6.34 below.

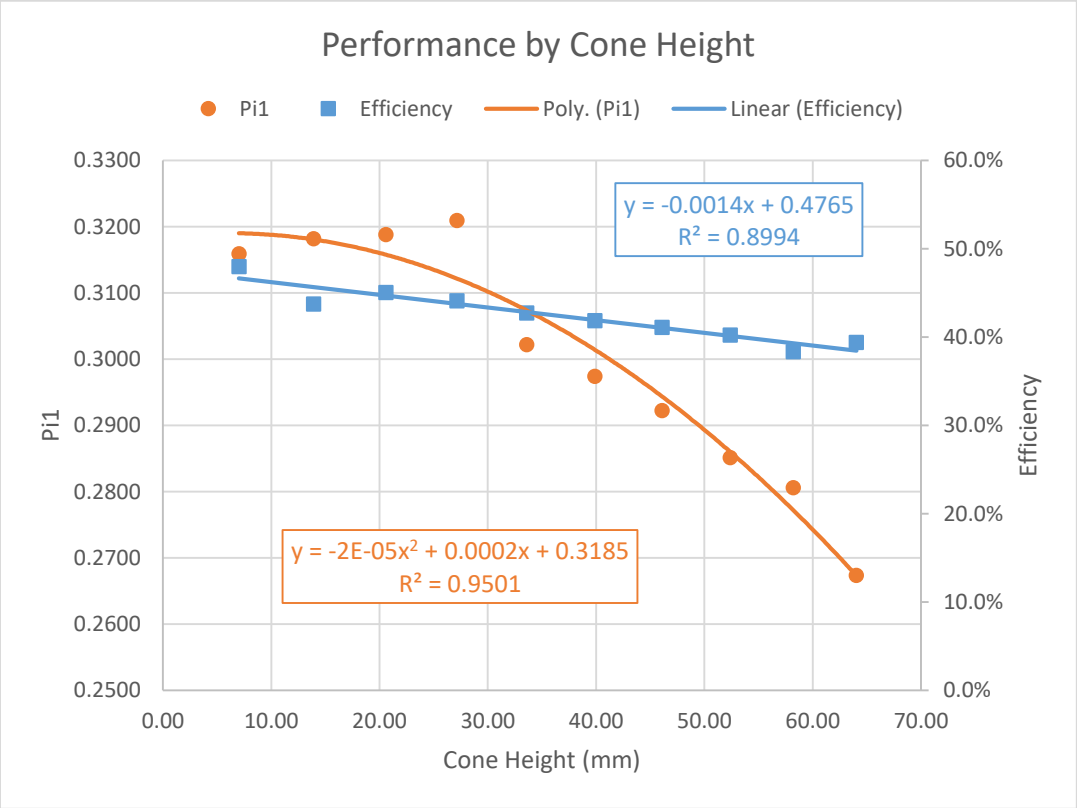

Figure 6.31. Single Factor Optimization - Cone Height

Figure 6.31 demonstrates the behavior of π_1 and efficiency with respect to the cone height. The behavior of π_1 versus Cone Diameter is colored in orange. From the experimental data, π_1 slowly increases with an increase in cone height before it reaches its maximum at a cone height of 27 mm. After that, π_1 sharply decreases with the cone

height. This trend can be fit by a second-order polynomial, $y = -2 * 10^{-5}x^2 + 0.0002x + 0.3185$, as shown in the figure with an R-squared value of 0.95. A first-order is not fit because it failed to capture the vertex phenomenon at this range. Note that the vertex from the fit parabola is shown at a cone height of 8 mm, thus the optimum cone height for a maximum π_1 may be estimated between 8 mm and 27 mm.

Figure 6.31 also demonstrates the relationship between efficiency and the cone height in blue. From the experimental data, the efficiency displays a decreasing relationship against an increasing cone height. This relationship is best qualified by a linear model, $y = -0.0014x + 0.4765$. The R-squared value of the linear fit is limited to 0.8994 due to several outliers. In this case, a linear fit is used instead of a second-order polynomial because the R-Squared value for the second-order fit is 0.9014, which is an insignificant increase.

Based on this analysis, cone height has an optimum value between 15 mm, the curve fit maximum, and 27 mm, at the highest π_1, and should be minimized for the best efficiency.

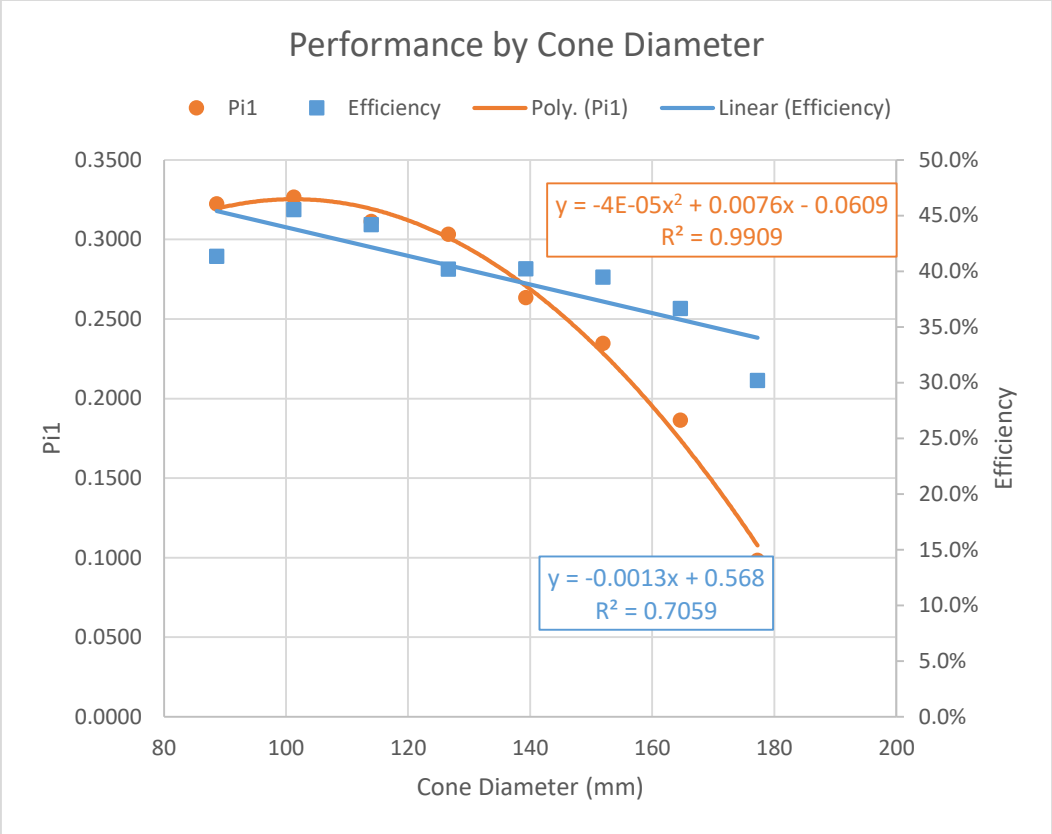

Figure 6.32. Single Factor Optimization – Cone Diameter

Similarly, Figure 6.32 shows the behavior of π_1 and efficiency with respect to the cone diameter. The behavior of π_1 is colored in orange. In terms of pumping capacity and head, the data reaches a maximum π_1 at the cone diameter of 101 mm. After that, the data decays parabolically. The behavior of $\pi_1$versus Cone Diameter is best fit by a second-order polynomial, $y = -4 * 10^{-5}x^2 + 0.0076x - 0.0609$, with an R-squared value of 0.9909. This indicates a high consistency between the data and the trend line.

The behavior of efficiency is colored in blue. In terms of efficiency, the data are best fit by a linear regression, $y = -0.0013x + 0.568$, with an R-squared value of 0.7059. Although the R-Squared value is not ideal, this is the only reasonable fit in this circumstance.

Based on this analysis, cone diameter has an optimum value of 101 mm for the highest π_1, and should be minimized for the best efficiency.

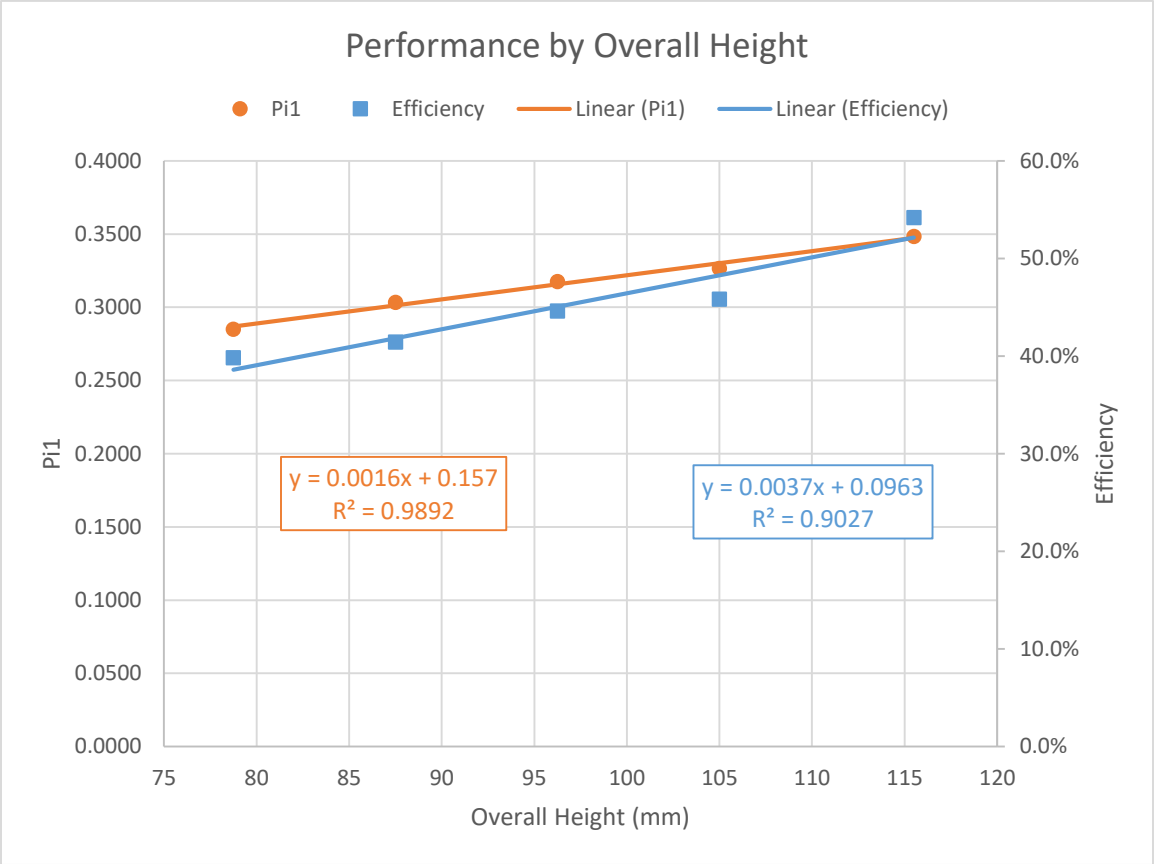

Figure 6.33. Single Factor Optimization - Overall Height

Figure 6.33 gives the behavior of π_1 and efficiency with respect to the overall height. The behavior of π_1 is colored in orange, and the behavior of efficiency is colored in blue. In this case, both π_1 and efficiency increase steadily with the increase in overall height. Thus, both performance variables are modeled using a linear model. π_1 versus Overall Height can be modeled by $y = 0.0016x + 0.157$, with an R-squared value of 0.9892. Efficiency versus Overall Height can be modeled by $y = 0.0037x + 0.0963$, with an R-squared value of 0.9027. This linear increase in π_1 may be due to the uniform

scaling of the impeller in the axial direction. Because of this scaling, the geometric shape of the impeller is retained in the other two directions. This allows a linear increase in the area of contact between impeller and water, without significantly affecting other factors. Thus, by operating at the same conditions, the pump performance is expected to be directly proportional to the area of contact or the uniform scaling in the axial direction. That being said, the reason of a linear increase in efficiency nevertheless is yet to be determined.

Based on this analysis, the impeller should be scaled up in axial direction as much as possible for greater π_1 and higher efficiency.

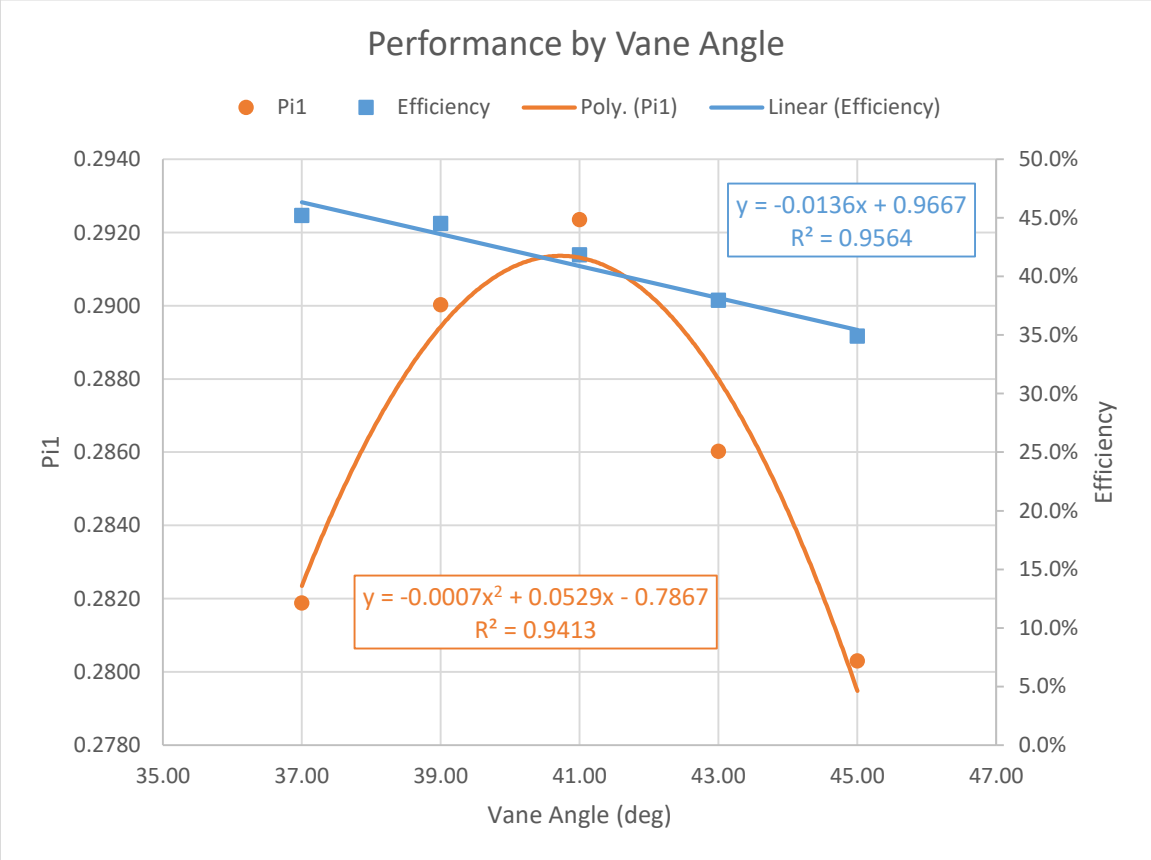

Figure 6.34. Single Factor Optimization – Vane Angle

Figure 6.34 presents the behavior of π_1 and efficiency with respect to the vane angle. The behavior of π_1 is colored in orange. In terms of π_1, the data reach a maximum π_1 at the vane angle of 41 degrees. The data decay before and after the vertex is roughly in the shape of a parabola. Thus, the behavior of π_1 versus Cone Diameter is best fit by a quadratic function, $y = -0.0007x^2 + 0.0529x - 0.7867$, with an R-Squared value of 0.9413. From the qualitative observation in Figure 6.34, the trend line aligns well with the experimental data.

The behavior of efficiency is colored in blue. In terms of efficiency, the data decreases against vane angle, approximately in a linear relationship. Thus, this relationship is fit by a linear model in the form $y = 0.0136x + 0.9667$. The correctness of this fit is supported by an R-Squared value of 0.9564.

Based on this analysis, vane angle has an optimum value of 41 degrees for the highest π_1, and should be minimized for the best efficiency.

This subsection investigates the behavior of each design parameter by itself based on the geometric model of sample impeller No. 3. Comparisons across different design parameters, nevertheless, are not yet included. These comparisons along with the effect of two-way interaction are covered in the Section 6.5.3.

6.5.3 Two-way Interaction and ANOVA

In this section, a set of full factorial experiments at two levels is conducted to study the significance of main effects and two-way interaction effects of the design parameters. The experiments are conducted based on CFD simulations following the

procedures as described in Section 6.5.1. Due to the time-consuming process of testing each case, the fourth design parameter – vane angle – is not included.

The experiments contain a single replicate because the results are generated by computers (Wu and Hamada, 2000). Each of the three design parameter are set to two levels – High and Low – as shown below in Table 6.15. By abbreviating the three design parameters Cone Height, Cone Diameter, Overall Height as letters "A", "B", "C", respectively, and their High and Low values as "+" and "–" signs, a model matrix can be created as shown in Table 6.15 below. The results associated with these cases are included in Table J5 in Appendix J and highlighted in Table 6.16.

Table 6.15. Model Matrix for Full Factorial Experiments at Two-Levels

Case No.	A	B	C	AB	AC	BC
1	–	–	–	+	+	–
2	–	–	+	+	–	+
3	–	+	–	–	–	+
4	–	+	+	–	+	–
5	+	–	–	–	+	–
6	+	–	+	–	–	+
7	+	+	–	+	–	+
8	+	+	+	+	+	–

Table 6.16. Result Highlights for 2^3 Experiments

Case No.	A	B	C	π_1	Efficiency η
1	–	–	–	0.2851	40.2%
2	–	–	+	0.3073	41.1%
3	–	+	–	0.2588	39.3%
4	–	+	+	0.2619	39.3%
5	+	–	–	0.2806	38.3%
6	+	–	+	0.3177	44.6%

7	+	+	–	0.2635	40.2%
8	+	+	+	0.2659	39.9%

Once the results are collected, ANOVA is performed via Matlab using the code included in Appendix J for π_1 and efficiency, η. In this case, the null hypothesis assumes that π_1/η is independent of each design parameter, and the alternative hypothesis is that π_1/η is affected by these design parameters. The analysis is performed at a confidence interval of 90%, or $\alpha = 0.10$. Depending on the effect of interaction terms, a Type II or Type III sum of square is calculated. This section includes a summary of the ANOVA results calculated via Matlab.

Analysis of Variance

Source	Sum Sq.	d.f.	Mean Sq.	F	Prob>F
Cone Height	0.00003	1	0.00003	0.88	0.5211
Cone Diameter	0.00247	1	0.00247	81.23	0.0703
Overall Height	0.00052	1	0.00052	17.25	0.1504
Cone Height*Cone Diameter	0	1	0	0.03	0.8869
Cone Height*Overall Height	0.00003	1	0.00003	0.83	0.5299
Cone Diameter*Overall Height	0.00036	1	0.00036	11.89	0.1797
Error	0.00003	1	0.00003		
Total	0.00344	7			

Hierarchical (Type II) sums of squares.

Figure 6.35. ANOVA Results of π_1

Figure 6.35 shows the ANOVA with respect to π_1. Note that the column labeled "Prob>F" gives the p-value associated with each term. In this case, the main effect of cone diameter has a p-value 0.0703, which is less than $\alpha = 0.10$. Thus, the main effect of cone diameter is the only significant effect with respect to π_1 at a confidence interval of 90%. At some lower confidence intervals, such as 80%, the main effect of the overall height and interactions between cone diameter and overall height, with p-values of 0.1504 and 0.1797, may also become significant. π_1 is independent to all other design parameter and interactions. Because interactions are not significant, the Type II sum of squares is used for calculation.

Analysis of Variance

Source	Sum Sq.	d.f.	Mean Sq.	F	Prob>F
Cone Height	1.2012	1	1.20125	0.3	0.6829
Cone Diameter	3.7812	1	3.78125	0.93	0.5114
Overall Height	5.9513	1	5.95125	1.47	0.4396
Cone Height*Cone Diameter	0.0013	1	0.00125	0	0.9888
Cone Height*Overall Height	3.2513	1	3.25125	0.8	0.5353
Cone Diameter*Overall Height	7.0312	1	7.03125	1.73	0.4137
Error	4.0613	1	4.06125		
Total	25.2787	7			

Hierarchical (Type II) sums of squares.

Figure 6.36. ANOVA Results of Efficiency

Figure 6.36 shows the ANOVA with respect to efficiency. Similarly, the column labeled "Prob>F" represents the p-value. In this case, none of the effects has a p-value less than $\alpha = 0.10$. Thus, there is not enough evidence to reject the null hypothesis. In other words, all design parameters as well as their interactions at the confidence interval of 90% do not have significant effect on the mechanical efficiency of the impeller. Because interactions are once again insignificant, Type II sum of square is used for efficiency calculations.

Table 6.17. Manufacturing Tolerances for 5% Change in Performance

	Cone Height (mm)	Cone Diameter (mm)
For highest π_1	17±10	101±13
For most Efficiency	7–20	88–101

Based on the single factor optimization and ANOVA results, a tolerance analysis is performed, with results highlighted in Table 6.17. When optimizing for pumping capacity and head, the manufacturer should keep the cone height at 17±10 mm and the cone diameter at 101±13 mm in order to limit the variation of $\pi_1$to within 5%; when optimizing for the most efficiency, the manufacturer should keep the cone height at 7–20 mm and the cone diameter at 88 – 101 mm to limit the variation of the impeller's efficiency to within 5%. Because the overall height has an insignificant effect on π_1 and efficiency according to the ANOVA results, the tolerance for the overall height is not specified.

6.5.4 Section Summary

Section 6.5 offers potential design optimization to current impeller products represented by Sample No. 3 through CFD simulation. Subsection 6.5.1 introduces the process of conducting experiments, as well as two dimensionless terms, π_1 and η, to evaluate the pumping capacity, head, and efficiency of the impellers' performance. From the results presented in Subsection 6.5.2, the manufacturer should set the cone height to 27 mm, the cone diameter to 101 mm and the vane angle to 41 degrees, and maximize overall height for the largest π_1. Similarly, the manufacturer should minimize cone height, cone diameter and vane angle, and maximize overall height for the highest efficiency. If the manufacturer is interested in creating products with the best compromise between pumping capacity and head, then one should prioritize cone height, overall height, and their interaction effects according to the results presented in Section 6.5.3. In the case for the highest efficiency, one may prioritize these factors in the order of overall height, cone diameter, and cone height. Nevertheless, there is no guarantee for a significant improvement in efficiency. Because this optimization method is based on computer-generated results, it requires further physical testing as a validation.

6.6 Chapter Summary

In summary, Chapter 6 presents and analyzes the results generated from physical testing and computer simulations. Section 6.1 focuses on the physical full-scale testing performed in Bangladesh. It validates and analyzes the testing results with different friction losses, operating RPMs, and lift heights. Section 6.1 also uses the above analysis to develop a method of pump selection for the customers. Section 6.2 discusses the prototype testing performed at the Georgia Tech using approximately the same procedure

in the previous section. Although a direct scaling of the results between full-scale and prototypes is impossible due to different apparatus, Section 6.2 supports the full-scale analysis by validating the methods and approaches once again at the prototype scale. Similarly, Sections 6.3 and 6.4 report another two validations using CFD simulations in ANSYS CFX and SolidWorks Flow Simulation, respectively, by comparing the shut-off heads. Finally, after the results are completely examined and validated, a potential design optimization is suggested in Section 6.5 using SolidWorks Flow Simulation only. After several design parameters are identified, Section 6.5 provides an optimum value for each design parameter, as well as the significance of each parameter to the impeller's performance. This completes the analysis of all physical testing and simulation results on the Bangladesh irrigation pump system.

CHAPTER 7

CONCLUSIONS AND FUTURE WORK

This thesis improves the current design of a Thai mixed flow irrigation pump in a cost effective and energy efficient manner. The design and optimization process consists of multiple stages, including design of experiments, sample testing, prototype testing, CFD simulation, and result analysis. The research also incorporates several advanced techniques such as rapid prototyping, reverse engineering, CAD, CFD, and ANOVA during this process. Overall, in support of CIMMYT and BARI, this thesis tests and analyzes the performance of a Thai MFP and suggests a potential optimization for the current design.

Pumps are generally divided into three categories – AFP, MFP, and CP. In the past, irrigation pumps had many different designs in each of these categories. Among these are the initial wood AFP model in 1941, the IRRI AFP model in 1983, the Varchola MFP model in 2012, and the Thai MFP model (TmIP) that was recently studied in 2014. Based on the circumstance in Bangladesh, the research selects the Thai MFP model as the subject of interest.

The study is based upon several fundamental theories. It involves the definition of specific speed, which differentiates the application of AFP, MPF, and CP. It also discusses friction losses and the Affinity Laws, which are incorporated in the analysis with respect to major and minor losses, and to different RPMs. After that, the study proceeds to the physical experiments and simulations.

There are two sets of physical experiments–full-scale testing performed in Bangladesh and prototype testing performed at Georgia Tech. In each set of testing, the pumps' performance in terms of flow rate and pressure are measured with respect to manufacturing capability, lift height, and rotational speed.

The simulations determine the pumps' performance with respect to manufacturing capability and rotational speeds. Simulation includes geometry modeling, mesh generation, problem definition, and solver control. For accuracy and reliability, simulations are performed by both SolidWorks Flow Simulation and ANSYS CFX. In addition to these simulations, design optimization is also performed by SolidWorks Flow Simulation.

Based on experimental results, the research produced several significant outcomes. The experimental results show that geometric differences due to manufacturing have a small effect on the shut-off head. With an average STD of 3.36% in geometry, sample impellers exhibit STDs at all RPMs of less than 3.0% in prototype testing, 4.4% in SolidWorks testing, and 5.6% in CFX testing. The thesis applies friction loss analysis to the pumping systems. For full-scale testing rigs, the loss coefficient was 21.75 with a STD of 1.74. For prototype testing rigs, the loss coefficient was 14.2 with a STD of 3.19. The thesis also applies the Affinity Laws to the pumps' performance at different RPMs. This is supported by R-squared values larger than 0.9 for full-scale testing for flow rate and 0.99 for prototype, SolidWorks, and CFX testing for shut-off head. The thesis then uses the modified Bernoulli's Equation to estimate the flow rate at an arbitrary lift height, of which the mathematical model has an R-squared value over 0.9 for fitting lines at all tested RPMs. After verification of all previous approaches, a method of pump selection is

developed. During these processes, the CFD results demonstrate good agreement with the full-scale testing results. Due to different test rigs, a qualitative rather than a quantitative agreement between full-scale and prototype testing results is observed. Finally, an optimum design is suggested for the highest π_1 and efficiency values, while the significance of each design parameter is ranked based on ANOVA.

In additions to the outcomes presented above, some major drawbacks of this study are also identified. These include the failure to accurately scale between full-scale and prototype results, limited design parameters identified in the stage of reverse engineering and design optimization, the lack of further validation of the optimized design using physical testing, and a limited application of this study on AFP and MFP. In the future, this study may be improved by inserting an additional pressure gauge prior to the control measurement section in full-scale testing. This allows the user to measure the loss coefficients of the control-measurement and pump sections separately, and thus to test different pumps using the same setup. In addition, the optimized design is expected to be physically tested with manufactured samples in order to evaluate its effectiveness. Last but not least, the testing procedure and pump selection method are also expected to be modified in order to facilitate CP testing. Though this study provides a fundamental testing and optimization of current irrigation pumps, more work is required to bring it to completion.

APPENDIX A

MEASREMENT OF FULL-SCALE IMPELLER SAMPLES

A-1. Figures Demonstrating Measured Parameters

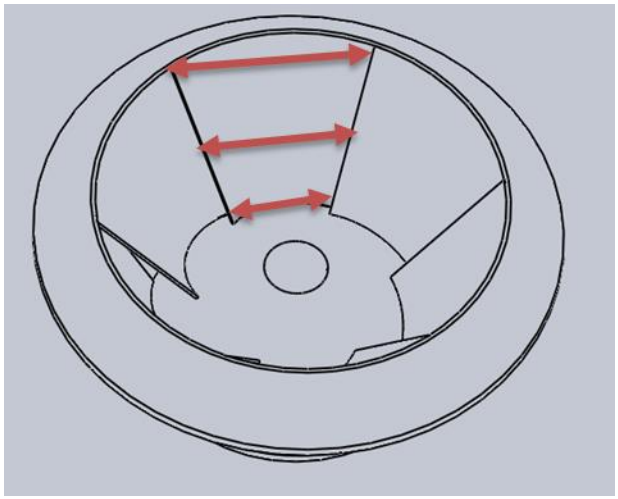

Figure A1. Vane Width Measurement

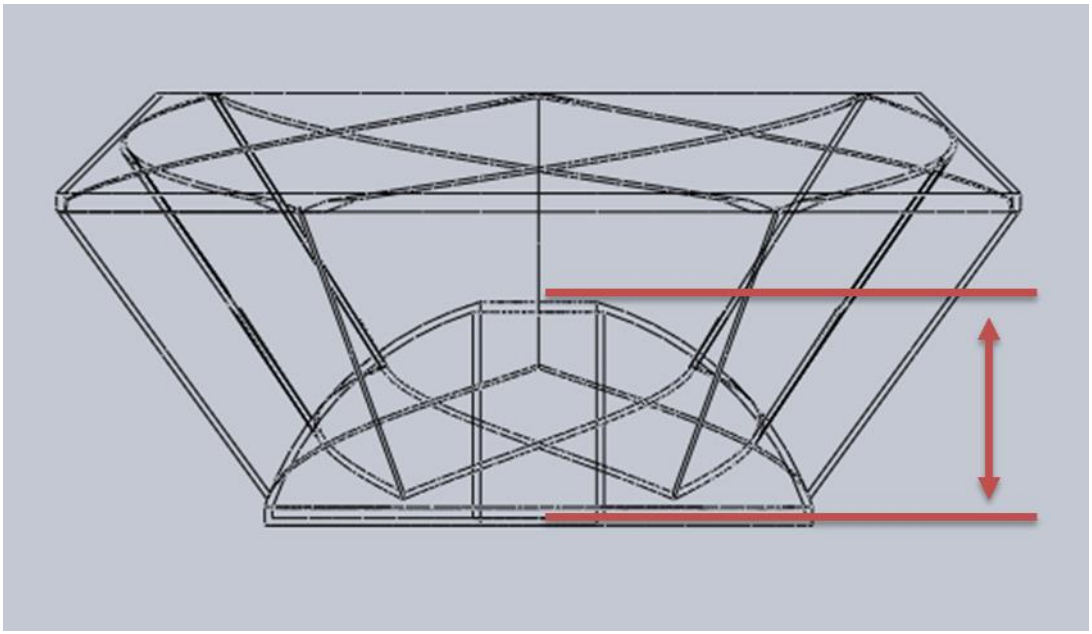

Figure A2. Height of Cone Measurement

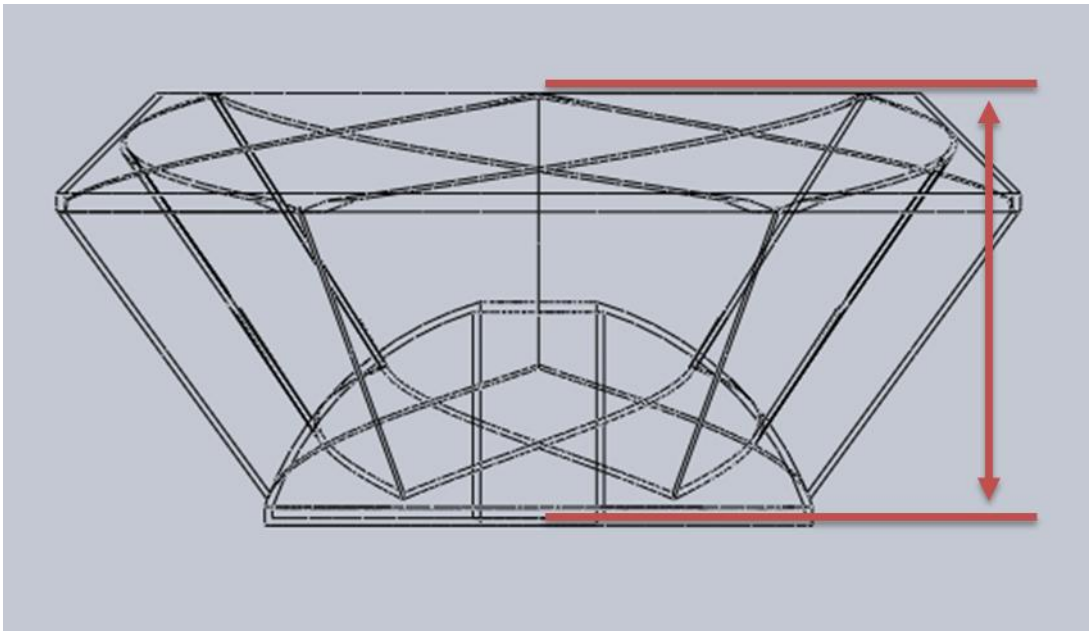

Figure A3. Height of Impeller Measurement

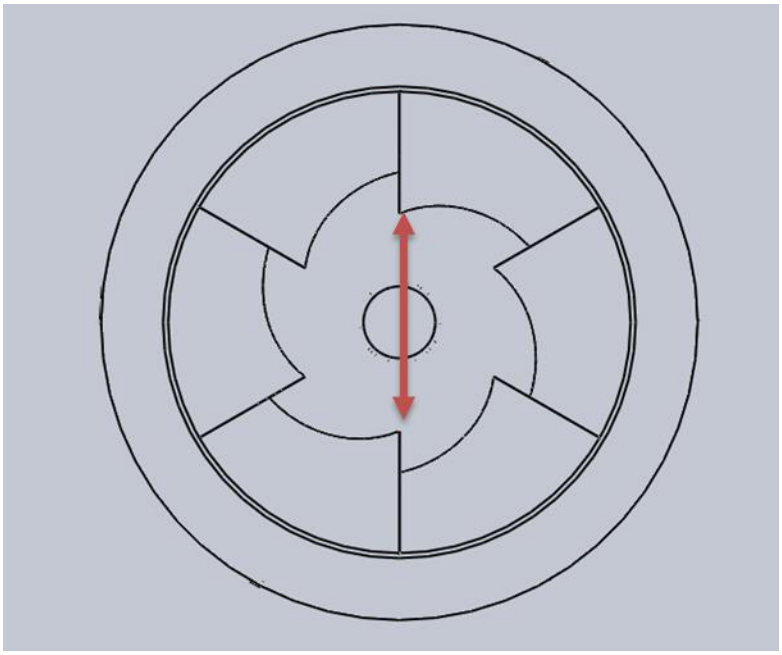

Figure A4. Distance between Tops of Vanes Measurement

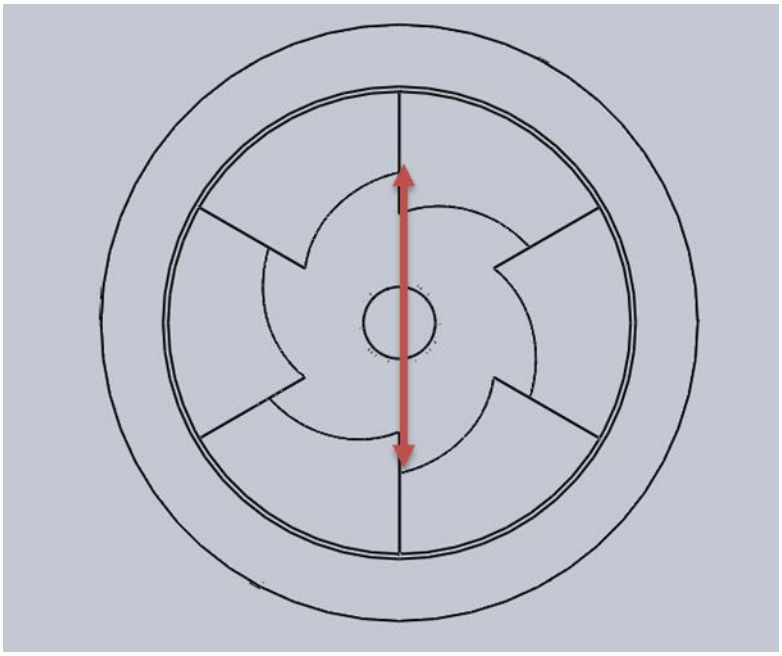

Figure A5. Distance between Edges of Vanes Measurement

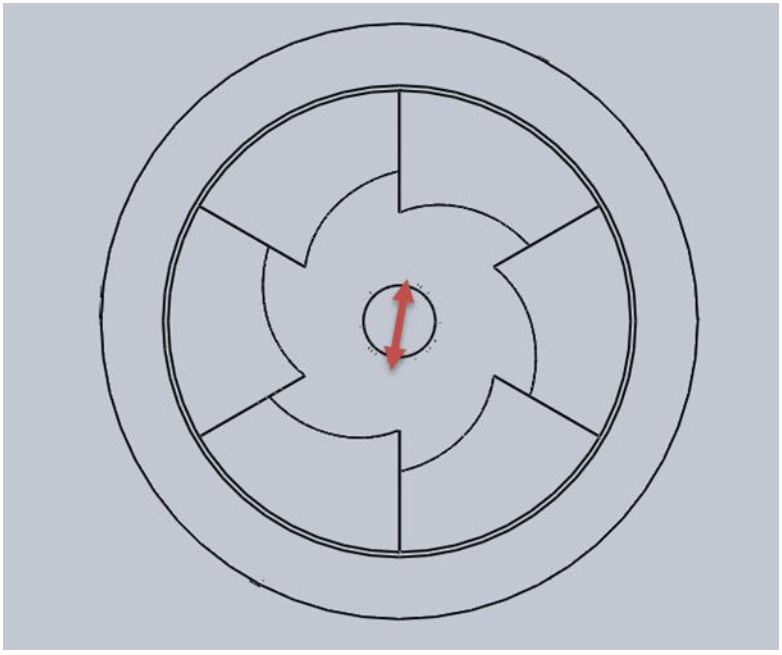

Figure A6. Diameter of Top of Cone (Hole) Measurement

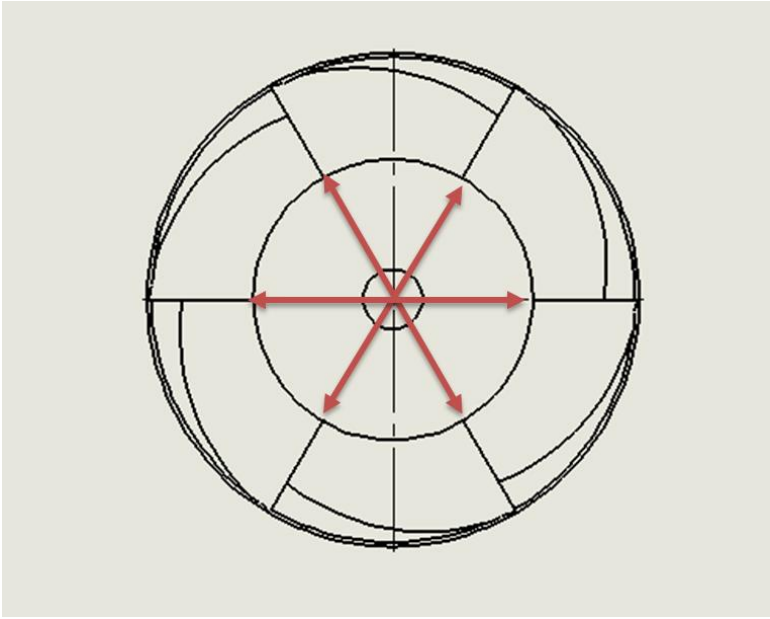

Figure A7. Diameter of Bottom of Cone Measurement

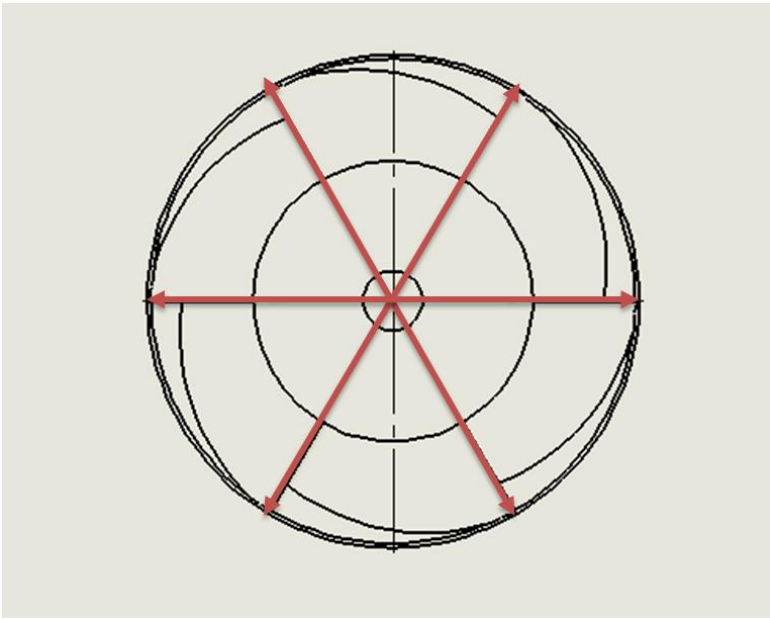

Figure A8. Diameter of Vane Measurement

A-2. Tables of Measured Values

Table A1. Measured Vane Width

Vane	1	2	3	4	5	6	AVG		SDV	
Impeller 1	53.52	53.39	53.70	52.60	52.50	51.30	52.84		0.900	
	55.30	54.50	54.40	55.40	56.10	54.90	55.10	57.99	0.636	5.608
	64.82	64.82	66.64	66.74	65.17	62.92	65.19		1.409	
Impeller 2	48.72	48.19	49.53	49.15	48.80	50.00	49.07		0.641	
	56.00	55.80	56.07	56.10	55.40	55.00	55.73	56.49	0.441	6.388
	64.82	65.29	64.00	64.21	60.61	65.29	64.04		1.762	
Impeller 3	53.00	52.21	49.42	50.68	45.22	49.59	50.02		2.746	
	55.40	56.26	54.38	55.44	55.71	55.92	55.52	57.15	0.643	6.618
	64.15	65.12	63.98	65.73	66.75	64.90	65.11		1.031	
Impeller 4	50.80	53.21	51.33	52.10	53.90	51.94	52.21		1.158	
	54.53	55.57	54.45	54.12	55.39	55.54	54.93	56.14	0.639	4.625
	58.30	61.14	63.74	64.34	62.45	63.97	62.32		2.297	
Impeller 5	46.83	51.54	48.06	51.10	47.41	50.61	49.26		2.058	
	55.30	55.16	55.53	55.40	54.90	55.36	55.28	56.96	0.220	7.287
	67.55	64.46	67.57	64.96	65.64	66.35	66.09		1.306	
Impeller 6	49.62	52.00	51.44	51.95	50.34	50.90	51.04		0.942	
	57.05	56.27	55.75	55.17	55.76	56.87	56.15	56.61	0.723	5.260
	60.80	62.64	62.11	64.56	62.82	66.13	63.18		1.889	
AVG	56.47	57.09	56.78	57.21	56.38	57.08	56.84			
SDV	5.962	5.408	6.254	6.048	6.380	6.135			5.905	
							SDV/AVG		10.39%	

Table A2. Measured Height of Cone

		AVG	SDV
Impeller 1	60.0	59.63	0.551
	59.9		
	59.0		
Impeller 2	55.1	55.13	0.058
	55.2		
	55.1		
Impeller 3	58.1	58.17	0.058
	58.2		
	58.2		
Impeller 4	55.1	55.03	0.058
	55.0		
	55.0		
Impeller 5	57.6	57.03	0.493
	56.7		
	56.8		
Impeller 6	56.6	56.50	0.458
	56.9		
	56.0		
AVG		56.92	
SDV			1.700
		SDV/AVG	2.99%

Table A3. Measured Height of Impeller

		AVG	SDV
Impeller 1	92.4	91.37	1.380
	91.9		
	89.8		
Impeller 2	86.7	85.87	0.850
	85.9		
	85.0		
Impeller 3	87.0	87.50	0.624
	87.3		
	88.2		
Impeller 4	88.0	87.77	0.586
	88.2		
	87.1		
Impeller 5	87.5	87.13	0.404
	87.2		
	86.7		
Impeller 6	88.7	88.57	0.321
	88.8		
	88.2		
AVG		88.03	
SDV			1.863
		SDV/AVG	2.12%

Table A4. Measured Distance Between Tops of Vanes

			AVG	SDV
Impeller 1	1_4	59.4	59.97	0.493
	2_5	60.2		
	3_6	60.3		
Impeller 2	1_4	59.7	60.57	2.029
	2_5	62.9		
	3_6	59.2		
Impeller 3	1_4	61.4	62.78	1.457
	2_5	62.7		
	3_6	64.3		
Impeller 4	1_4	61.3	61.54	0.413
	2_5	61.3		
	3_6	62.0		
Impeller 5	1_4	65.1	64.92	0.136
	2_5	64.9		
	3_6	64.8		
Impeller 6	1_4	61.9	61.89	0.761
	2_5	61.1		
	3_6	62.6		
AVG			61.94	
SDV				1.893
			SDV/AVG	3.06%

Table A5. Measured Distance Between Edges of Vanes

			AVG	SDV
Impeller 1	1_4	133.5	133.90	1.058
	2_5	133.1		
	3_6	135.1		
Impeller 2	1_4	128.4	129.38	1.216
	2_5	129.1		
	3_6	130.7		
Impeller 3	1_4	135.2	132.47	3.439
	2_5	128.6		
	3_6	133.7		
Impeller 4	1_4	132.0	133.53	1.990
	2_5	135.8		
	3_6	132.9		
Impeller 5	1_4	128.0	128.35	0.792
	2_5	129.3		
	3_6	127.8		
Impeller 6	1_4	126.1	126.70	3.376
	2_5	123.6		
	3_6	130.3		
AVG			130.72	
SDV				3.386
			SDV/AVG	2.59%

Table A6. Measured Diameter of Top of Cone (Hole)

			AVG	SDV
Impeller 1	1_4	31.8	30.80	0.872
	2_5	30.4		
	3_6	30.2		
Impeller 2	1_4	37.5	37.68	0.235
	2_5	37.9		
	3_6	37.7		
Impeller 3	1_4	32.4	32.45	0.081
	2_5	32.5		
	3_6	32.5		
Impeller 4	1_4	32.2	32.37	0.473
	2_5	32.0		
	3_6	32.9		
Impeller 5	1_4	36.1	36.18	0.240
	2_5	36.5		
	3_6	36.0		
Impeller 6	1_4	37.5	38.01	0.554
	2_5	37.9		
	3_6	38.6		
AVG			34.58	
SDV				2.928
			SDV/AVG	8.47%

Table A7. Measured Diameter of Bottom of Cone

			AVG	SDV
Impeller 1	1_4	127.9	126.97	0.814
	2_5	126.4		
	3_6	126.6		
Impeller 2	1_4	127.4	127.13	0.305
	2_5	126.8		
	3_6	127.1		
Impeller 3	1_4	127.0	126.60	0.371
	2_5	126.2		
	3_6	126.6		
Impeller 4	1_4	125.4	125.15	0.319
	2_5	125.3		
	3_6	124.8		
Impeller 5	1_4	128.2	127.73	0.539
	2_5	127.8		
	3_6	127.2		
Impeller 6	1_4	126.8	126.65	0.161
	2_5	126.6		
	3_6	126.5		
AVG			126.71	
SDV				0.901
			SDV/AVG	0.71%

Table A8. Measured of Outer Diameter

			AVG	SDV
Impeller 1	1_4	182.4	180.97	1.242
	2_5	180.3		
	3_6	180.2		
Impeller 2	1_4	179.8	179.77	0.950
	2_5	178.8		
	3_6	180.7		
Impeller 3	1_4	178.6	178.90	0.985
	2_5	180.0		
	3_6	178.1		
Impeller 4	1_4	181.3	180.85	0.484
	2_5	181.0		
	3_6	180.3		
Impeller 5	1_4	181.9	181.58	0.290
	2_5	181.3		
	3_6	181.5		
Impeller 6	1_4	179.7	180.87	0.999
	2_5	181.5		
	3_6	181.4		
AVG			180.49	
SDV				1.181
			SDV/AVG	0.65%

Table A9. Measured Weight of Impeller

Impeller 1	1.14
Impeller 2	1.10
Impeller 3	1.14
Impeller 4	1.16
Impeller 5	1.10
Impeller 6	1.12
AVG	1.13
SDV	0.024
SDV/AVG	2.15%

APPENDIX B

MAJOR AND MINOR LOSS COEFFICIENT ESTIMATION

Table B1. Associated Parameters in Loss Coefficient Estimation

Inlet Diameter m	0.193	Kinematic Viscosity in m^2/s	1.004E-06
Pipe Diameter m	0.153	Average Water Velocity m/s	2.097
Shaft Diameter m	0.035	Water Density kg/m^3	1000
Pipe Cross Section Area m^2	0.018	Reynolds Number	319490

Table B2. Major Loss Coefficient Estimation

No.	Pipe Material	Pipe Length /m	Pipe Roughness /m	Resource	Relative Roughness ε/D	Re	Friction Factor f	Resource	Major Loss Coefficient K=fL/D
1	GI Pipe with Inner Shaft	6	1.50E-04	Engineering Toolbox	0.000980	319490	0.024	Moody Chart from A-24	0.94
2	Flexible Pipe	3.72	0.015	Estimate	0.098039	319490	0.1	Moody Chart from A-24	2.43
3	Worn Cast Iron	1.228	0.001	Engineering Toolbox	0.006536	319490	0.036	Moody Chart from A-24	0.29
								Total Major	3.94

Table B3. Major Loss Coefficient Estimation

No.	Feature	Head loss /bar	D1/D2	Angle /degree	Material	L/D	Friction Factor	Comment	Minor Loss Coeff. K
			(Flow Rate kg/h)	Diameter of Pipe in					
1	Inlet Cage	0.03	100000	6			0.024	Modeled as Foot valves with Strainer with Hinged Disc	2.62
2	Diffuse Vane					45	0.024	Modeled as Butterfly Valves	1.08
3	Protruding Pipe Entrance								0.80
4	Gradual Contraction		0.79	37					0.26
5	Shaft Bearing					45	0.024		1.08
		Beta	C		D	E	F		
6	Wye Flow	1	0.55	40	1	2	1.41		0.32
				Reynolds Number	Drag Coeff. C_D	D			
7	Crossing Shaft			319490	0.0105	0.1834			0.005
8	Pressure Fitting 1							Modeled as Protruding Pipe Entrance	0.80
9	Pressure Fitting 2							Modeled as Sharp Edge Exit	1.00
10	Woltman Flowmeter WPH-150	0.2						Company Product Info Page	1.43
11	Tee Threaded Dividing Line Flow								0.90
12	Ball Valve								0.05
13	Pressure Gauge							Modeled as Plug Valve Straightaway	0.27
14	Butterfly Valve				Cast Iron	45	0.036		1.62
15	Sharp Edged Exit								1.00
								Total Minor	13.24
								Total	17.18

APPENDIX C

EXPERIMENTAL LOSS COEFFICIENT CALCULATION

Table C1. Experimental Loss Coefficient Calculation from Impellers 3 and 4

Impeller No.	RPM	Valve position	Time elapsed	Δvolume	Volumetric Flow Rate	Velocity	Average Velocity	Shut-off Head	Loss Factor
		(%)	(min)	(m^3)	L/s	(m/s)	(m/s)	(m)	
4	1006	Fully open	8	10.2	21.25	1.203	1.230		24.94
		Fully open	8	10.8	22.50	1.273			
		Fully open	8	10.3	21.46	1.214			
		Closed	1	10.43	21.74			2.000	
			1					2.000	
			1					2.000	
	1498	Fully open	8	19.6	40.83	2.311	2.283		21.58
		Fully open	8	19.7	41.04	2.322			
		Fully open	8	18.8	39.17	2.216			
		Closed	1	19.37	40.35			6.000	
			1					6.000	
			1					6.000	
	1748	Fully open	8	23.7	49.38	2.794	2.731		21.88
		Fully open	8	22.9	47.71	2.700			
		Fully open	8	22.9	47.71	2.700			
		Closed	1	23.17	48.26			8.700	
		Closed	1					8.700	
		Closed	1					8.700	
3	1004	Fully open	8	10.6	22.08	1.250	1.230		24.94
		Fully open	8	10.3	21.46	1.214			
		Fully open	8	10.4	21.67	1.226			
		Closed	1	10.43	21.74			2.000	
		Closed	1					2.000	
		Closed	1					2.000	

	1510	Fully open	8	20.2	42.08	2.381	2.389		21.34
		Fully open	8	20.3	42.29	2.393			
		Fully open	8	20.3	42.29	2.393			
		Closed	1	20.27	42.22			6.500	
		Closed	1					6.500	
		Closed	1					6.500	
	1741	Fully open	8	22.9	47.71	2.700	2.715		21.35
		Fully open	8	23.1	48.12	2.723			
		Fully open	8	23.1	48.12	2.723			
		Closed	1	23.03	47.99			8.400	
		Closed	1					8.400	
		Closed	1					8.400	

Table C2. Experimental Loss Coefficient Calculation for BG GI 1

	Valve, % Open	Read Pressure, kg/cm2	TDH, m of H2O	Initial Volume, m3	Final Volume, m3	Time Elapsed, min	Delta Volume, m3	Delta Volume, L	Flow-rate, L/s	Loss Factor
Replication 1										
Engine ID	Changchai S195 Diesel 13.8 HP, 2000 RPM 94351238, 2014									
Pump ID	BG AFP GI 1, Thai MF Impeller									
Engine Sheave	Engine 133 mm 1695 RPM									
Pump Sheave	Pump 127 mm 1740 RPM									
	90	0	0.94	1804	1824.6	8	20.60	20600	42.9	20.6
	50	0.1	1.94	1831.5	1848.7	8	17.20	17200	35.8	
	40	0.2	2.94	1858	1872.3	8	14.30	14300	29.8	
	30	0.34	4.34	1874.5	1884	8	9.50	9500	19.8	
	20	0.51	6.04	1885.5	1889.5	8	4.00	4000	8.3	
	0	0.61	7.04						0.0	
Engine ID	Changchai S195 Diesel 13.8 HP, 2000 RPM 94351238, 2014									
Pump ID	BG AFP GI 1, Thai MF Impeller									
Engine Sheave	133mm 1498 RPM									
Pump Sheave	127 mm 1546 RPM									
	90	0	0.94	1940	1956.9	8	16.90	16900	35.2	23.2
	40	0.1	1.94	1966.5	1979.4	8	12.90	12900	26.9	
	30	0.22	3.14	1982	1992.2	8	10.20	10200	21.3	
	20	0.4	4.94	1998.5	2000.9	8	2.40	2400	5.0	
	0	0.46	5.54						0.0	
Engine ID	Changchai S195 Diesel 13.8 HP, 2000 RPM									

Pump ID Engine Sheave Pump Sheave	94351238, 2014 BG AFP GI 1, Thai Impeller 175 mm 1497 RPM 127 mm 2065 RPM									
	90	0	0.94	2027	2051.2	8	24.20	24200	50.4	20.1
	60	0.05	1.44	2057	2079.4	8	22.40	22400	46.7	
	50	0.14	2.34	2084	2104.3	8	20.30	20300	42.3	
	40	0.22	3.14	2109	2123.3	8	14.30	14300	29.8	
	30	0.48	5.74	2125	2134.2	8	9.20	9200	19.2	
	20	0.74	8.34	2137	2141.4	8	4.40	4400	9.2	
	0	0.82	9.14						0.0	
	Replication 2									
Engine ID Pump ID Engine Sheave Pump Sheave	Changchai S195 Diesel 13.8 HP, 2000 RPM 94351238, 2014 BG AFP GI 1, Thai Impeller Engine 133 mm 1701 RPM Pump 127 mm 1757 RPM									
	90	0	0.94	2893	2913.2	8	20.20	20200	42.1	20.4
	50	0.11	2.04	2920	2937	8	17.00	17000	35.4	
	40	0.22	3.14	2956	2969.2	8	13.20	13200	27.5	
	30	0.34	4.34	2972.5	2979	8	6.50	6500	13.5	
	20	0.52	6.14	2981.5	2983.5	8	2.00	2000	4.2	
	0	0.58	6.74						0.0	
Engine ID Pump ID Engine Sheave Pump	Changchai S195 Diesel 13.8 HP, 2000 RPM 94351238, 2014 BG AFP GI 1, Thai Impeller Engine 174 mm 1498 RPM Pump 127									

Sheave	mm 2059 RPM									
	90	0	0.94	3006	3030.6	8	24.60	24600	51.2	19.9
	70	0.02	1.14	3037	3060.9	8	23.90	23900	49.8	
	60	0.06	1.54	3065	3087.7	8	22.70	22700	47.3	
	50	0.16	2.54	3091	3111.5	8	20.50	20500	42.7	
	40	0.3	3.94	3115	3131.9	8	16.90	16900	35.2	
	30	0.52	6.14	3140.5	3151	8	10.50	10500	21.9	
	20	0.74	8.34	3152.5	3156	8	3.50	3500	7.3	
	0	0.84	9.34						0.0	
Engine ID Pump ID Engine Sheave Pump Sheave	Changchai S195 Diesel 13.8 HP, 2000 RPM 94351238, 2014 BG AFP GI 1, Thai Impeller Engine 133 mm 1504 RPM Pump 127 mm 1553 RPM									
	90	0	0.94	2816.5	2833.9	8	17.40	17400	36.3	20.9
	50	0.06	1.54	2840.5	2855.1	8	14.60	14600	30.4	
	40	0.15	2.44	2857	2869.9	8	12.90	12900	26.9	
	30	0.27	3.64	2871	2878	8	7.00	7000	14.6	
	20	0.38	4.74	2879	2881.1	8	2.10	2100	4.4	

APPENDIX D

PUMP PERFORMANCE AT DIFFERENT LIFT HEIGHTS

Table D1. BG GI 1 Model Lift Height Analysis

	Valve, % Open	Fuel Initial, kg	Flowrate, L/s	Flow velocity (m/s)	Static pressure head (m)	Experi-mental Lift (m)	Theore-tical Lift (m)
	Replication 1						
Engine ID	Changchai S195 Diesel 13.8 HP, 2000 RPM						
	94351238, 2014			All impellers are MF type			
Pump ID	BG AFP GI 1, Thai MF Impeller						
Engine Sheave	Engine 133 mm 1695 RPM						
Pump Sheave	Pump 127 mm 1740 RPM						
	90	3.8	42.9	2.4	0	0.94	0.94
	50	3.61	35.8	2.0	1	0.94	1.94
	40	3.41	29.8	1.6	2	0.94	2.94
	30	3.28	19.8	1.1	3.4	0.94	4.34
	20	3.11	8.3	0.5	5.1	0.94	6.04
	0		0.0		6.1	0.94	7.04
Engine ID	Changchai S195 Diesel 13.8 HP, 2000 RPM						
	94351238, 2014						
Pump ID	BG AFP GI 1, Thai MF Impeller						
Engine Sheave	133mm 1498 RPM						
Pump Sheave	127 mm 1546 RPM						
	90	2.44	35.2	1.9	0.00	0.94	0.94
	40	2.25	26.9	1.5	1.00	0.94	1.94
	30	2.15	21.3	1.2	2.20	0.94	3.14

	20	1.93	5.0	0.3	4.00	0.94	4.94
	0		0.0		4.60	0.94	5.54
Engine ID	Changchai S195 Diesel 13.8 HP, 2000 RPM 94351238, 2014						
Pump ID	BG AFP GI 1, Thai Impeller						
Engine Sheave	175 mm 1497 RPM						
Pump Sheave	127 mm 2065 RPM						
	90	3.44	50.4	2.8	0.00	0.94	1.33
	60	3.2	46.7	2.6	0.50	0.94	1.77
	50	2.98	42.3	2.3	1.40	0.94	2.61
	40	2.75	29.8	1.6	2.20	0.94	3.28
	30	2.58	19.2	1.1	4.80	0.94	5.80
	20	2.38	9.2	0.5	7.40	0.94	8.35
	0		0.0		8.20	0.94	9.14
	Replication 2						
Engine ID	Changchai S195 Diesel 13.8 HP, 2000 RPM 94351238, 2014						
Pump ID	BG AFP GI 1, Thai Impeller						
Engine Sheave	Engine 133 mm 1701 RPM						
Pump Sheave	Pump 127 mm 1757 RPM						
	90	3.61	42.1	2.3	0.00	0.94	1.21
	50	3.42	35.4	1.9	1.10	0.94	2.23
	40	3.11	27.5	1.5	2.20	0.94	3.26
	30	2.95	13.5	0.7	3.40	0.94	4.37
	20	2.78	4.2	0.2	5.20	0.94	6.14
	0		0.0		5.80	0.94	6.74
Engine ID	Changchai S195 Diesel 13.8 HP, 2000 RPM 94351238, 2014						

Pump ID	BG AFP GI 1, Thai Impeller						
Engine Sheave	Engine 174 mm 1498 RPM						
Pump Sheave	Pump 127 mm 2059 RPM						
	90	3.33	51.2	2.8	0.00	0.94	1.34
	70	3.11	49.8	2.7	0.20	0.94	1.52
	60	2.91	47.3	2.6	0.60	0.94	1.88
	50	2.7	42.7	2.3	1.60	0.94	2.82
	40	2.51	35.2	1.9	3.00	0.94	4.13
	30	2.26	21.9	1.2	5.20	0.94	6.21
	20	2.04	7.3	0.4	7.40	0.94	8.35
	0		0.0		8.40	0.94	9.34
Engine ID	Changchai S195 Diesel 13.8 HP, 2000 RPM 94351238, 2014						
Pump ID	BG AFP GI 1, Thai Impeller						
Engine Sheave	Engine 133 mm 1504 RPM						
Pump Sheave	Pump 127 mm 1553 RPM						
	90	2.53	36.3	2.0	0.00	0.94	1.14
	50	2.37	30.4	1.7	0.60	0.94	1.68
	40	2.26	26.9	1.5	1.50	0.94	2.55
	30	2.14	14.6	0.8	2.70	0.94	3.67
	20	2.05	4.4	0.2	3.80	0.94	4.74
	0		0.0		4.40	0.94	5.34

APPENDIX E

BG G1 MODEL EFFICIENCY ANALYSIS

Table E1. BG GI 1 Model Efficiency Analysis

Valve, % Open	Flow-rate, L/s	Fuel Use, L/hr	Water Power, kW	Diesel Power, kW	Fuel Eff, %	Water Deli-very Eff, L water/ diesel	Theo-retical Lift (m)	Expected Flow Rate without Test Rigs (L/s)	Expected Water Power w/o Test Rigs (kW)	Expected Fuel Eff w/o Test Rigs (kW)
Replication 1										
Changchai S195 Diesel 13.8 HP, 2000 RPM 94351238, 2014 BG AFP GI 1, Thai MF Impeller Engine 133 mm 1695 RPM Pump 127 mm 1740 RPM										
90	42.9	1.26	0.40	12.6	3.15%	122423	0.94	62.40	0.575	4.57%
50	35.8	1.35	0.68	13.5	5.06%	95403	1.94	52.10	0.992	7.36%
40	29.8	1.08	0.86	10.8	7.97%	99147	2.94	43.32	1.249	11.58%
30	19.8	1.35	0.84	13.5	6.25%	52693	4.34	28.78	1.225	9.09%
20	8.3	1.44	0.49	14.4	3.43%	20800	6.04	12.12	0.718	4.99%
0	0.0						7.04			
Changchai S195 Diesel 13.8 HP, 2000 RPM 94351238, 2014 BG AFP GI 1, Thai MF Impeller 133mm 1498 RPM 127 mm 1546 RPM										
90	35.2	0.90	0.32	9.0	3.61%	140608	0.94	51.19	0.472	5.25%
40	26.9	0.81	0.51	8.1	6.32%	119253	1.94	39.08	0.744	9.19%
30	21.3	1.62	0.65	16.2	4.05%	47147	3.14	30.90	0.952	5.88%

20	5.0	1.26	0.24	12.6	1.93%	14263	4.94	7.27	0.352	2.80%
0	0.0						5.54			
Changchai S195 Diesel 13.8 HP, 2000 RPM 94351238, 2014 BG AFP GI 1, Thai Impeller 175 mm 1497 RPM 127 mm 2065 RPM										
90	50.4	1.62	0.46	16.2	2.87%	111858	0.94	73.30	0.676	4.18%
60	46.7	1.62	0.66	16.2	4.08%	103538	1.44	67.85	0.959	5.93%
50	42.3	1.62	0.97	16.2	6.00%	93831	2.34	61.49	1.412	8.73%
40	29.8	1.35	0.92	13.5	6.81%	79317	3.14	43.32	1.334	9.90%
30	19.2	1.17	1.08	11.7	9.24%	58880	5.74	27.87	1.569	13.43%
20	9.2	1.26	0.75	12.6	5.96%	26149	8.34	13.33	1.090	8.67%
0	0.0						9.14			
Replication 2										
Changchai S195 Diesel 13.8 HP, 2000 RPM 94351238, 2014 BG AFP GI 1, Thai Impeller Engine 133 mm 1701 RPM Pump 127 mm 1757 RPM										
90	42.1	1.26	0.39	12.6	3.08%	120046	0.94	61.19	0.564	4.48%
50	35.4	1.26	0.71	12.6	5.63%	101029	2.04	51.49	1.031	8.19%
40	27.5	1.26	0.85	12.6	6.73%	78446	3.14	39.98	1.232	9.79%
30	13.5	1.35	0.58	13.5	4.28%	36053	4.34	19.69	0.838	6.22%
20	4.2	1.26	0.25	12.6	1.99%	11886	6.14	6.06	0.365	2.90%
0	0.0						6.74			
Changchai S195 Diesel 13.8 HP, 2000 RPM 94351238, 2014										

BG AFP GI 1, Thai Impeller Engine 174 mm 1498 RPM Pump 127 mm 2059 RPM										
90	51.2	1.62	0.47	16.2	2.92%	113707	0.94	74.52	0.687	4.25%
70	49.8	1.44	0.56	14.4	3.87%	124280	1.14	72.40	0.810	5.63%
60	47.3	1.53	0.71	15.3	4.68%	111096	1.54	68.76	1.039	6.80%
50	42.7	1.35	1.06	13.5	7.89%	113707	2.54	62.10	1.547	11.48%
40	35.2	1.44	1.36	14.4	9.46%	87880	3.94	51.19	1.979	13.76%
30	21.9	1.62	1.32	16.2	8.15%	48533	6.14	31.81	1.916	11.84%
20	7.3	1.53	0.60	15.3	3.90%	17129	8.34	10.60	0.867	5.68%
0	0.0						9.34			
Changchai S195 Diesel 13.8 HP, 2000 RPM 94351238, 2014 BG AFP GI 1, Thai Impeller Engine 133 mm 1504 RPM Pump 127 mm 1553 RPM										
90	36.3	0.99	0.33	9.9	3.38%	131607	0.94	52.71	0.486	4.92%
50	30.4	0.72	0.46	7.2	6.39%	151840	1.54	44.23	0.668	9.29%
40	26.9	0.99	0.64	9.9	6.51%	97571	2.44	39.08	0.935	9.46%
30	14.6	0.72	0.52	7.2	7.24%	72800	3.64	21.20	0.757	10.53%
20	4.4	0.99	0.20	9.9	2.06%	15884	4.74	6.36	0.296	2.99%
0	0.0						5.34			

APPENDIX F

PROTOTYPE GEOMETRIC VARIATION STUDY

Table F1. Prototype Measurements

Impeller	Parameters	Expected	Measured			AVE	STD	% Diff.
1	Height	1.435	1.448	1.467	1.453	1.456	0.010	1.4%
	Hub Diameter	1.994	1.993	1.991	1.995	1.993	0.002	0.1%
2	Height	1.374	1.390	1.386	1.394	1.390	0.004	1.1%
	Hub Diameter	2.035	2.031	2.032	2.034	2.032	0.002	0.1%
3	Height	1.390	1.407	1.407	1.417	1.410	0.006	1.4%
	Hub Diameter	2.012	2.007	2.011	2.014	2.011	0.004	0.0%
4	Height	1.380	1.383	1.385	1.397	1.388	0.007	0.6%
	Hub Diameter	1.967	1.965	1.964	1.967	1.965	0.002	0.1%
5	Height	1.364	1.373	1.380	1.377	1.377	0.003	0.9%
	Hub Diameter	2.000	2.002	1.998	2.000	2.000	0.002	0.0%
6	Height	1.392	1.405	1.423	1.414	1.414	0.009	1.6%
	Hub Diameter	1.990	1.988	1.992	1.994	1.991	0.003	0.0%
						Overall Height		1.2%
						Overall Hub Diameter		0.1%

Table F2. Prototype Testing Results

		Open Valve					Closed Valve	Open Valve		Closed Valve	
RPM	Impellers		Open Head (/cm)	Delta Vol. (/L)	Test Time (/s)	Flow Rate (L/s)	Shut-Off Head (/cm)	Flow Rate AVE (L/s)	Flow Rate STD (L/s)	Shut-Off Head AVE (/cm)	Shut-Off Head STD (/cm)
1744	No. 1	1	71.0	20	24.68	0.81	85.5	0.93	0.07	85.2	2.23
		2	70.5	20	19.68	1.02	84.0				
		3	71.0	20	22.81	0.88	85.5				
	No. 2	1	76.0	20	21.47	0.93	89.0				
		2	72.0	20	19.43	1.03	90.0				
		3	74.0	20	23.00	0.87	90.0				
	No. 3	1	69.0	20	22.08	0.91	84.5				
		2	66.0	20	19.56	1.02	83.0				
		3	68.5	20	19.40	1.03	83.0				
	No. 4	1	71.0	20	24.18	0.83	83.5				
		2	72.0	20	23.77	0.84	83.0				
		3	71.0	20	22.28	0.90	84.0				
	No. 5	1	69.5	20	22.53	0.89	84.0				
		2	69.5	20	21.87	0.91	85.0				
		3	69.5	20	21.30	0.94	84.5				
	No. 6	1	70.0	20	21.75	0.92	85.0				
		2	71.0	20	20.06	1.00	86.0				
		3	71.0	20	19.76	1.01	84.5				
							STD/AVE		7.8%		2.6%
1500	No. 1	1	56.0	7.5	8.93	0.84	66.0	0.71	0.08	65.7	1.56
		2	55.5	7.5	12.46	0.60	64.5				
		3	56.8	7.5	12.51	0.60	64.0				
	No. 2	1	56.0	7.5	10.18	0.74	68.5				
		2	54.5	7.5	10.13	0.74	69.0				
		3	56.0	7.5	9.63	0.78	69.0				
	No. 3	1	55.0	7.5	9.66	0.78	65.0				
		2	55.5	7.5	11.31	0.66	65.5				
		3	56.0	7.5	8.80	0.85	66.0				
	No. 4	1	56.0	7.5	10.34	0.73	66.5				
		2	54.0	7.5	11.06	0.68	65.0				
		3	53.0	7.5	11.11	0.68	64.0				
	No. 5	1	55.5	7.5	11.98	0.63	65.0				

		2	56.0	7.5	11.76	0.64	65.0				
		3	54.5	7.5	12.21	0.61	65.0				
	No. 6	1	55.0	7.5	9.65	0.78	65.0				
		2	55.0	7.5	9.91	0.76	65.0				
		3	56.0	7.5	10.01	0.75	65.0				
							STD/AVE	11.1%		2.4%	
1000	No. 1	1	30.5	7.5	32.52	0.23	32.5	0.29	0.04	33.4	1.01
		2	30.5	7.5	35.73	0.21	32.5				
		3	30.5	7.5	33.90	0.22	32.5				
	No. 2	1	30.5	7.5	28.13	0.27	35.0				
		2	30.5	7.5	26.21	0.29	35.5				
		3	30.0	7.5	30.58	0.25	35.0				
	No. 3	1	32.0	7.5	26.76	0.28	34.0				
		2	30.5	7.5	22.80	0.33	33.5				
		3	30.0	7.5	25.78	0.29	34.0				
	No. 4	1	31.0	7.5	26.26	0.29	32.5				
		2	30.0	7.5	23.06	0.33	33.0				
		3	30.0	7.5	26.28	0.29	32.5				
	No. 5	1	30.5	7.5	26.25	0.29	33.0				
		2	30.0	7.5	25.85	0.29	32.0				
		3	30.5	7.5	25.80	0.29	32.5				
	No. 6	1	31.0	7.5	21.63	0.35	33.5				
		2	30.0	7.5	23.16	0.32	33.5				
		3	31.0	7.5	21.06	0.36	33.5				
							STD/AVE	14.3%		3.0%	

APPENDIX G

PROTOTYPE FRICTION LOSS ANALYSIS

Table G1. Major Loss Parameters

	Pipe Material	Pipe Length (m)	Pipe Diameter (m)	Pipe Roughness ε (m)	Relative Roughness ε / D
1	PVC (3 inch)	0.16	0.06985	4.50E-06	6.44E-05
2	PVC (2 inch)	0.5225	0.0508	4.50E-06	8.86E-05

Table G2. Minor Loss Estimation

	Feature	Resistance	Resource
1	Open (Ball) Valve	0.1	The Engineering Toolbox
2	Inlet (Protruding)	0.8	FE Handbook Version 9.3 (NCEES, 2013)
3&4	Bend 1+Hole (Modeled as Dividing T (Flanged))	1.0	The Engineering Toolbox
5	Bend 2	0.3	The Engineering Toolbox
6	Contraction 1 (3in -> 2in), Assumed Re<2500	1.5	Crane Co. Engineering Division
7	Exit	1.0	FE Handbook Version 9.3 (NCEES, 2013)
8	Manometer (T-Line Flow)	0.2	Crane Co. Engineering Division
10	Inlet Fitting (Expansion)	1.0	FE Handbook Version 9.3 - Modeled as Sharp Exit (NCEES, 2013)
11	Bend 1 Inlet (Expansion + Contraction)	1.5	FE Handbook Version 9.3 - Modeled as Sharp Exit and Entrance (NCEES, 2013)
12	Bend 1 Outlet (Expansion + Contraction)	1.5	FE Handbook Version 9.3 - Modeled as Sharp Exit and Entrance (NCEES, 2013)
13	Valve Inlet (Expansion)	1.0	FE Handbook Version 9.3 - Modeled as Sharp Exit (NCEES, 2013)
14	O-Ring 1 (Contraction)	0.5	FE Handbook Version 9.3 - Modeled as Sharp Entrance (NCEES, 2013)
15	O-Ring 2 (Expansion)	1.0	FE Handbook Version 9.3 - Modeled as Sharp Exit (NCEES, 2013)
16	Valve Outlet (Contraction)	0.5	FE Handbook Version 9.3 - Modeled as Sharp Entrance (NCEES, 2013)
17	Bend 2 Inlet (Expansion + Contraction)	1.5	FE Handbook Version 9.3 - Modeled as Sharp Exit and Entrance (NCEES, 2013)
	Total Minor Loss	13.3	

Table G3. Major Loss Calculation

		Major Losses								
		Entrance (3 in)				Pipes (2 in)				
Impeller	RPM	velocity (m/s)	Re	Friction Factor	Resistance Coefficient K=fL/D	velocity (m/s)	Re	Friction Factor	Resistance Coeffiecent K=fL/D	Total Major Loss Coefficient
Impeller 1	1744	0.211	14743	0.028	0.064	0.400	20271	0.026	0.267	0.33
		0.265	18488	0.026	0.061	0.501	25421	0.025	0.253	0.31
		0.229	15951	0.027	0.063	0.433	21933	0.025	0.262	0.32
	1500	0.219	15279	0.028	0.064	0.414	21009	0.026	0.264	0.33
		0.157	10950	0.030	0.069	0.297	15057	0.028	0.287	0.36
		0.156	10907	0.030	0.070	0.296	14997	0.028	0.288	0.36
Impeller 2	1744	0.243	16947	0.027	0.062	0.460	23302	0.025	0.258	0.32
		0.269	18726	0.026	0.060	0.508	25748	0.024	0.252	0.31
		0.227	15819	0.028	0.063	0.429	21752	0.026	0.262	0.33
	1500	0.192	13403	0.029	0.066	0.364	18429	0.027	0.273	0.34
		0.193	13469	0.029	0.066	0.365	18520	0.027	0.273	0.34
		0.203	14168	0.028	0.065	0.384	19482	0.026	0.269	0.33
Impeller 3	1744	0.236	16479	0.027	0.062	0.447	22658	0.025	0.260	0.32
		0.267	18602	0.026	0.061	0.504	25577	0.025	0.252	0.31
		0.269	18755	0.026	0.060	0.509	25788	0.024	0.252	0.31
	1500	0.203	14124	0.028	0.065	0.383	19421	0.026	0.270	0.33
		0.173	12064	0.030	0.068	0.327	16588	0.027	0.280	0.35
		0.222	15505	0.028	0.063	0.421	21319	0.026	0.264	0.33
Impeller 4	1744	0.216	15047	0.028	0.064	0.408	20690	0.026	0.265	0.33
		0.220	15307	0.028	0.064	0.415	21047	0.026	0.264	0.33
		0.234	16331	0.027	0.063	0.443	22455	0.025	0.260	0.32
	1500	0.189	13196	0.029	0.066	0.358	18144	0.027	0.274	0.34
		0.177	12337	0.029	0.067	0.335	16963	0.027	0.279	0.35
		0.176	12281	0.029	0.067	0.333	16886	0.027	0.279	0.35
Impeller 5	1744	0.232	16149	0.027	0.063	0.438	22205	0.025	0.261	0.32
		0.239	16637	0.027	0.062	0.451	22876	0.025	0.259	0.32
		0.245	17082	0.027	0.062	0.463	23488	0.025	0.257	0.32
	1500	0.163	11389	0.030	0.069	0.309	15660	0.028	0.285	0.35
		0.166	11602	0.030	0.068	0.315	15953	0.028	0.283	0.35
		0.160	11175	0.030	0.069	0.303	15365	0.028	0.286	0.35

Impeller 6	1744	0.240	16729	0.027	0.062	0.454	23002	0.025	0.259	0.32
		0.260	18138	0.027	0.061	0.492	24940	0.025	0.254	0.31
		0.264	18413	0.027	0.061	0.499	25318	0.025	0.253	0.31
	1500	0.203	14139	0.028	0.065	0.383	19441	0.026	0.270	0.33
		0.198	13768	0.029	0.065	0.373	18931	0.026	0.271	0.34
		0.196	13631	0.029	0.066	0.370	18742	0.026	0.272	0.34

Table G4. Estimated Loss Coefficient vs. Calculated Loss Coefficient from Experiments

Impeller	RPM	Open Pressure Reading /cm	Average Flow Rate (L/s)	Closed Pressure Reading /cm	Total Major Loss Coefficient	Total Minor Loss Coefficient	Total Estimated Loss Coefficient	Calculated Loss Coefficient from Experiments
Impeller 1	1744	71.0	0.81	85.5	0.33		13.6	16.8
		70.5	1.02	84.0	0.31		13.6	9.5
		71.0	0.88	85.5	0.32		13.6	14.2
	1500	56.0	0.84	66.0	0.33		13.6	10.4
		55.5	0.60	64.5	0.36		13.7	19.0
		56.8	0.60	64.0	0.36		13.7	15.1
Impeller 2	1744	76.0	0.93	89.0	0.32		13.6	11.1
		72.0	1.03	90.0	0.31		13.6	12.7
		74.0	0.87	90.0	0.33		13.6	16.0
	1500	56.0	0.74	68.5	0.34		13.6	17.5
		54.5	0.74	69.0	0.34		13.6	20.3
		56.0	0.78	69.0	0.33		13.6	16.3
Impeller 3	1744	69.0	0.91	84.5	0.32		13.6	14.2
		66.0	1.02	83.0	0.31		13.6	12.1
		68.5	1.03	83.0	0.31		13.6	10.0
	1500	55.0	0.78	65.0	0.33	13.30	13.6	12.4
		55.5	0.66	65.5	0.35		13.7	17.3
		56.0	0.85	66.0	0.33		13.6	10.1
Impeller 4	1744	71.0	0.83	83.5	0.33		13.6	13.7
		72.0	0.84	83.0	0.33		13.6	11.5
		71.0	0.90	84.0	0.32		13.6	12.0
	1500	56.0	0.73	66.5	0.34		13.6	15.1
		54.0	0.68	65.0	0.35		13.6	18.3
		53.0	0.68	64.0	0.35		13.6	18.4
Impeller 5	1744	69.5	0.89	84.0	0.32		13.6	13.8
		69.5	0.91	85.0	0.32		13.6	13.9
		69.5	0.94	84.5	0.32		13.6	12.7
	1500	55.5	0.63	65.0	0.35		13.7	18.5
		56.0	0.64	65.0	0.35		13.7	16.8
		54.5	0.61	65.0	0.35		13.7	21.4
Impeller	1744	70.0	0.92	85.0	0.32		13.6	13.3

6		71.0	1.00	86.0	0.31		13.6	11.1
		71.0	1.01	84.5	0.31		13.6	9.6
	1500	55.0	0.78	65.0	0.33		13.6	12.3
		55.0	0.76	65.0	0.34		13.6	13.1
		56.0	0.75	65.0	0.34		13.6	11.9
						Average	13.6	14.2
						STD	0.014	3.188
						% Diff.	4.2%	

APPENDIX H

SCALING BETWEEN FULL-SCALE AND PROTOTYPE RESULTS

Table H1. Scaling between Full-Scale and Prototype Results of Impellers 3 and 4

		Impeller 3			Impeller 4		
Prototype	Diameter (mm)	72.20			72.20		
	RPM	1744	1500	1000	1744	1500	1000
	Flow Rate (L/s)	0.99	0.76	0.30	0.86	0.69	0.30
	Shut-Off Head (cm)	83.50	65.50	33.83	83.50	65.17	32.67
Full-Scale	Diameter (mm)	178.90			180.85		
	RPM	1741	1510	1004	1748	1498	1006
	Flow Rate (L/s)	47.99	42.22	21.74	48.26	40.35	21.74
	Shut-Off Head (m)	8.40	6.50	2.00	8.70	6.00	2.00
Scaled Up from Prototype	Expected Flow Rate from Prototype (L/s)	14.98	11.70	4.58	13.47	10.87	4.72
	Expected Head from Prototype (m)	5.11	4.08	2.09	5.26	4.08	2.07

APPENDIX I

ANSYS CFX SIMULATION

Table I1. CFX Grid Independence Study

	Grid size analysis		
RPM	1500	1500	1500
Residual	0.0001	0.0001	0.0001
Max size (m)	0.01579	0.005	0.004
Nodes	56128	113260	202640
Grid Elements	297276	627475	1137699
Inlet Pressure (Pa)	54	20	20
Outlet Pressure (Pa)	44642	40607	43834
Max Pressure (Pa)	62910	62130	66630
Inlet Head (m)	0.01	0.00	0.00
Outlet Head (m)	4.56	4.14	4.47
Max Head (m)	6.42	6.34	6.80
Ave Δ Head (m)	4.55	4.14	4.47
Max Δ Head (m)	6.41	6.34	6.80

APPENDIX J

DESIGN OPTIMIZATION

J-1. Tables of Factor Optimization

Table J1. Single Factor Optimization – Cone Height

Cone Height /mm	64.04	58.22	52.40	46.10	39.90	33.59	27.15	20.60	13.90	7.02
Shut-Off Pressure /kpa	186	186	186	182	185	182	179	181	180	181
Shut-Off Head /m	8.59	8.63	8.65	8.19	8.51	8.18	7.90	8.10	8.08	8.08
Flow Rate /$m^3\ s^{-1}$	0.0785	0.0826	0.0840	0.0838	0.0869	0.0866	0.0904	0.0909	0.0906	0.0900
Velocity /$m\ s^{-1}$	7.72	7.651	7.78	7.73	7.82	7.79	7.93	7.89	7.758	8.221
π_1	0.2673	0.2806	0.2851	0.2922	0.2974	0.3022	0.3209	0.3188	0.3182	0.3159
Y-Axis Torque /Nm	32.52	34.54	34.63	33.36	34.74	33.66	35.25	34.38	34.14	34.70
Water Power	2338	2418	2545	2503	2656	2627	2840	2829	2726	3041
Shaft Power	5938	6308	6325	6093	6345	6148	6438	6278	6235	6337
Efficiency	39.4%	38.3%	40.2%	41.1%	41.9%	42.7%	44.1%	45.1%	43.7%	48.0%

Table J2. Single Factor Optimization – Cone Diameter

Cone Diameter /mm	88.62	101.28	113.94	126.60	139.26	151.92	164.58	177.24
Shut-Off Pressure /Pa	175243	178994	184400	185927	203634	211165	226593	231534
Shut-Off Head /m	7.54	7.93	8.48	8.63	10.44	11.21	12.78	13.29
Flow Rate /m^3s^{-1}	0.0887	0.0921	0.0908	0.0893	0.0853	0.0787	0.0668	0.0359
Velocity /m s^{-1}	7.829	7.866	7.789	7.651	7.601	7.510	7.100	5.520
π_1	0.3224	0.3265	0.3113	0.3033	0.2635	0.2346	0.1865	0.0983
Y-Axis Torque /Nm	36.01	34.26	34.13	35.60	33.54	30.79	25.15	9.92
Water Power 2	2718	2849	2754	2614	2464	2219	1684	547
Shaft Power	6576	6257	6232	6502	6125	5623	4593	1812
Efficiency η	41.3%	45.5%	44.2%	40.2%	40.2%	39.5%	36.7%	30.2%

Table J3. Single Factor Optimization – Overall Height

Overall Height /mm	115.5	105	96.25	87.50	78.75
Shut-Off Pressure /Pa	197779	192493	188996	185927	187485
Shut-Off Head /m	9.84	9.30	8.95	8.63	8.79
Flow Rate /m^3s^{-1}	0.1095	0.0998	0.0952	0.0893	0.0847
Velocity /m s^{-1}	8.39	7.992	7.87	7.651	7.698
π_1	0.3484	0.3266	0.3177	0.3033	0.2851
Y-Axis Torque /Nm	38.94	38.09	36.18	34.54	34.49
Water Power 2	3854	3187	2948	2614	2510
Shaft Power	7111	6956	6608	6308	6298
Efficiency η	54.2%	45.8%	44.6%	41.4%	39.8%

Table J4. Single Factor Optimization – Vane Angle

Vane Angle /mm	45.00	43.00	41.00	39.00	37.00
Shut-Off Pressure /Pa	179464	181174	181535	180704	188227
Shut-Off Head /m	7.97	8.15	8.18	8.10	8.87
Flow Rate /m^3 s^{-1}	0.0793	0.0818	0.0838	0.0827	0.0841
Velocity /m s^{-1}	7.64	7.651	7.65	7.63	7.64
π_1	0.2803	0.2860	0.2924	0.2900	0.2819
Y-Axis Torque /Nm	36.29	34.54	32.11	29.59	29.76
Water Power 2	2313	2394	2454	2406	2457
Shaft Power	6628	6308	5864	5404	5435
Efficiency η	34.9%	38.0%	41.9%	44.5%	45.2%

Table J5. Results for 2^3 Experiments

Diameter /mm	178.9
Surface Area /m^2	0.0275

Case No.	A	B	C	Pressure /Pa	Shut-Off Head /m	Flow Rate /m^3	Velocity /m s^-1	π_1	Y-Axis Torque /Nm	Water Power /W	Shaft Power /W	Effici−ency η
1	–	–	–	186069	8.65	0.0840	7.78	0.2851	34.63	2545	6325	40.2%
2	–	–	+	180855	8.12	0.0877	7.906	0.3073	36.54	2741	6674	41.1%
3	–	+	–	192522	9.31	0.0791	7.753	0.2588	33.09	2377	6044	39.3%
4	–	+	+	201283	10.20	0.0838	7.829	0.2619	35.79	2568	6537	39.3%
5	+	–	–	185927	8.63	0.0826	7.651	0.2806	34.54	2418	6308	38.3%
6	+	–	+	188996	8.95	0.0952	7.87	0.3177	36.18	2948	6608	44.6%
7	+	+	–	203634	10.44	0.0853	7.601	0.2635	33.54	2464	6125	40.2%
8	+	+	+	190612	9.11	0.0804	7.865	0.2659	34.11	2487	6229	39.9%

J-2. Matlab Code to Perform ANOVA

```
pi1 = [0.2851
0.3073
0.2588
0.2619
0.2806
0.3177
0.2635
0.2659];
Eff = [40.2
41.1
39.3
39.3
38.3
44.6
40.2
39.9];
g1 = [52.4 52.4 52.4 52.4 58.22 58.22 58.22 58.22];
g2 = [126.6 126.6 139.26 139.26 126.6 126.6 139.26
139.26];
g3 = [87.5 96.25 87.5 96.25 87.5 96.25 87.5 96.25];
% g1 = [0 0 0 0 1 1 1 1];
% g2 = [0 0 1 1 0 0 1 1];
% g3 = [0 1 0 1 0 1 0 1];
P_pi1=anovan(pi1,{g1,g2,g3},'model','interaction','varn
ames',{'Cone Height','Cone Diameter','Overall
Height'}...
    ,'alpha',0.10,'sstype',2,'continuous',[1 2 3]);
P_Eff=anovan(Eff,{g1,g2,g3},'model','interaction','varn
ames',{'Cone Height','Cone Diameter','Overall
Height'}...
    ,'alpha',0.10,'sstype',3,'continuous',[1 2 3]);
```

REFERENCES

Aban, M. M., and International Rice Research Institute. (1985). Design parameters affecting the performance of the IRRI-designed axial-flow pump (IRRI research paper series, no. 112; IRRI research paper series, no. 112). Manila, Philippines: International Rice Research Institute.

Bangladesh Agricultural Development Corporation. (June 2013). *Minor Irrigation Survey Report 2012-13*. Bangladesh: Ministry of Agriculture.

Biggs, D. (2011). Small Machines in the Garden: Everyday Technology and Revolution in the Mekong Delta. *Modern Asian Studies*, 47-70.

Chinsuwan, W. (1985). *Development and Use of the Axial Flow Lowlift Pump in Thailand*. Thailand: Department of Agricultural Engineering, Khon Kaen University.

Crane Co. Engineering Division (2012). *Flow of fluids through valves, fittings, and pipe*. The Woodlands, TX: Crane.

Esch, B. P. M. Van, and Kruyt, N. P. (2001) Hydraulic Performance of a Mixed-Flow Pump: Unsteady Inviscid Computations and Loss Models. *Journal of Fluids Engineering* 123.2: 256.

Godfray, H.C.J., J.R. Beddington, I.R. Crute, L. Haddad, D. Lawrence, J.F. Muir, et al. (2010). Food security: the challenge of feeding 9 billion people. Science 327: 812-818.

Kalitzin, G., and Iaccarino, G., 2002. Turbulence Modeling in an Immersed-Boundary RANS-Method, Center for Turbulence Research Annual Research Briefs, Stanford University, California, pp. 415 - 426

Karassik, Igor J., Messina, Joseph P., and Cooper, Paul. *Pump Handbook* (4th Edition). Blacklick, OH, USA: McGraw-Hill Professional Publishing, 2007. ProQuest ebrary.

Kasantikul, B., and Laksitanonta, S. (2014). Study and Develop the Thai-Made Irrigation Pump System (Tor Payanak) in a Large Aquaculture Pond. *Journal of Agricultural Technology*, 10(5), 1115-1138.

Lam, Eric, Krupnik, Timothy J., Matin, Md. Abdul, Hossain, Md. Ayub, and Colton, Jonathan. (2015). Standard Protocol for Evaluation of Surface Water Irrigation Pumps in South Asia. *US AID, from the American People.* Cereal Systems Initiative for South Asia- Mechanization and Irrigation (CSISA-MI).

Maps of World. (February 2016). Top Ten Countries with Most Rice Producing Countries.

Minor Irrigation Survey Report 2012-13. (June 2013). Bangladesh: Ministry of Agriculture.

Molle, Francois., Shah, Tushaar., and Baker, Randy. (2003) The Groundswell of Pumps: Multilevel Impacts of a Silent Revolution. *ICID-Asia Meeting*, Taiwan.

Munson, B. R., Okiishi, T. H., and Huebsch, W. W. (2009). Chapter 8 Section 4: Dimensional Analysis of Pipe Flow. *Fundamentals of Fluid Mechanics*. Hoboken, NJ: J. Wiley & Sons.

NCEES, (2013). *FE Reference Handbook*. Retrieved from http://ncees.org/engineering/fe/

PattanaKarnkol. (n.d.). Thai Propeller Pump. Retrieved April 18, 2014, from www.thaipropellerpumpcom

Sarker, A., and Ali, M. (2010). Irrigation Management for Optimizing Rice Yield and Nitrate Leaching. *Agricultural Engineering Division* (pp. 59-68). Bangladesh: Institute of Engineers.

Schulthess, U., Krupnik, T. J., Ahmed, Z. U., and McDonald, A. J. (2015). Technology targeting for sustainable intensification of crop production in the Delta region of Bangladesh. *Int. Arch. Photogramm. Remote Sens. Spatial Inf. Sci. ISPRS - International Archives of the Photogrammetry, Remote Sensing and Spatial Information Sciences, XL-7/W3*, 1475-1481. doi:10.5194/isprsarchives-xl-7-w3-1475-2015

Schwartzberg, Joseph E. (February 2016). India. *Encyclopedia Britannica*. Retrieved from http://www.britannica.com/place/India

Soil Conservation Service. (1999). Chapter 8 Section 15: Irrigation. In *SCS National Engineering Handbook*. United States Department of Agriculture.

Stepanoff, Alexey J. (1957) *Centrifugal and axial flow pumps: theory, design, and application*. New York: Wiley. Print.

Stickney, R., and Salazar, G. (1989). Axial-Flow Propeller Pump for Small Rice Farms and Fishponds. *Waterliens*, Vol.8 No.2.

Tavakul, D. 1967. Research and Development of Irrigation Equipment (in Thai). *Technology and Agriculture*. pp 20-24.

The International Rice Research Institute. (1983). *Comparative Advantages of Axial-Flow Pumps Over Centrifugal Pumps for Low-Lift Irrigation*. Malate: IRRI.

The Engineering Tool Box, (n.d.). Minor Loss Coefficients in Pipes and Tubes Components. Retrieved from http://www.engineeringtoolbox.com/minor-loss-coefficients-pipes-d_626.html

Tilman, D., C. Balzer, J. Hill and B.L. Befort. 2011. Global food demand and the sustainable intensification of agriculture. Proceedings of the *National Academy of Sciences of the United States of America* 108: 20260-20264.

Varchola, M., and Hlbocan, P. (2012). Geometry Design of a Mixed Flow Pump Using Experimental Results of on Internal Impeller Flow. *Procedia Engineering*, 168-174.

Wilcox, David C. (2000) *Basic Fluid Mechanics*. La Cañada, CA: DCW Industries

World Bank Group. (2016). GDP per Capita (current US$). *The World Bank | Working for a World Free of Poverty*. Retrieved from http://data.worldbank.org/indicator/NY.GDP.PCAP.CD?order=wbapi_data_value_2014+wbapi_data_value+wbapi_data_value-last&sort=desc

World Bank Group. (2016). Poverty & Equity. *The World Bank | Working for a World Free of Poverty*. Retrieved from http://povertydata.worldbank.org/poverty/region/EAP

Wu, C., and Hamada, M. (2000). *Experiments: Planning, Analysis, and Parameter Design Optimization.* New York: Wiley.